COMPOSITES CONTAINING PERCOLATED NETWORKS AND/OR CORE-SHELL STRUCTURES USEFUL FOR MICROSYSTEMS APPLICATIONS

A Dissertation
Presented to
The Academic Faculty

by

Youngho Jin

In Partial Fulfillment
of the Requirements for the Degree
Doctor of Philosophy in the
School of Materials Science and Engineering

Georgia Institute of Technology
December 2016

COMPOSITES CONTAINING PERCOLATED NETWORKS AND/OR CORE-SHELL STRUCTURES USEFUL FOR MICROSYSTEMS APPLICATIONS

Approved by:

Dr. Rosario A. Gerhardt, Advisor
School of Materials Science and Engineering
Georgia Institute of Technology

Dr. Arun M. Gokhale
School of Materials Science and Engineering
Georgia Institute of Technology

Dr. Seung Soon Jang
School of Materials Science and Engineering
Georgia Institute of Technology

Dr. Mark D. Losego
School of Materials Science and Engineering
Georgia Institute of Technology

Dr. Pulugurtha Markondeya Raj
School of Electrical and Computer Engineering
Georgia Institute of Technology

Date Approved: August 19, 2016

ACKNOWLEDGEMENTS

I would like to express my deepest appreciation to everyone who has supported and helped me in one way or another during the course of my PhD study. First of all, I want to thank my advisor Prof. Gerhardt for accepting, supporting, encouraging, and guiding me in every possible way. I want to express my gratitude to my committee members Dr. Gokhale, Dr. Jang, Dr. Losego and Dr. Raj for all their knowledge, support, and advice throughout this thesis process.

I am highly indebted to the current and past group members, Timothy Pruyn, Rachel Muhlbauer, Justin Brandt, Ning Xia, Thomas Rudzik, and Morgan Watt for useful training, constructive discussions and suggestions. The Gerhardt group has always been welcoming and warm to me, and also made graduate school an enjoyable experience.

I would like to acknowledge the funding and financial support from the National Science Foundation via DMR-1207323 for this project over the years. The training of Todd Walters with SEMs, EDS and TEM, the assistance of David Tavakoli with XRD and the help of Dr. Amanda Gable with academic writing is greatly appreciated.

Finally, I want to thank my families for their endless encouragement throughout my study. My wife Soyoung Kim has helped me all along, and I feel really fortunate to have her by my side. I am also endlessly thankful to my parents, Munsop Jin and Yeonhee Lee and my children Seona and Seonwoo Jin, who have always been so supportive and encouraging throughout my education. None of this would be possible without their love.

TABLE OF CONTENTS

Page

ACKNOWLEDGEMENTS iii

LIST OF TABLES ix

LIST OF FIGURES x

LIST OF SYMBOLS xvii

LIST OF ABBREVIATIONS xviii

SUMMARY xx

CHAPTER

1 INTRODUCTION 1

1.1 Effects of Precursor Materials and Processing Conditions in Conductive PMCs 2

1.2 Effects of Nanofiller Types, Size, Morphology and Distribution in Dielectric PMCs 3

1.3 Finite Element Simulation of Electrical Responses in Different Types of PMCs 4

1.4 Overview and Organization of the Thesis 5

2 LITERATURE SURVEY 6

2.1 Conductive Nanocomposites with Self-Assembled Nanoparticles 6

2.1.1 Fundamental Aspects of Conductive PMCs 6

2.1.1.1 Percolation Behavior in Composites 6

2.1.1.2 Effects of Microstructure on Electrical Properties 8

2.1.2 Processing and Properties of Conductive PMCs 9

2.1.2.1 Effects of Processing Methods 9

2.1.2.2 Effects of Processing Temperature and Pressure 11

2.1.3 Effects of Host and Filler Materials on Electrical Properties 13

2.1.4 Applications of Conductive PMCs 17

2.2.6 Background on Materials to be Made Into Conductive Composites in this Dissertation 18

2.1.5.1 Antimony Tin Oxide (ATO) 18

2.1.5.2 Polymethylmethacrylate (PMMA) 19

2.2 Dielectric Nanocomposites with Uniformly Distributed Nanoparticles 21

2.2.1 Fundamental Aspects of High-*k* PMCs 21

2.2.1.1 Polarization and Relaxation Behavior in High-*k* PMCs 21

2.2.1.2 Capacitance and Electric Energy Storage in High-*k* PMCs 25

2.2.1.3 Breakdown Strength in High-*k* PMCs 26

2.2.2 Theoretical Models for Dielectric Properties 27

2.2.3 Effects of Microstructure and Interfaces on Dielectric Properties 29

2.2.4 Effects of Filler Materials on Dielectric Properties 34

2.2.4.1 Effects of High-*k* Ceramic Fillers Composition 34

2.2.4.2 Effects of the Size and Shape of Fillers 35

2.2.4.3 Effects of Organic / Inorganic Conductive Fillers 37

2.2.5 Applications of High-*k* PMCs 38

2.2.6 Background on Materials to be Made Into Dielectric Composites in this Dissertation 39

2.2.6.1 Barium Titanate (BT) 39

2.2.6.2 Poly(vinylidene fluoride) (PVDF) 40

2.3 Simulation and Characterization Tools 41

2.3.1 COMSOL Multiphysics® 41

2.3.2 Impedance Spectroscopy 43

3 CONDUCTIVE NANOCOMPOSITES WITH SELF-ASSEMBLED NANOPARTICLES 47

3.1 Experimental Procedure 47

3.1.1 Filler and Matrix Components used 47

3.1.2 Composite Fabrication Procedure 48

3.1.3 Microscopy and UV-Vis Spectroscopy 49

3.1.3.1 Microscopy 49

3.1.3.2 In-situ Electrical Measurements 50

3.1.3.3 AC Electrical Measurements 51

3.2 Results and Discussion 52

3.2.1 Properties of the Precursor Materials 52

3.2.1.1 Thermal Analysis and Electrical Conductivity of Matrix Polymer (PMMA) 52

3.2.1.2 Electrical Conductivity of Antimony Tin Oxide 53

3.2.2 Characterization and Analysis of Results 55

3.2.2.1 Electrical Conductivity Percolation Curves of Conductive Nanocomposites with Monosize and Polydisperse PMMA 55

3.2.2.2 Correlation between Microstructure and Electrical Properties 60

3.2.2.3 Effects of Processing Parameters on the Electrical Conductivity of Phase Segregated Nanocomposites 62

3.2.2.4 Electromagnetic Interference Shielding Effectiveness of Phase Segregated Nanocomposites 75

3.2.3 Finite Element Modeling of Percolation Behavior of Conductive PMCs 78

3.2.3.1 Modeling Overview 78

3.2.3.2 2D Impedance Simulation of PMMA/ATO Nanocomposites 79

3.2.3.3 3D Impedance Simulation of PMMA/ATO Nanocomposites 85

3.2.4 Conclusions 89

4 DIELECTRIC NANOCOMPOSITES WITH UNIFORMLY DISTRIBUTED NANOPARTICLES 91

4.1 Experimental Procedure 91

4.1.1 Filler and Matrix Components used 91

4.1.2 Composite Fabrication Procedure 93

4.1.3 Microstructural, Thermal, and Electrical Characterization 94

4.1.3.1 Microscopy 94

4.1.3.2 Fourier Transform Infrared Spectroscopy 94

4.1.3.3 X-ray Diffraction and Thermal Analysis 95

4.1.3.4 AC Dielectric Measurements 95

4.1.3.5 High Voltage DC Breakdown Tests 96

4.2 Results and Discussion 97

4.2.1 Component Synthesis and Properties 97

4.2.1.1 Hydrothermal Synthesis of Barium Titanate Nanocrystals with different sizes 97

4.2.1.2 Surface Functionalization of Barium Titanate Nanocrystals 100

4.2.1.3 Phase and Crystallinity of Matrix Polymer (PVDF) 101

4.2.2 Characterization and Analysis of Results 108

4.2.2.1 Effects of Uniformly Distributed High-*k* Fillers 108

4.2.2.2 Effects of Conductive Fillers in Conjunction with High-*k* Fillers 112

4.2.2.3 Effects of Particle Size of High-*k* Fillers 120

4.2.2.4 Breakdown Strength and Energy Density of the Dielectric PMC 124

4.2.2.5 Equivalent Circuit Fitting for Dielectric Responses of the Dielectric PMCs 127

4.2.3 Finite Element Modeling of Dielectric Behavior of the Dielectric PMCs 133

4.2.3.1 Modeling Overview 133

4.2.3.2 Dielectric Responses from Interactions of Fillers 134

4.2.3.3 Dielectric Responses as a Function of Concentration of Fillers 136

4.3 Conclusion 139

5 CONCLUSIONS AND SUGGESTED FUTURE WORK 140

5.1 Conclusions 140

5.2 Suggested Future Work 142

APPENDIX A: HYDROTHERMAL SYNTHESIS OF BT NANOCRYSTALS 144

REFERENCES 149

LIST OF TABLES

Page

Table 4.1: Dielectric properties of reported polymer matrix composites 126

Table 4.2: Simulated values of the equivalent circuit elements. (obtained from the average) 128

Table 4.3: Comparison of real permittivity at 1kHz between finite element analysis and experiments 136

LIST OF FIGURES

Page

Figure 2.1: (a) Schematic of segregated conductive network, (b) random distribution conductive network and (c) Log DC resistivity vs. volume fraction of carbon black (CB)-PMMA composites with segregated network and random network. Modified from reference.[4, 19] 8

Figure 2.2: Schematics and followed by microstructural images for fabricating conductive nanocomposites with phase segregated microstructure: (a-b) mechanical blending,[30] (c-d) latex technology,[24] (e-f) melt blending[21] and (g-h) miscible solvent mixing and precipitation.[29] Schematics in (a, c, and e) were modified from reference.[4] 11

Figure 2.3: Effects of compression molding pressure on the DC conductivity of PMMA/ITO composites as a function of ITO concentration.[10] 13

Figure 2.4: Effects of matrix microsphere size on the electrical conductivity of polystyrene-carbon black composites as a function of carbon black. Modified from reference.[34] 14

Figure 2.5: Effects of matrix polymer on the formation of segregated network and following electrical conductivity of composites. (a) Electrical conductivity of soft latex (red triangles) and hard latex (blue squares) as a function of CNT concentration, (b-c) SEM images of the hard latex composites and (d-e) atomic force microscopy (AFM) topography of the soft latex composites.[4, 24] 15

Figure 2.6: Effects of the particle size ratio between the matrix and the filler on the percolation threshold (f_c).[9] A cartoon inset shows the difference in particle size of the matrix and the filler.[35] 16

Figure 2.7: Effects of filler geometry on the dimensionality of the segregated conductive networks: SEM images of fractured cross-sections of (a) CNT-HDPE and (b) GNS-HDPE composites and (c) the following electrical conductivity of the composites as a function of filler concentration (black diamonds show CNT and red stars show GNS.[36] 17

Figure 2.8: Classification of conductive polymer composites according to their electrical resistivity and application ranges.[4] 18

Figure 2.9: A unit cell of rutile SnO_2 showing the location of interstitial antimony.[45, 46] 19

Figure 2.10: Molecular structure of PMMA 20

Figure 2.11: Temperature dependence of viscosity(η) below and near glass transition temperature for some common polymers.[49] 21

Figure 2.12: A dielectric medium showing a random orientation when no electric field is applied (left) and a polarized orientation of charged particles when an electric field is applied. 22

Figure 2.13: A dielectric permittivity spectrum over a wide range of frequencies. The real and imaginary parts of permittivity are shown, and various mechanisms are depicted: ionic and dipolar relaxation, and atomic and electronic resonances at higher energies in terms of the real and imaginary parts of the permittivity. (copyright Prof. Kenneth A. Mauritz, Univ. Southern Mississippi) 24

Figure 2.14: Effects of microstructure and interfaces of the matrix and the filler on the dielectric properties of composites: (a) core-shell structure with spherical filler,[69] (b) randomly distributed high aspect ratio filler,[72] (c) highly aligned conductive nanotubes,[74] and (d) layered structure with conductive interlayer.[73] Schematics in (a-b) were drawn by the author of this dissertation. 31

Figure 2.15: General methods associated with design and construction of core–shell nanoparticles for high-*k* polymer nanocomposites.[52] 33

Figure 2.16: General schematics of the IBLC theory associated with CCTO's giant dielectric constant.[12, 90] 35

Figure 2.17: Effects of filler particle size in some PVDF/BT composite: (a) 60 vol % BT in PVDF[95] and (b) 50% BT in PVDF.[96] 36

Figure 2.18: Dielectric properties of nanocomposites in terms of filler morphology and concentration.[99] 37

Figure 2.19: The structure of (left) cubic and (right) tetragonal $BaTiO_3$. The red spheres represent oxygen centers, blue Ti^{4+} cations, and green Ba^{2+}, respectively. The off-center position of Ti^{4+} ions are shown in tetragonal structure. (copyright Army High Performance Computing Research Center (AHPCRC), Stanford University) 40

Figure 2.20: Structures of (a) non-ferroelectric α phase and (b) ferroelectric β phase PVDF.[120] 41

Figure 2.21: (a) Complex impedance plot for a resistor (1000 Ω) and a capacitor (1 nF) in parallel. (b) Complex impedance plot for a resistor (1000 Ω) and an inductor (1 μH) in parallel. (c) Complex impedance plot for a resistor (1000 Ω) and a capacitor (1 nF) in series.(d) Complex impedance plot for a resistor (1000 Ω) and an inductor (1 μH) in series. (e) Phase angle Bode plot of the circuit impedance from (a-d). (f) Impedance magnitude plot of the circuits from (a-d).[35, 127] 45

Figure 3.1: Optical images of (a) monosize PMMA, (b) polydisperse PMMA and (c) TEM image of ATO nanoparticles.[6] 48

Figure 3.2: Schematic of the in-situ measurements configuration. 51

Figure 3.3: Differential scanning calorimetry (DSC) scan of PMMA particles. 52

Figure 3.4: Impedance complex plot of compression molded PMMA pellet (diameter: 31.7 mm and thickness: 2 mm). 53

Figure 3.5: (a) Impedance magnitude and (b) impedance phase angle of compressed ATO powder at pressures from 56.6 to 226.6 MPa (Solid lines are fit data; diameter and thickness of pellet at 226.6 MPa are 10 mm and 1.3 mm respectively). 54

Figure 3.6: (a) Complex impedance plots for several PMMA/ATO composites. (b) Complex impedance plot for the 0.09 vol % PMMA/ATO composite, fitted using a parallel R-CPE model (shown by the solid line). 56

Figure 3.7: DC conductivity of PMMA/ATO nanocomposites as a function of ATO content (molded at 170 ℃, 50.6 MPa for 15 min).[6] 57

Figure 3.8: AC conductivity of PMMA/ATO nanocomposites for different ATO contents (molded at 170 ℃, 50.6 MPa for 15 min) using (a) monosize PMMA and (b) polydisperse PMMA.[6] 59

Figure 3.9: SEM images of polished surfaces of PMMA/ATO nanocomposites containing 0.09 and 1.06 vol % ATO for the polydisperse PMMA (shown in panels a and c) and the monosize PMMA (shown in panels b and d), respectively.[6] 61

Figure 3.10: (a) SEM image of nanocomposite (1.06 vol %). (b) EDS spectra at different locations: ① edge ② center.[6] 62

Figure 3.11: AC conductivity as a function of frequency for PMMA/ATO composites containing different (a) ATO contents as well as molding pressures and (b) molding temperatures for 2 mm pellets. 64

Figure 3.12: DC conductivity of PMMA/1.06 vol % ATO nanocomposite as a function of (a) molding pressure and (b) molding temperature as well as sample thickness. 67

Figure 3.13: In-situ DC resistance during (a) heating with continuous pressure and (b) compression molding of composites. 70

Figure 3.14: Fractured cross sections for PMMA-ATO nanocomposites (thickness: 0.6 mm) containing 1.06 vol % ATO molded at 50.68 MPa and (a) 150 ℃ (b) 190 ℃ (taken perpendicular to the pressing direction). 71

Figure 3.15: (a) Schematics of the microstructure with respect to increasing molding pressure (images modified from reference [18]), (b-e) SEM images on the polished top surfaces and cross sections of PMMA/1.06 vol % ATO nanocomposites (thickness: 0.6 mm) molded at 190 ℃ with 12.67 MPa and 50.68 MPa. 72

Figure 3.16: DC conductivity of 2 mm thick PMMA/ATO composites as a function of ATO content for samples made at 170 ℃ and different molding pressures. 74

Figure 3.17: Optical transmittance spectra of PMMA/ATO composites made at 170 ℃ and 12.67 MPa (thickness: 0.2 mm) between 390-700 nm (visible light region) as a function of ATO content. 75

Figure 3.18: Electromagnetic interference shielding effectiveness (EMI SE) of PMMA/ATO composites (compression molded at 170 ℃ and 50.68 MPa with thickness of 2 mm). Note that EMI SE data are taken from S_{12} values because S_{11} values are negligible. 77

Figure 3.19: Schematic of 1D percolation in 2D lattice (a) 2D simplified geometry (b) filler distribution (partially connected and disconnected) and corresponding calculated electrical potentials.[6] 79

Figure 3.20: Predicted DC conductivity as filler packing density “1.0” illustrates perfect solid filler chains and “0.65” illustrates minimum density to maintain percolated state. Modified from reference.[6] 81

Figure 3.21: FEA simulated AC conductivity of PMMA/ATO nanocomposites using different 1D chain lengths and packing densities in 2D lattice. Modified from reference.[6] 82

Figure 3.22: Area fraction of the fillers to completely cover the edges of the matrix polygons as a function of matrix and filler size derived from FEA simulations of 2D idealized segregated network microstructures.[6] 84

Figure 3.23: (a) FEA configuration and (b) simulated current density map of PMMA/ATO nanocomposites for different percolation paths (thickness of edges: 100 nm). 86

Figure 3.24: FEA simulated impedance of PMMA/ATO nanocomposites using different 1D chain paths and packing density. 100 % connected represents the maximum possible conductivity for the monosize PMMA/ATO composites. 86

Figure 3.25: Examples of FEA study on PMCs with different fillers. (a) PMMA/CB composites and (b) PMMA/ITO composites 88

Figure 4.1: TEM images of commercial (a) BT nanoparticles (b) MWCNT. 92

Figure 4.2: Schematics of steps for making BT/MWCNT/PVDF hybrid nanocomposites using a simple phase separation method. Optical images in the bottom right show appearance of composites containing 37.1 vol % BT with 0 vol % MWCNT (left), and 3 vol % MWCNT (right). 94

Figure 4.3: XRD patterns of synthesized BT nanoparticles. 97

Figure 4.4: TEM images of hydrothermally synthesized BT in DI water at 180 ℃ for (a) 3 h, (b) 6 h, (c) 12 h and (d) 24 h. 98

Figure 4.5: Particle size of synthesized BT as a function of reaction time at 180 ℃ in DI water (blue circle) and in 30% ammonia solution (red star) 99

Figure 4.6: Thermogravimetric analysis of BT before and after surface modification with MPS. 100

Figure 4.7: FTIR spectra of BT nanoparticles before and after surface modification with MPS. 101

Figure 4.8: (a) FTIR and (b) DSC results for pure PVDF; hot pressed from powder (dash) and hot pressed after coagulation (solid). 103

Figure 4.9: (a) XRD patterns for pure PVDF film; hot pressed after coagulation (solid) and hot pressed from powder (dash), (b) XRD patterns for pure PVDF (bottom), nanocomposites containing 22.8 vol % BT (middle) and 37.1 vol % BT (up). 104

Figure 4.10: 4.10. FTIR spectra of heat treated and untreated (a) PVDF and (b) PVDF-HFP films.[83] 106

Figure 4.11: DSC results of heat treated and untreated (a) PVDF and (b) PVDF-HFP films.[83] 107

Figure 4.12: SEM images of nanocomposites (a) filler dispersion by surfactant and (b) filler dispersion by surface modification. Inset in (b) shows flexibility of the composite even in a thick (500 μm) sample.[11] 109

Figure 4.13: (a) Real permittivity and (b) dielectric loss for composites containing different amounts of BT.[11] 111

Figure 4.14: SEM images of BT/MWCNT/PVDF hybrid nanocomposites containing 37.1 vol % BT and 3 vol % MWCNT (a) top surface of the nanocomposite (b-d) fractured cross sections of the nanocomposites with different magnifications.[83] 112

Figure 4.15: (a) Real permittivity and (b) dielectric loss of nanocomposites containing 22.8 vol % BT and MWCNT varying contents of 0 to 5 vol %.[83] 114

Figure 4.16: (a) Real permittivity and (b) dielectric loss of nanocomposites containing 3 vol % MWCNT and 22.8, 37.1 and 47.0 vol % BT.[83] 115

Figure 4.17: AC conductivity of nanocomposites containing 22.8 vol % BT and 0 to 5 vol % MWCNT as well as samples containing 37.1 vol % BT and 0 to 4 vol % MWCNT.[83] 117

Figure 4.18: Steady state dielectric properties of nanocomposites at 1 kHz (a) real permittivity and (b) dielectric loss.[83] 119

Figure 4.19: (a) Real permittivity and (b) dielectric loss of nanocomposites containing 37.1 vol % BT synthesized with different sizes (78 nm BT was commercially obtained). 121

Figure 4.20: Steady state dielectric properties of nanocomposites at 100-1MHz as a function of particle size (a) real permittivity (b) dielectric loss. 123

Figure 4.21: (a) Breakdown strength of heat treated (grey) and untreated (white) pure PVDF, PVDF-HFP and nanocomposites containing 37.1 vol % BT and 1 to 3 vol % MWCNT. (b) Calculated energy density.[83] 125

Figure 4.22: Equivalent circuit fitting of a composite containing 37.1 vol % BT and 3 vol % MWCNT (a) impedance complex plot, (b) permittivity complex plot, (c) real permittivity and (d) dielectric loss. 131

Figure 4.23: Additional equivalent circuit fitted curves for the same composite containing 37.1 vol % BT and 3 vol % MWCNT displayed in Fig. 4.22 (a) real impedance, (b) imaginary impedance (c) real admittance, (d) imaginary admittance, (e) real electric modulus and (f) imaginary electric modulus plots.[83] 132

Figure 4.24: Schematic of the configuration for dielectric simulation of a composite containing 47.9 vol % BT.[83] 133

Figure 4.25: (a) Simulation of the effects of inter-particle distance in electric displacement field in between BT NPs (60, 40, 20, and 10 nm from the left) and (b) schematic of interaction zone with respect to inter-particle distance (image modified from reference.[12]) 134

Figure 4.26: Cross-sectional electric displacements field maps of composites containing 22.8 vol % BT and 0 to 3 vol % MWCNT. 135

Figure 4.27: FEA modeling geometry for different BT concentrations with minimum inter-particle distance of 10 nm; (a) 10 vol % BT, (b) 20 vol % BT, (c) 30 vol % BT, and (d) 40 vol % BT.[83] 138

Figure 4.28: Experimental and FEA simulated real permittivity of composites as a function of BT content and calculated values by some numerical models.[83] 138

Figure A.1: TEM images of hydrothermally synthesized BT crystals with different shapes: (a) star (80 ℃ / 0.2 M $Ba(OH)_2 \cdot 8H_2O$), (b) sword (120 ℃ / 0.1 M $Ba(OH)_2 \cdot 8H_2O$), (c) cube (140 ℃ / 0.2 M $Ba(OH)_2 \cdot 8H_2O$), (d) Nanowire (210 ℃ / 0.1 M $Ba(OH)_2 \cdot 8H_2O$). 146

Figure A.2: Influence of the hydrothermal reaction conditions on the shapes of the synthesized BT crystals. 147

LIST OF SYMBOLS

ρ_c/f_c	Percolation threshold
T_g	Glass transition temperature
T_m	Melting temperature
η	Viscosity
ε_0	Permittivity of free space
σ	Electrical conductivity
ε_r	Relative permittivity
ε'	Real permittivity
ε''	Imaginary permittivity
Tan δ	Loss tangent
C	Capacitance
V_{bd}	Breakdown voltage
E_{bd}	Breakdown strength
$\breve{W}$	Volumetric energy density
Z'	Real impedance
Z"	Imaginary impedance
Y'	Real admittance
Y"	Imaginary admittance
M'	Real electric modulus
M"	Imaginary electric modulus

LIST OF ABBREVIATIONS

PMMA	Poly(methyl methacrylate)
ATO	Antimony tin oxide
PMC	Polymer matrix composite
high-*k*	High permittivity
PVDF	poly(vinylidene fluoride)
$BaTiO_3$/BT	Barium titanate
$Ba_{0.2}Sr_{0.8}TiO_2$/BST	Barium strontium titanate
$CaCu_3Ti_4O_{12}$/CCTO	Calcium copper titanate
CB	Carbon Black
ABS	Acrylonitrile-butadiene-styrene
CNT	Carbon nanotube
GNS	Graphene nano sheet
HDPE	High density polyethylene
MWCNT	Multiwall carbon nanotube
SEM	Scanning electron microscopy
EMI	Electromagnetic interference
TCO	Transparent conducting oxide
ITO	Indium tin oxide
VTF	Vogel-Tammann-Fulcher equation
Tan δ	Loss tangent
ATRP	Atom transfer radical polymerization
RAFT	Reversible addition-fragmentation chain transfer

CP	Colossal permittivity
IBLC	Internal barrier layer capacitance
BOPP	Biaxially oriented polypropylene
PZT	Lead zirconate titanate
PMN	Lead manganese niobate
KNO	Potassium niobate
FEA	Finite element analysis
TEM	Transmission electron microscopy
DSC	Differential scanning calorimetry
CPE	Constant phase element
EDS	Energy dispersive spectroscopy
P(VDF-HFP)	Poly(vinylidene fluoride)-hexafluoropropylene
DMF	Dimethylformamide
FTIR	Fourier transform infrared spectroscopy
XRD	X-ray diffractometer
TGA	Thermogravimetric analyzer

SUMMARY

Polymer matrix composites (PMCs) can have percolated networks of fillers or uniform core-shell structures depending on the fabrication process used. PMCs with percolated networks of electrically conductive fillers can be useful for various applications, including anti-static materials, electromagnetic interference (EMI) shielding, electronic-nose devices, sensors and conductors, while PMCs with uniform core-shell structures of dielectric and/or conductive fillers can be useful for applications such as embedded capacitors, gate dielectrics, energy storage devices and electromechanical transducers. In this research, experimental and computational investigations have been conducted on both types of polymer matrix composite systems.

First, electrical percolation in phase segregated polymer matrix conductive composites consisting of poly(methyl methacrylate) (PMMA) microspheres and antimony tin oxide (ATO) nanoparticles was investigated. The nanocomposites were fabricated by mechanical blending combined with compression molding. As a result of this process, the matrix PMMA was transformed into space filling polyhedra and the ATO nanoparticles were primarily distributed at the interfaces between matrix-rich regions, forming a 3D interconnected network. Percolation was achieved at a very low ATO content (0.18 vol %) when using monosize spheres. The effects of the average size and size distribution of the matrix polymer microspheres were investigated and the correlation between processing, electrical conductivity and microstructure was investigated using impedance spectroscopy and SEM. A parametric finite element approach was chosen for simulating this unique microstructure-driven percolation behavior. Good agreement was obtained between the experimental and the simulation results. The simulation model developed is applicable to many different kinds of phase

segregated insulator-conductor composite systems to predict the electrical percolation behavior.

Second, an investigation was conducted on polymer matrix dielectric composites with uniform core-shell microstructure containing poly(vinylidene fluoride) (PVDF), barium titanate ($BaTiO_3$) and/or multiwall carbon nanotubes (MWCNT). Composites with high dielectric permittivity and low dielectric loss were obtained by a simple phase separation method combined with compression molding to evenly distribute the nanofillers in the polymer matrix at all length-scales. The effects of nanofiller type, size and distribution in the dielectric PMCs were investigated as a way to improve the dielectric properties.

Impedance spectroscopy was used to examine the dielectric properties of PMCs and to reveal interesting dependences on the size and shape of the nanofillers used. The maximum relative real permittivity achieved was above 70 with very low loss (<0.045 at 1kHz). For quantitative analysis of the dielectric polarization mechanism in the dielectric PMCs, an equivalent circuit model consisting of a modified Debye circuit and a parallel RC circuit in series was introduced to describe the dielectric responses of the multi-phase nanocomposites. The finite element approach was also used to simulate the dielectric properties of PMCs with one or more types of uniformly distributed fillers. It was found that the interfaces between the matrix and the filler play a significant role in improving the dielectric properties. The geometry-based 3D finite element simulation model can be applicable to different composite systems with fillers of different shapes and properties.

CHAPTER 1

INTRODUCTION

A composite material is a multi-phase system that consists of a matrix material and a filler material that have different properties and can be made into different forms through a variety of compounding methods. The benefit of composites is that they not only maintain the main characteristics of the original components, but may also show new characteristics which are not possessed by any of the original components.[1] Generally the matrix material in composites is a continuous phase, which may include metals, ceramics and polymers, and the filler material is the dispersed phase. Fillers often include fibrous materials such as glass fiber and organic fiber, micro- and nano-particles or other 1D/2D materials such as nanotubes and nanosheets.

Polymer matrix composites (PMCs) use polymers as the matrix. PMCs, which contain single or multiple fillers, are an important class of materials that are useful for various applications. The properties of PMCs are highly dependent on the type of polymer matrix and filler material used as well as the processing conditions used to make them. The advantages of PMCs typically include good mechanical properties, a wide range of electrical properties, and ease of production in terms of cost and processing.[2] From the service performance standpoint, there are two main types of PMCs: (1) structural composites, (2) functional composites.[1] For structural composites, their mechanical properties are the most important, while for functional composites, it is their optical, electrical, magnetic and thermal properties that matters.

As functional composites, PMCs with high electrical conductivity or high dielectric permittivity have attracted academic and industrial attention. Interestingly, the microstructures of the PMCs, which may vary depending on the fabrication conditions used, can play a significant role in obtaining a wide range of electrical properties ranging

from an electrically conducting composite to a high dielectric constant insulating composite. PMCs may be rendered electrically conducting if the microstructure permits percolation of the conductive filler through the matrix.[3] PMCs may also have high dielectric constant if the microstructure contains uniform distribution of high-*k* and/or conductive fillers without forming percolation networks.

Despite the recent success in these PMCs, there are still challenges remaining.[4, 5] In conductive PMCs, the effects of precursor materials and processing conditions on the formation of percolated networks and resultant electrical properties have not been fully investigated. In dielectric PMCs, ideal methods to achieve a uniform distribution of nanofillers are needed, and the interfaces between the matrix and the filler should be improved for better dielectric properties. In this thesis, conductive PMCs with phase-segregated percolation networks and dielectric PMCs with randomly distributed nano-fillers are investigated as separated chapters. These composites are characterized with different kinds of tools and techniques as well as simulation with respect to the following topics: (1) effects of precursor materials and processing conditions in conductive PMCs, (2) effects of nanofiller type, size, morphology and distribution in dielectric PMCs, (3) finite element simulation of electrical responses in different types of PMCs.

1.1 Effects of Precursor Materials and Processing Conditions in Conductive PMCs

Among many conventional fabrication methods, mechanical blending followed by hot pressing has been reported to have the lowest percolation threshold at which transition from a capacitor to a resistor occurs due to the phase segregated microstructure.[4, 6] Many factors can contribute to the formation of the phase segregated microstructure. First, the intrinsic characteristics of conductive fillers can be one of the most decisive factors. Not only does the intrinsic electrical conductivity of the filler control the electrical conductivity of the composites, but the particle size of the conductive filler can also affect the microstructure and the percolation threshold.[6-9]

Second, the polymer matrix itself can also be one of the most important factors in forming the phase-segregated microstructure. The average size and the size distribution of the matrix polymer microspheres can play a critical role in determining the percolation threshold and the microstructure of composites.[6] Third, the electrical properties and the percolation threshold can also be affected by the processing parameters, such as mixing methods, processing pressure and temperature. Although, the effects of the processing pressure on the electrical properties of conductive PMCs have been previously reported,[10] further in-depth studies are necessary to find the optimum processing parameters.

In this thesis, the effects of the average size and size distribution of the matrix polymer are described in mechanically blended phase segregated composites. The effects of processing parameters on the electrical conductivity of conductive PMCs and the correlation between microstructure, properties and processing will also be investigated and analyzed.

1.2 Effects of Nanofiller Type, Size, Morphology and Distribution in Dielectric PMCs

Polymer matrix composites (PMCs) for dielectric applications exhibit polarization and conduction phenomena under an applied electric field through charge migration. Contrasting with conductive PMCs, the charge in dielectric composites is confined in the local space, which results in induced dipole moments. Various types of fillers have been investigated for the past decade including both conducting and dielectric fillers. The uniform distribution of the filler and preventing percolation of conducting fillers are of prime concerns, and methods ideal for achieving a random distribution of the fillers are needed.

A new solution based direct blending and miscible immiscible coagulation method followed by hot pressing[11] is described in this thesis. Different types of fillers, such as conductive carbon nanotubes and ferroelectric BT nanoparticles are investigated.

The polymer matrix is modified by either single or hybrid fillers to improve the dielectric properties. Different types of fillers are subject to hybridization and/or surface modification prior to incorporation into the matrix.

The effects of the filler size on the dielectric polarization of the dielectric PMCs are also analyzed in this thesis. Dielectric properties, such as dielectric permittivity, dielectric loss and breakdown strength are closely linked with dielectric polarization and relaxation. The dielectric properties of PMCs are often considered as a consequence of interfacial polarization.[5, 12] Therefore the dielectric permittivity can be improved by using materials with larger interfacial area. At the same time, the dielectric loss and the breakdown strength can be improved by improving the interfacial interactions between the matrix polymer and the filler. Ferroelectric fillers with different sizes are synthesized and their effects on the dielectric properties of the dielectric PMCs are evaluated and presented.

1.3 Finite Element Simulation of Electrical Responses in Different Types of PMCs

The finite element approach was selected for simulating the impedance responses of insulator-conductor nanocomposites, which have phase segregated microstructures. 2D and 3D models are presented to predict the percolation behavior of the conductive PMCs. In this thesis, COMSOL finite element models are introduced to predict the properties of different kinds of nanocomposite systems with the phase segregated structure. The effects of the filler interconnectivity, filler packing states and the matrix and the filler conductivities are visualized in the resultant electric potential and current density maps. Dielectric PMCs with evenly distributed fillers are also studied using finite element simulation. Dielectric polarization and relaxation mechanisms in the dielectric composites with respect to the filler distribution and morphology are predicted with the aid of the finite element simulation and the equivalent circuit fitting.

1.4 Overview and Organization of the Thesis

In chapter 2 the most relevant literature pertaining to these topics is summarized to provide the background needed for the two composite types studied. Some basic background on the COMSOL Multiphysics® simulation use and impedance spectroscopy analysis are also presented.

Chapter 3 details experimental methods, including the preparation of the precursor materials, characterization techniques, the fabrication of the polymer matrix composites with phase segregated conductive networks. The factors that affect the electrical percolation behavior are investigated, including the characteristics and sizes of the matrix and the fillers and the processing parameters, such as compression molding temperature and pressure. The finite element simulation is also discussed to help improve the predictability of the electrical properties of conductive PMCs.

Chapter 4 introduces experimental details, including the preparation of the precursor materials, the characterization techniques used, as well as the fabrication techniques of the polymer matrix dielectric composites with effectively distributed fillers. Core-shell nano-particles were successfully distributed in the matrix by a simple phase separation technique, resulting in improved dielectric properties of the composites. The dielectric polarization mechanisms and the quantitative analysis of charge accumulation and charge transport effects in the polymer matrix composites with hybrid fillers are investigated. The real geometry-based finite element analysis completed will provide further understanding and improved predictability of the dielectric properties in the dielectric PMCs.

Chapter 5 concludes the dissertation and suggests possible future works that can be conducted to further develop this research.

CHAPTER 2

LITERATURE SURVEY

This chapter summarizes the current state of polymer matrix composites. The first section reviews polymer matrix conductive composites. Fundamental aspects of the conductive polymer matrix composites (PMCs) were discussed. The particular focus is on fabrication methods and materials serving as matrix polymers and conductive fillers to achieve a low electrical percolation threshold (ρ_c) for improved electrical conductivity. The second section reviews polymer matrix dielectric composites. Fundamental aspects of the dielectric polymer matrix composites (PMCs) were introduced. The particular focus is on how to fabricate a dielectric PMC with high real permittivity and low loss. Various recent investigations on the effects of processing conditions and matrix and filler materials on dielectric properties of PMCs are also discussed.

2.1 Conductive Nanocomposites with Self-Assembled Nanoparticles

2.1.1 Fundamental Aspects of Conductive PMCs

2.1.1.1 Percolation Behavior in Composites

Percolation in general is the movement of a material or signal throughout a system. Percolation phenomena are important in many systems, such as amorphous and porous materials, structured galaxies, epidemic spreading and fire spreading in a forest.[13, 14] For a composite material, percolation means the formation of interconnected networks in the composites when the filler forms some sort of contact with one another.[15] The interconnected networks result in a change of properties in the composite as the properties of the filler are imparted to it.[14] For example, the addition of an electrically conducting filler to a composite that has an electrically insulating material as the matrix

will eventually result in percolation. This will result in a rapid increase in the electrical conductivity of the composite.[3]

Most of the matrix polymer materials are electrically insulating, thus the electrical properties of polymer matrix composites are dependent on the percolation networks formed by incorporating conductive fillers.[3] The critical amount of the conductive filler, over which the composite material exhibits a transition from an insulator to a conductor is called the percolation threshold (ρ_c). The electrical conductivity of the polymer matrix percolated composites dramatically increases by several orders of magnitude when the first continuous conducting channel is connected. As the content of the conductive filler increases further, additional conductive pathways can be formed, resulting in a more gradual increase in the electrical conductivity of the composite until saturation is reached. One of the most common equations to describe electrical percolation in composite materials is shown in equation (2.1)

$$\sigma = \sigma_0(\rho - \rho_c)^t \tag{2.1}$$

where σ is the electrical conductivity of the composite, σ_0 is the proportionality constant related to the intrinsic conductivity of the filler, ρ is the probability of a site being filled, ρ_c is the percolation threshold, and t is an exponent that is related to the dimensionality of the conductive networks in the composite. It is approximately 1.6~2 in a three dimensional, and 1~1.3 in a two dimensional system.[13, 16, 17] This model is valid near the percolation threshold, but it has several limitations at the higher concentrations above the percolation threshold (ρ_c). However, equation 2.1 can still show that the concentration of the conductive filler and the percolation threshold are critical in determining the composite properties.[18]

2.1.1.2 Effects of Microstructure on Electrical Properties

Figure 2.1 shows different types of conductive networks in polymer matrix composites (PMCs) and their resulting DC resistivity. When the segregated conductive network is connected, the transition from an insulator to a conductor occurs at much lower filler concentration compared to the randomly distributed conductive network.[19] In other words, the percolation threshold can be lowered by using a phase segregated microstructure. Forming a segregated conductive network is the most promising strategy to lower ρ_c.[19, 20] The conductive fillers are primarily located at the interfaces between the matrix rich-regions instead of randomly distributed in the matrix polymer as shown in Fig. 2.1.

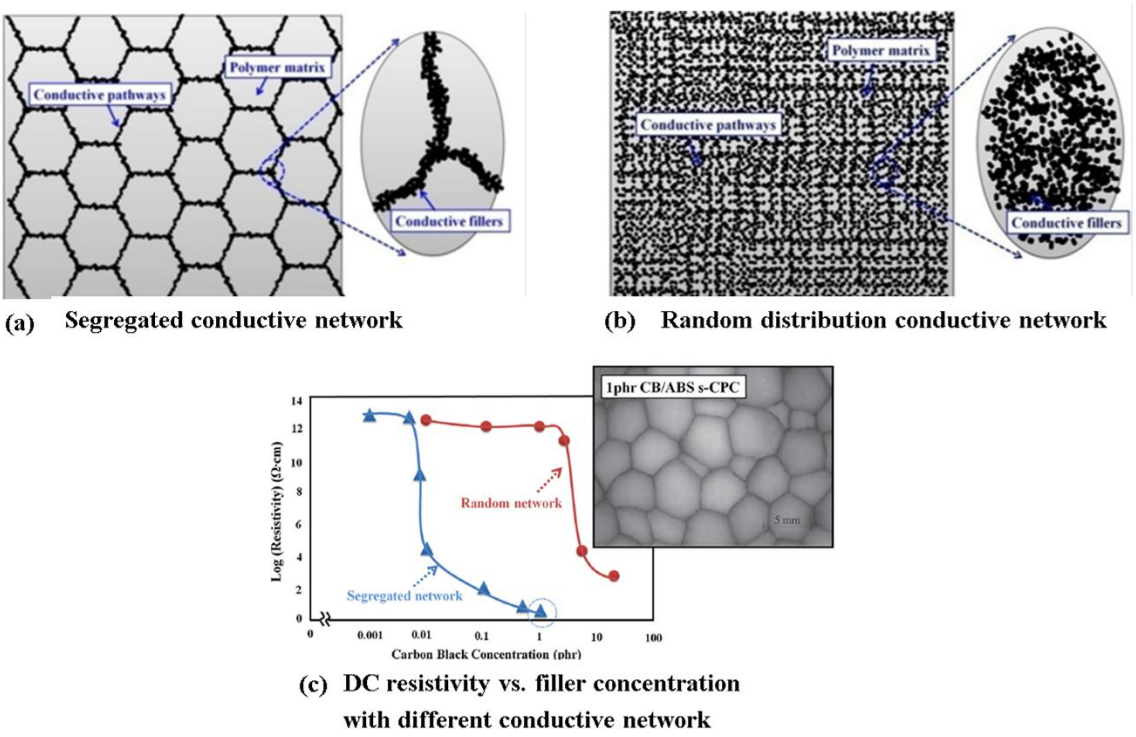

Figure 2.1. (a) Schematic of a segregated conductive network, (b) random distribution conductive network and (c) Log DC resistivity vs. volume fraction of carbon black (CB)-PMMA composites with segregated network and random network. Modified from reference.[4, 19]

Figure 2.1 (c) shows DC resistivity of acrylonitrile-butadiene-styrene (ABS) matrix conductive composite containing carbon black (CB) as a filler.[19] The composites containing phase segregated percolation networks show much lower percolation threshold than that of the composite with randomly distributed CB. The percolation threshold in this composite was 0.0054 vol %, which is the lowest value for CB-based polymer matrix conductive composites in the available literature.[19]

2.1.2 Processing and Properties of Conductive PMCs

2.1.2.1 Effects of Processing Methods

Many processing techniques such as melt blending,[21] solution blending,[21, 22] in-situ polymerization,[23] latex blending[24] and mechanical blending [10, 25, 26] have been used to fabricate polymer matrix conductive composites. One of the most common techniques in the industry is melt blending due to the simplicity of processing. Melt blending often results in a random distribution of conductive fillers, thus the percolation threshold can be as high as 20 vol % according to traditional percolation theory.[15, 27] It is not desirable to have such high percolation threshold because the conductive fillers are usually expensive, and high filler content results in poor processability due to the high viscosity. Additionally, other properties such as mechanical strength, thermal stability and optical properties might also be traded off due to inhomogeneity between the phases.[25] Despite the recent success of making phase segregated conductive composite using selective dispersion of conductive fillers at the interfaces of immiscible polymer blends (Fig. 2.2 (e-f)),[28] forming a stable segregated conductive network using melt blending is much more difficult than with the other techniques.[4]

Figure 2.2 shows schematics of different fabrication techniques that can achieve phase segregated conductive networks in the polymer matrix composites. One of the most

useful fabrication methods currently being studied is mechanical blending followed by compression molding (Figs. 2.2 (a-b)), because it has shown the lowest percolation threshold to date (< 0.0054 %), where the electrical conductivity increases by several orders of magnitude.[19] Gerhardt et al. reported this behavior on several insulator-conductor composite systems previously, i.e. obtaining electrical percolation at low concentration of fillers.[10, 25, 26]

The second main processing method to form a phase segregated conductive network is latex mixing (Figs. 2.2 (c-d)), which involves dispersion of the conductive fillers within a polymeric latex. The conductive fillers are confined within the internal space between the polymer latex particles during freezing-drying processes.[24] There are some advantages in latex mixing over solution blending, which is shown in Figs. 2.2 (e-f). A relatively stable phase segregation can be achieved and it is environmentally friendly when only water is used as a solvent. However, the manufacturing process is relatively more complex compared to mechanical mixing or melt mixing technique and selection of matrix polymer and filler material is limited.[4]

Another interesting processing method is termed miscible solvent mixing and precipitation (MSMP) method (Figs. 2.2 (g-h)).[29] This method consists of mixing conductive filler suspensions and polymer solutions in a miscible solvent. By having the polymer not miscible in the filler suspension, there is filler/polymer nanocomposite precipitation with the segregated filler networks. However, forming a stable segregated conductive network is less efficient than with the mechanical and latex blending techniques.

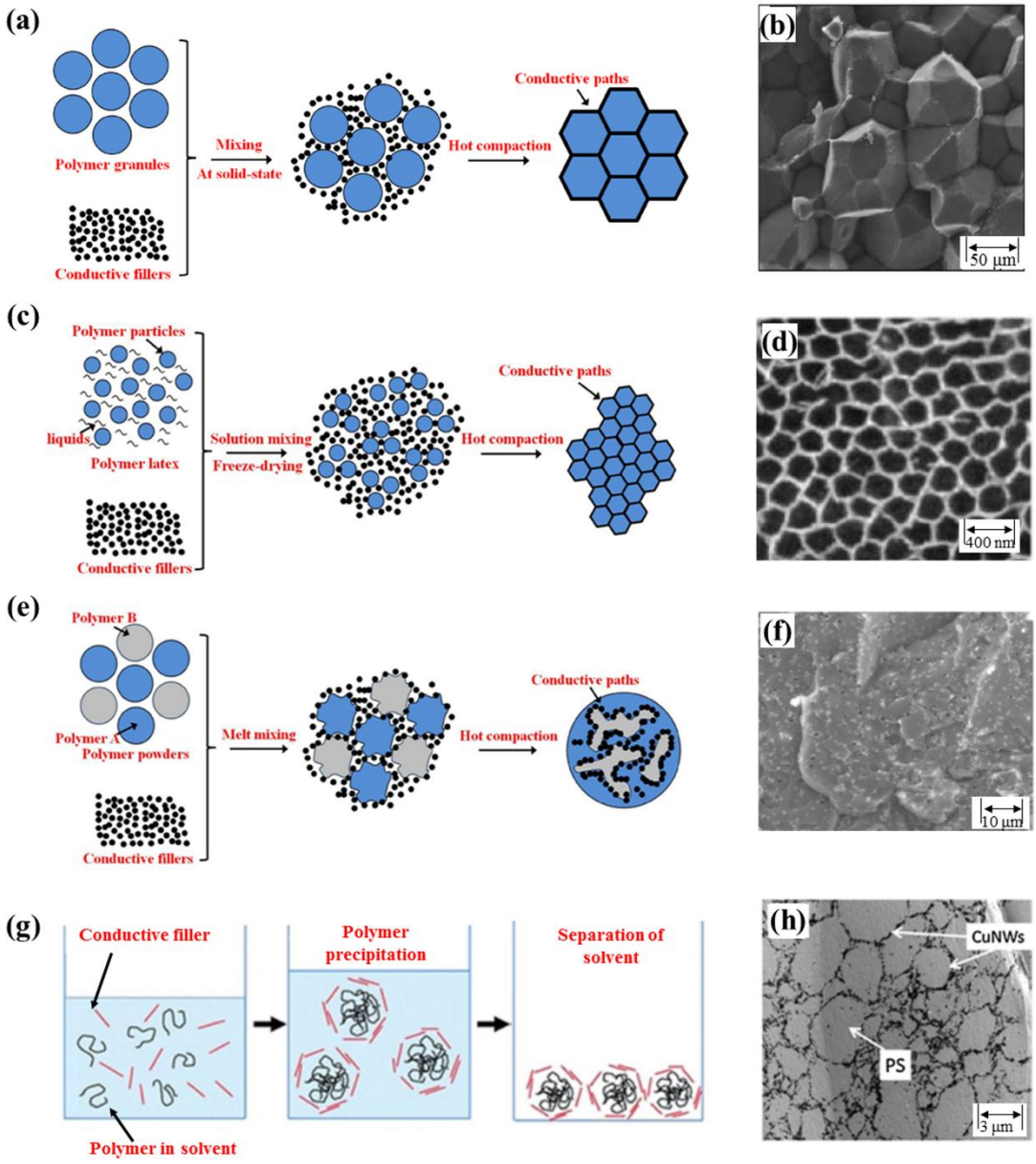

Figure 2.2. Schematics of methods used for fabricating conductive nanocomposites with phase segregated microstructure followed by microstructural images: (a-b) mechanical blending,[30] (c-d) latex technology,[24] (e-f) melt blending[21] and (g-h) miscible solvent mixing and precipitation.[29] Schematics in (a, c, and e) were modified from reference.[4]

2.1.2.2 Effects of Processing Temperature and Pressure

For some polymer matrix composite systems, the increased compression molding pressure could improve the contact between the filler particles resulting in better electrical conductivities.[31] However, the processing pressure can also be detrimental to

the phase segregated percolation network when high enough pressure is applied to the composites. The applied pressure can allow the polymer to flow into the capillaries between the filler particles and break up the network.[10]

Capozzi and Gerhardt summarized the influence of processing pressure on the DC conductivity of polymer matrix conductive composites as a function of filler (ITO) content (Fig. 2.3).[10] As the pressure is increased from 6.4 to 25.6 and 51.3 MPa, the conductivity of the composites decreased especially for the composites with filler concentrations above the percolation threshold and the percolation threshold (ρ_c) shifted to higher filler content. The polymer matrix composites fabricated by mechanical blending or latex blending followed by compression molding can be more susceptible to the processing pressure because high melt viscosity is required to preserve the segregated conductive networks in those composites.

For the same reasons, compression molding temperature will also affect the electrical conductivity of the composites because the high processing temperature lowers the melt viscosity of the polymer during processing.[22, 32] To the best of our knowledge, there is no single trend of the effects of processing conditions on the electrical percolation of polymer matrix composites. Unlike Capozzi, Bouchet et al. showed the DC conductivity of the specimens increased as the processing pressure was increased.[33] The effects of processing temperature and pressure are different by composite systems and dependent on many factors including the matrix and the filler materials and the processing techniques used.

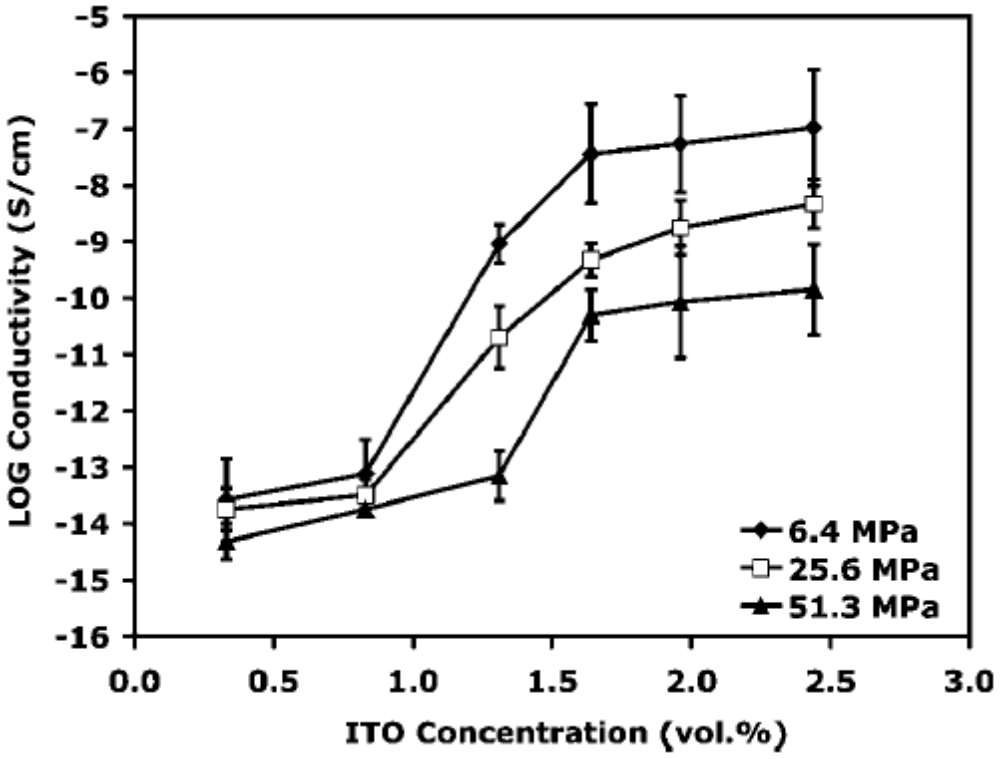

Figure 2.3. Effects of compression molding pressure on the DC conductivity of PMMA/ITO composites as a function of ITO concentration.[10]

2.1.3 Effects of Host and Filler Materials on Electrical Properties

It is not just the fabrication method that influences the percolation threshold, but the characteristics and the size of the matrix and the fillers used that can also critically affect the percolation behavior.[4, 6, 18, 19, 24, 30, 34] The percolation curves shown in Fig. 2.4 clearly demonstrate that the size of the matrix polymer controls the percolation threshold for the same filler type and processing procedure. The lowest percolation threshold was achieved with the largest polymer micro-spheres and the largest percolation threshold was obtained with the smallest polymer micro-spheres.[34]

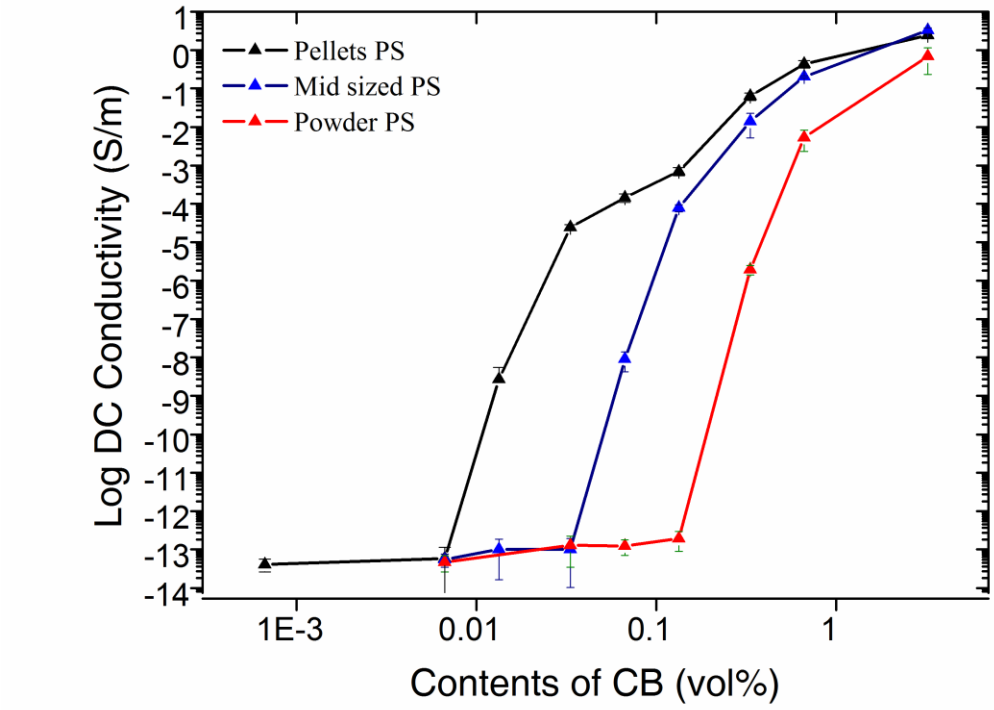

Figure 2.4. Effects of matrix microsphere size on the electrical conductivity of polystyrene-carbon black composites as a function of carbon black. Modified from reference.[34]

The characteristics of the polymer matrix can also affect the percolation threshold of the composites. Figure 2.5 shows the effects of matrix polymer on the formation of the segregated network and the resultant electrical conductivity of composites.[4, 24] In the composites with hard latex polymer, which has glass transition temperature (T_g) of 28 ℃ (Figs. 2.5 (b-c)), the polymer latex particles are progressively deformed to fill the voids in a segregated network during solvent evaporation. [24] In the composites with soft latex polymer, which has the glass transition temperature (T_g) of -50 ℃ (Figs. 2.5 (d-e)), polymer diffusion across boundaries of the latex particles takes place. The fillers partially diffuse into the latex particles to form a continuous and random network.[24]

The following percolation threshold in Fig. 2.5 (a) shows much lower value in the composite with a hard latex polymer as expected.[24]

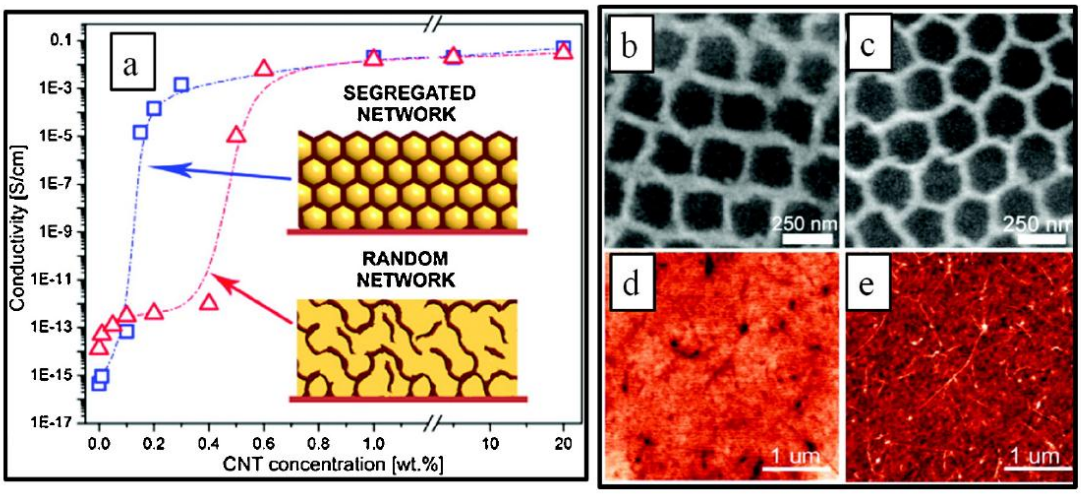

Figure 2.5. Effects of matrix polymer on the formation of segregated network and following electrical conductivity of composites. (a) Electrical conductivity of soft latex (red triangles) and hard latex (blue squares) as a function of CNT concentration, (b-c) SEM images of the hard latex composites and (d-e) atomic force microscopy (AFM) topography of the soft latex composites.[4, 24]

The percolation threshold of the polymer matrix composites with the phase segregated networks tends to increase with a larger particle size ratio between the matrix and the filler (r_{filler} / r_{matrix}). Figure 2.6 shows the generalized percolation threshold as a function of the size ratio between the matrix and the filler (note that R1 and R2 are of the radiuses of the matrix and the filler respectively in Fig. 2.6). The smaller the size ratio between the matrix and the filler (r_{filler} / r_{matrix}), the smaller the percolation threshold of the phase segregated composites is achieved.[8] In general, it is favorable to have the filler as small as possible and the matrix as relatively large (micron-sized), when making the phase segregated percolation networks using mechanical blending or latex blending to lower the percolation threshold.

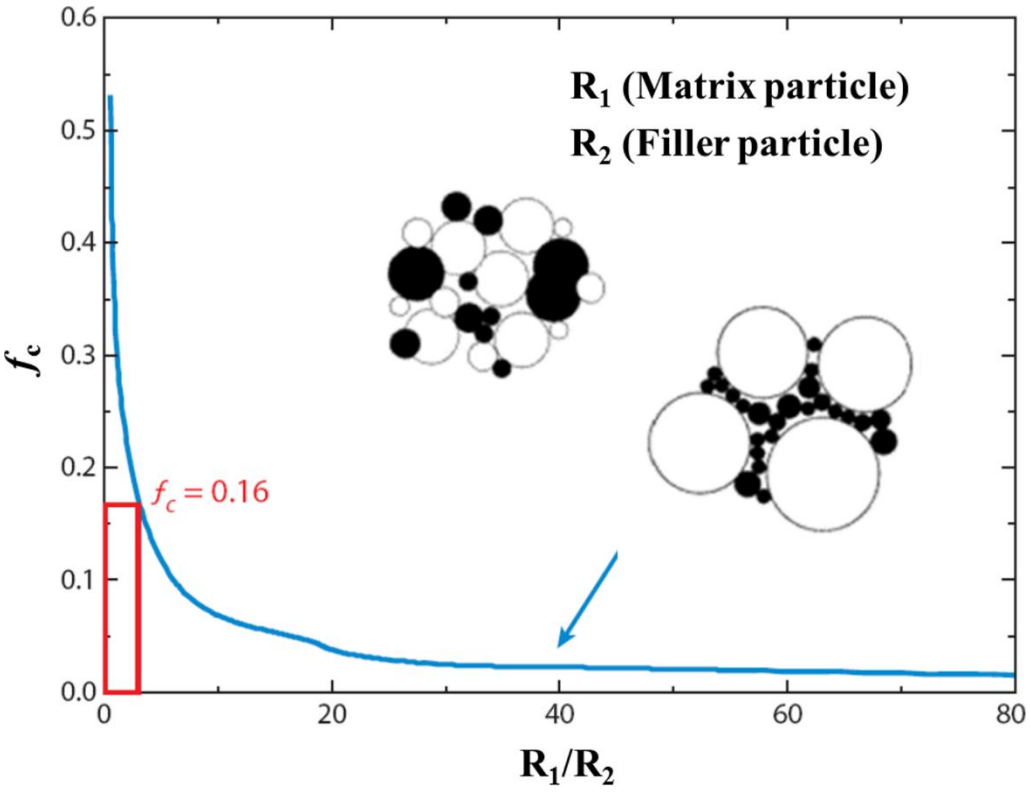

Figure 2.6. Effects of the particle size ratio between the matrix and the filler on the percolation threshold (f_c).[9] A cartoon inset shows the difference in particle size of the matrix and the filler.[35]

The percolation behavior can also be affected by the geometry of the fillers. Figure 2.7 shows the effects of the filler geometry on the percolation behavior of the segregated conductive networks. Figures 2.7 (a-b) show SEM images of the fractured cross-sections of CNT-HDPE and graphene nano sheet (GNS)-HDPE composites. Although the images do not show the overall distribution of the percolation networks in the matrix, MWCNTs are more ramdomly distributed within the percolation networks, while more aggregation can be observed for the GNSs.[36] Figure 2.7 (c) shows the corresponding electrical conductivity of the composites as a function of filler concentration (black diamonds show CNT and red stars show GNS.[36] The percolation threshold in the CNT-HDPE composites was lower than that of the GNS-HDPE composites. As a two-dimensional material, GNSs are more difficult to interlace to others and form network structures.[36] It is obvious that the filler geometry plays a critical role

in determining percolation behavior, however, the effects of the filler geometry on the electrical percolation can also be highly processing technique sensitive.

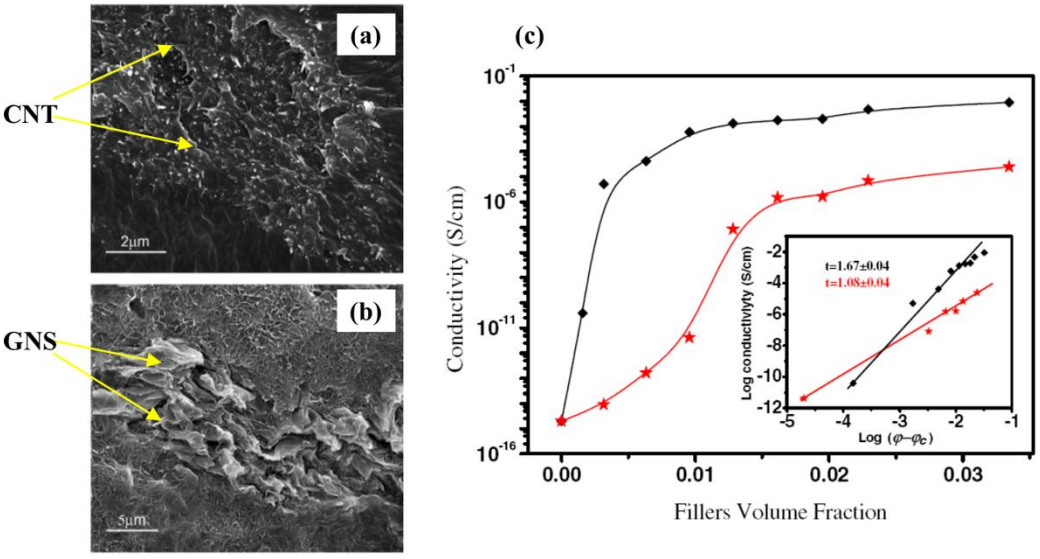

Figure 2.7. Effects of filler geometry on the dimensionality of the segregated conductive networks: SEM images of fractured cross-sections of (a) CNT-HDPE and (b) GNS-HDPE composites and (c) the following electrical conductivity of the composites as a function of filler concentration (black diamonds show CNT and red stars show GNS.[36]

2.1.4 Applications of Conductive PMCs

Polymer matrix conductive composites can be used as anti-static materials, electromagnetic interference (EMI) shielding, sensors and conductors, because of ease processing, low-cost, and tunable electrical properties in comparison to intrinsic conducting polymers.[5, 25, 37-39] The electrical resistivity (conductivity) of the polymer matrix composites determines their specific applications. Figure 2.8 shows the classification of conductive polymer composites according to their electrical resistivity (conductivity) and application ranges. For example, the conductive PMCs for electrostatic dissipation in plastic fuel tanks typically require an electrical resistivity of ~ 10^6 Ω·cm (10^{-4} S/m),[4] while EMI shielding requires electrical resistivity values below 10^2 Ω·cm (1 S/m)[37]

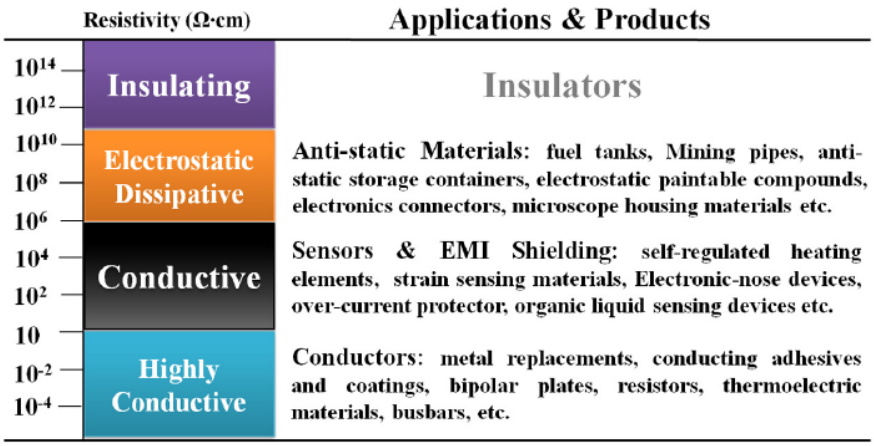

Figure 2.8. Classification of conductive polymer composites according to their electrical resistivity and application ranges.[4]

2.1.5 Background on Materials to be Made Into Conductive Composites in this Dissertation

2.1.5.1 Antimony Tin Oxide (ATO)

The filler material in this study will be antimony tin oxide (ATO), which is a transparent conducting oxide (TCO) like ITO.[40] ATO is considered as a potential replacement for ITO because of its much lower cost,[41] although the electrical conductivity and the optical transmittance of ITO are higher than those of ATO. However, ATO has better performance as an antistatic agent compared to carbon black and other metallic pigments.[42] Currently, ATO is not as widely used as ITO because ATO is not easily sintered to full density due to some non-densifying sintering mechanisms including surface diffusion, evaporation-condensation and a high vapor pressure for temperatures over 1000℃, which are temperatures needed for sintering.[35, 43] ATO can be considered as a good filler material for polymer composites considering its

reasonable electrical conductivity, optical transmittance as well as good antistatic performance.

Tin oxide (SnO_2) has a rutile structure where the tin atoms occupy the corner and center positions of the unit cell and the oxygen atoms are located at the tetrahedral interstitial sites in the unit cell.[40] Without Sb doping, tin oxide itself is a wide-band gap (~3.6 eV at RT) semiconductor.[40] The addition of antimony oxide (Sb_2O_3) to tin oxide (Sn_2O_3) results in higher electrical conductivity (from 10^{-5} to 10^6 S/cm).[41] The main mechanism as to the origin of the increase in the electrical conductivity is the possibility of two different oxidation states for antimony. At a low doping level (< 10%), Sb^{5+} is the main oxidation level,[44] which results in higher electrical conductivity due to more free electrons being produced. With this doping, the material acts as a degenerate semiconductor exhibiting metallic conduction properties.[41] Figure 2.9 shows a unit cell of rutile tin oxide showing antimony cation interstitial sites.[45, 46]

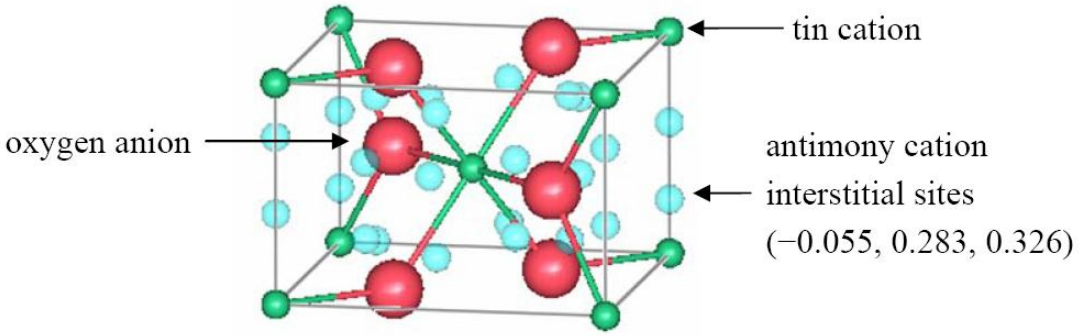

Figure 2.9. A unit cell of rutile SnO_2 showing the location of interstitial antimony.[45, 46]

2.1.5.2 Poly(methyl methacrylate) (PMMA)

PMMA is a widely used matrix material in polymer-matrix composites.[6, 10, 23, 30, 47]. The glass transition temperature and coarsening mechanisms of PMMA play an important role in the processing of the PMMA for polymer-based composites.[18] It is a

well-known amorphous material with a glass transition temperature in the range of 100-120 ℃.[48, 49] The molecular structure of PMMA is shown in Figure 2.10.

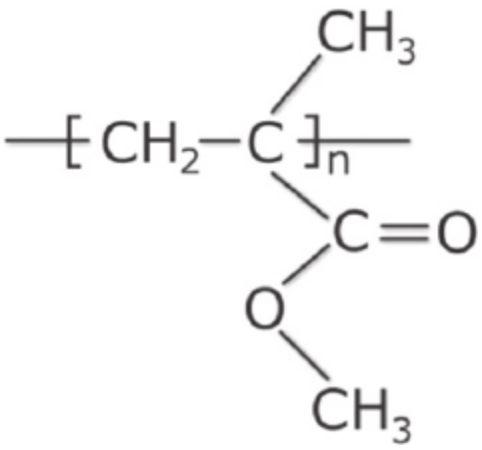

Figure 2.10. Molecular structure of PMMA

The viscosity of PMMA as a function of the inverse absolute temperature normalized by glass transition temperature (T_g) together with data for PS and PC is shown in Fig. 2.11. The viscosity sharply increases with decreasing temperature below and near its glass transition temperature. The rapid increase in the viscosity gradually slows down as the temperature further decreases.[49] The zero-strain rate viscosity of polymer matrix follows the Vogel-Tammann-Fulcher (VTF) formula when the temperature is above the glass transition temperature,[49] which is represented as

$$\eta = A\exp[B / (T - T_0)] \tag{2.2}$$

where A, B, and T_0 (VTF temperature) are the fitting constants.

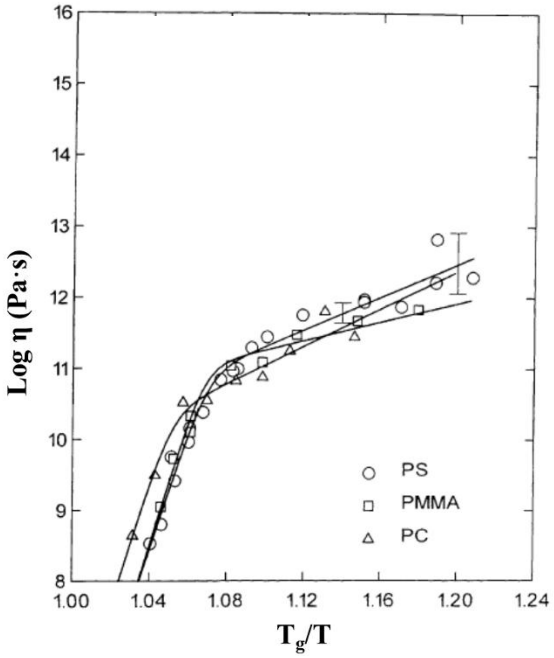

Figure 2.11. Temperature dependence of viscosity(η) below and near glass transition temperature for some common polymers.[49]

2.2 Dielectric Nanocomposites with Uniformly Distributed Nanoparticles

2.2.1 Fundamental Aspects of High-*k* PMCs

2.2.1.1 Polarization and Relaxation Behavior in High-*k* PMCs

A dielectric material literally means a material which does not permit the passage of electric field or flux. Dielectric materials undergo dielectric and/or electric polarization with an applied electric field. Dielectric polarization can result from the orientation of existing dipoles toward the direction of an applied electric field or via the separation of mobile charge carriers at the interface between a dielectric material and an electrode surface. This phenomenon can also be considered as the orientation of the dipole moments of polar molecules if a material contains polar molecules. Figure 2.12 illustrates the polarization of a dielectric medium in between parallel plates. Because of dielectric polarization, positive charges are displaced toward the field and negative charges are

shifted in the opposite direction. This creates an internal electric field that decreases the effective electric field between the plates as follows:

$$E_{effective} = E - E_{polarization} = \frac{\sigma}{k\varepsilon_0} \tag{2.3}$$

where ε_0 is the permittivity of free space (8.854 x 10^{-12} F/m), σ is the conductivity of the dielectric medium. The factor *k* by which the effective field is decreased by the polarization of the dielectric is called the dielectric constant or relative permittivity (ε_r) of the material. A dielectric material with a higher *k*, shows a higher ratio of electric flux to charge than empty space.

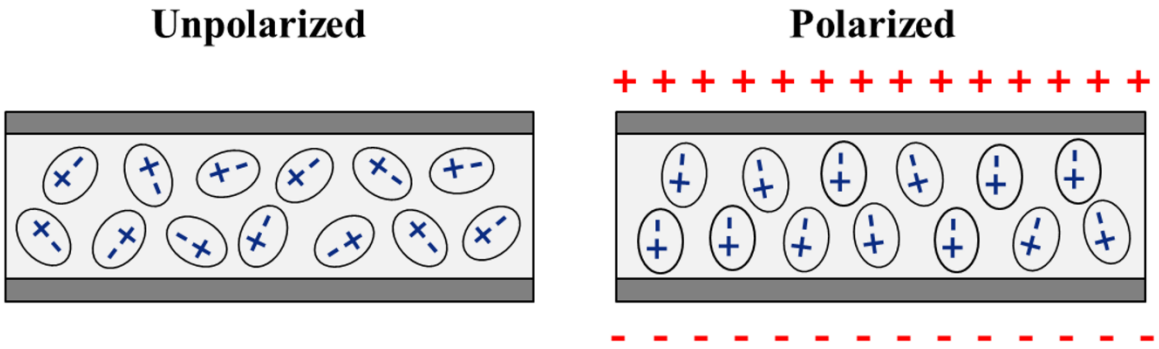

Figure 2.12. A dielectric medium showing a random orientation when no electric field is applied (left) and a polarized orientation of charged particles when an electric field is applied.

In general, the permittivity of a dielectric material depends on the frequency in Hertz (Hz) of the applied electric field and can be described as a complex physical quantity, where the imaginary part is related to charge dissipation or dielectric loss. The frequency dependence of the permittivity of a dielectric material reflects the possible existence of dispersive behaviors somewhere in the electromagnetic spectrum.[5] The relative dielectric permittivity is a frequency dependent complex quantity.

$$\varepsilon^* = \varepsilon' - j\varepsilon'' \tag{2.4}$$

where ε' and ε'' are the real and the imaginary permittivities of the dielectric medium respectively.

The real permittivity always has a non-zero value and represents the contribution to the polarization responsible for the energy storage in the material. The relative permittivity is often used to describe a material's property independent from the electric field. The imaginary permittivity, loss factor, shows possible dissipative effects and its frequency spectrum differs from zero only in dispersive regions. Sometimes, the dissipative behavior is characterized by means of the so-called loss tangent, which is defined as

$$Loss\ tangent = {\varepsilon''}/{\varepsilon'} \tag{2.5}$$

As the polarization of a material under an applied electric field varies, some of the field energy is dissipated due to charge migration (i.e., conduction) or conversion into thermal energy (e.g., molecular vibration). To exploit the applications of a dielectric material, the dielectric loss should be kept as low as possible. In fact, losses not only waste part of the input energy, but also worsen the insulation properties of the materials.[5]

There are four mechanisms in the dielectric polarization depending on the origin of polarization, which have different response times: electronic polarization, atomic or ionic polarization, dipolar (orientational or rotational) polarization, and interfacial or space charge polarization, which is particularly associated with mobile and trapped charges (Fig. 2.13).

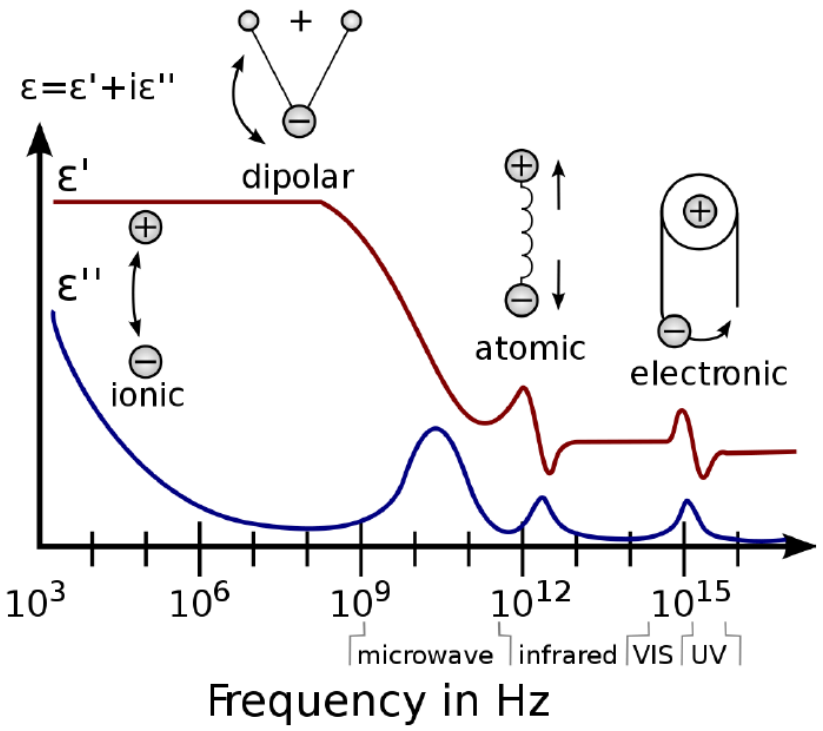

Figure 2.13. A dielectric permittivity spectrum over a wide range of frequencies. The real and imaginary parts of permittivity are shown, and various mechanisms are depicted: ionic and dipolar relaxation, and atomic and electronic resonances at higher energies in terms of the real and imaginary parts of the permittivity. (copyright Prof. Kenneth A. Mauritz, Univ. Southern Mississippi)

Electronic polarization refers to the polarization caused by the deformation or the translation of the originally neutral electron clouds of atoms or molecules by the external electric field.[50] This polarization is not permanent and is dissipated once an applied electric field is removed. Ionic polarization is polarization caused by relative displacements between positive and negative ions in ionic crystals.[50] Atomic polarization is related to the displacement of atoms to each other under the influence of an electric field.[50] Dipolar polarization is related to dipolar molecules or particles possessing permanent dipole moment.[50] If an electric field is applied, the distance between charges within each permanent dipole remains constant, because it is related to chemical bonding; however, the direction of polarization rotates. The net dipole moment would return to zero, once the electric field is removed, because thermal

agitation tends to randomize oriented dipoles. This rotation occurs on a timescale depending on the surrounding local viscosity of the molecules, while the electronic and ionic polarization are associated with the displacement of electron clouds and lattice vibration within atoms or molecules respectively. Therefore, dipolar polarization involves a momentary delay which is known as a relaxation process.

Interfacial or space charge polarization is related to movement of charge carriers (ions, holes or electrons) applied from electrical contacts or formed at the interfaces of materials with different charge transport properties.[50] The accumulated charges distort the electric field distribution and thus affect the relative permittivity and the breakdown strength of a material. The interfacial polarization is important in heterogeneous or multiphase composite materials, such as ceramic/polymer nanocomposites, multi-layered structures, and porous materials. There have been tremendous efforts to modulate the dominant interfacial polarization by improving the filler/polymer interfaces.[51, 52]

There are two main types of dielectric polarization: resonance and relaxation. Resonance is associated with the vibrations of electrons, atoms or ions. Electronic and atomic or ionic polarizations are examples of resonance. A resonance phenomenon will occur when the frequency of the excitation field is close to the natural frequency of the vibration of the oscillation system. Relaxation is related to the movements of charges. Dipolar and interfacial or space charge polarizations can be classified as relaxation. A relaxation phenomenon occurs during a polarization or a depolarization process because the movement of charge carriers occurs on a time scale and often shows time delay.[53]

2.2.1.2 Capacitance and Electric Energy Storage in High-*k* PMCs

A parallel plate capacitor with area A and thickness d has a capacitance given by:

$$C = \varepsilon' A/d = \varepsilon_0 \varepsilon_r A/\mathrm{d} \tag{2.6}$$

The energy stored by a capacitor is given by:

$$W = \frac{1}{2} C {V_{bd}}^2 \quad (2.7)$$

where V_{bd} is the breakdown voltage. In terms of the dielectric constant (ε_r), the volumetric energy density of a dielectric capacitor is:

$$\widetilde{W} = \frac{W}{Ad} = \frac{1}{2} \varepsilon_0 \varepsilon_r \left(\frac{V_{bd}}{d}\right)^2 = \frac{1}{2} \varepsilon_0 \varepsilon_r {E_{bd}}^2 \quad (2.8)$$

where E_{bd} is the breakdown field strength. Despite having high dielectric constants, ceramic capacitors have low inherent breakdown field strength, which results in low energy density.

2.2.1.3 Breakdown Strength in High-*k* PMCs

According to equation 2.8, both the high dielectric permittivity and the high breakdown strength are required for obtaining high energy density. Dielectric breakdown is the catastrophic failure of an insulating material under an external applied field resulting in a rapid reduction in the resistivity of an insulator and mechanical damage. A general consensus of dielectric breakdown strength in polymers is related to the dissociation of polymer molecules under an external electric field.[54] However, the exact mechanism of dissociation is not clear. There are two types of mechanisms in the dielectric breakdown of solids; thermal and electrical breakdowns.[55] Thermal breakdown refers to failure due to joule heating and thermal excitation arising from conduction currents and dielectric losses under an applied electric field.[12] Electrical breakdown includes intrinsic and avalanche mechanisms.[55] Intrinsic breakdown strength means the "true" breakdown strength of a material depending only on the material and the temperature. An ideal insulating material is believed to show its intrinsic breakdown strength when an external electric field is high enough to raise electrons from the valence band to the conduction band.[12] Avalanche or ionization breakdown, which is believed to

be one of the most common breakdown mechanisms in polymers, occurs when free electrons in an insulating material gain high enough energy by accelerating along the mean free path to knock out other electrons. The charge carrier multiplication occurs in the conduction band leading to conduction. It is believed that the initial stage of breakdown is due to the combination of thermal and avalanche processes, but the final catastrophic breakdown is mainly due to the thermal process.[53] A recent study revealed that the breakdown strength of the polymer matrix composite can be remarkably enhanced by using boron nitride (BN) nano-sheets, which has high intrinsic thermal conductivity to control heat and leakage current.[56, 57]

2.2.2 Theoretical Models for Dielectric Properties

There are many theoretical models to predict effective dielectric constant of the high-*k* PMCs. The volume-fraction average method is one of the simplest methods but it is quite inaccurate. For any two-phase PMCs, the lower permittivity can be described as a series model as:

$$\varepsilon_{c.min} = \frac{\varepsilon_m \varepsilon_f}{\varepsilon_m \emptyset_f + \varepsilon_f \emptyset_m} \tag{2.9}$$

where ε_m and ε_f are the permittivity of the matrix polymer and the filler respectively and $\emptyset_m$ and $\emptyset_f$ are the volume fractions of the matrix polymer and the filler respectively. The upper permittivity can be described as a parallel model:

$$\varepsilon_{c.max} = \varepsilon_m \emptyset_m + \varepsilon_f \emptyset_f \tag{2.10}$$

For a given system, the dielectric constant must be in between these bounds.

More realistic models are based on mean field theory. Maxwell-Garnett equation calculates dielectric permittivity of composites from dispersed spherical fillers in the matrix:[58]

$$\varepsilon_c = \varepsilon_m \left[1 + \frac{\emptyset_m(\varepsilon_f - \varepsilon_m)}{A(1-\emptyset_f)(\varepsilon_f - \varepsilon_m)+\varepsilon_m}\right] \quad (2.11)$$

Another mean field theory, known as the Bruggeman model, considers the two-phase composites as repeated unit cells of the matrix and the spherical inclusions in the center. The effective dielectric permittivity (ε_c) is given by:[59]

$$\emptyset_m \left(\frac{\varepsilon_m - \varepsilon_c}{\varepsilon_m + 2\varepsilon_c}\right) + \emptyset_f \frac{\varepsilon_f - \varepsilon_c}{\varepsilon_f + 2\varepsilon_c} = 0 \quad (2.12)$$

Various studies have shown that the effective permittivity of high-*k* PMCs predicted by Bruggeman model sharply increased for filler volume fractions above 20 %.[12]

More theoretical models exist to explain the role of the interface between the polymer matrix and the filler because the interface plays an important role in determining the properties of the dielectric materials. Some models treat the interphase as a separate phase.[12, 60] The Jaysundere-Smith (J-S) model includes an induced electric field with a filler sphere embedded in a continuous dielectric medium considering polarization of adjacent particles and results in the following equation:[61]

$$\varepsilon_c = \frac{\varepsilon_m \emptyset_m + \varepsilon_f \emptyset_f \frac{3\varepsilon_m}{2\varepsilon_m + \varepsilon_f}\left[1 + 3\emptyset_f \frac{(\varepsilon_f - \varepsilon_m)}{2\varepsilon_m + \varepsilon_f}\right]}{\emptyset_m + \emptyset_f \frac{3\varepsilon_m}{2\varepsilon_m + \varepsilon_f}\left[1 + 3\emptyset_f \frac{(\varepsilon_f - \varepsilon_m)}{2\varepsilon_m + \varepsilon_f}\right]} \quad (2.13)$$

When a conductive filler is used in the high-*k* PMCs, a percolation model can be used to predict the dielectric permittivity of PMCs. The use of conductive fillers is originated from the fact that they can also increase interfacial polarization, not just to increase electrical conductivity. In general, the dielectric permittivity sharply increases when the conductive filler volume fraction exceeds the percolation threshold (ρ_c) of that composite system. When the filler volume fraction is below ρ_c, the conductive fillers are separated by the insulating medium and the electric properties of PMCs are determined by the matrix region. As the filler fraction increases, local clusters of fillers are formed.

The localized clusters form a localized percolation network, increasing electrical conductivity and the interfacial polarization. The dielectric permittivity of PMCs using conductive fillers often follows the relations below:

$$\varepsilon_c \propto (\rho_c - \rho)^{-q} \tag{2.14}$$

where ρ_c is the percolation threshold and q is the critical exponent in the insulating region which normally has a value of 0.8-1.[62] Although there are many numerical models, the current existing models do not predict the dielectric properties well enough, due to complexities in microstructure, composition, and interfaces of the high-*k* PMCs.[5]

2.2.3 Effects of Microstructure and Interfaces on Dielectric Properties

Polymer matrix high-*k* composites usually consist of two or more phases. Thus the microstructure, compositions and interfaces between the constituent phases are crucial to obtain the desired properties.[63] As filler particles approach one another, there is steric interaction which requires distortion of the polymer chain conformation and increases the conformational entropy, especially when the inter-particle distance is close to or shorter than the radius of gyration of the polymer chains.[63] A semi-crystalline polymer would experience more interaction force.[5] Moreover, induced electrical field from the distribution of dipole moment is no longer negligible when calculating the overall field locally experienced in the matrix, when a ferroelectric filler is dispersed in the matrix polymer.[5] Thus, the microstructure should be carefully assessed when evaluating the performance of PMCs.

A common approach for fabrication of PMCs is to incorporate high-*k* ceramic fillers into a polymer matrix. A variety of polymers have been used as a matrix. In particular, PVDF [64, 65], its copolymers [65, 66] or terpolymers [66] have been investigated due to their higher permittivity than that of other polymers. Some high dielectric constant ceramics, such as barium titanate ($BaTiO_3$), barium strontium titanate ($Ba_{0.2}Sr_{0.8}TiO_2$) [67]

and calcium copper titanate ($CaCu_3Ti_4O_{12}$)[68] have been chosen as fillers. Most of all, a uniform distribution of high-*k* ceramic fillers into the hosting polymers effectively increases the dielectric permittivity of the composites.

Figure 2.14 summarizes different microstructures of high-*k* PMCs. To achieve a uniform dispersion of BT NPs in the polymer matrix, Xie et al. highlighted the core@double-shell structured nanoparticles with up to 56.7 wt % of BT in which the first shell is hyper-branched aromatic polyamide (HBP) and the second shell is PMMA to have high dielectric constant and low dielectric loss nanocomposites for energy storage application (Fig. 2.14 (a)).[69] There have been great efforts to enhance dielectric properties of PMCs using high aspect ratio fillers.[70-72] Such 1-D fillers can help minimize filler loading to achieve desired properties (Fig. 2.14 (b)). Figure 2.14 (c) shows a highly aligned array of CNTs in the polymer matrix to enhance dielectric properties of the composite. When conductive materials are used as fillers, high permittivity is easily obtained near the percolation threshold of fillers in the polymer composites. Thus, the microstructure as well as the percolation structure, which are dependent on the size, shape and inter-particle distance, significantly affect the dielectric properties of PMCs. However, one of the critical challenges in using 1D/2D conductive fillers is that it is difficult to effectively disperse them in the matrix without agglomeration or formation of conductive percolation channels, which increase the leakage current, resulting in high dielectric loss and low breakdown strength. Figure 2.14 (d) shows a layered structure of a dielectric composite film. Such layered structure can be a useful solution for obtaining high-*k* transparent composite films, because the conductive interlayer in the film forms a space charge layer at which an accumulation of polarized charge carriers near the conductive filler occurs, resulting in an induced space charge polarization and enhanced dielectric constant.[73]

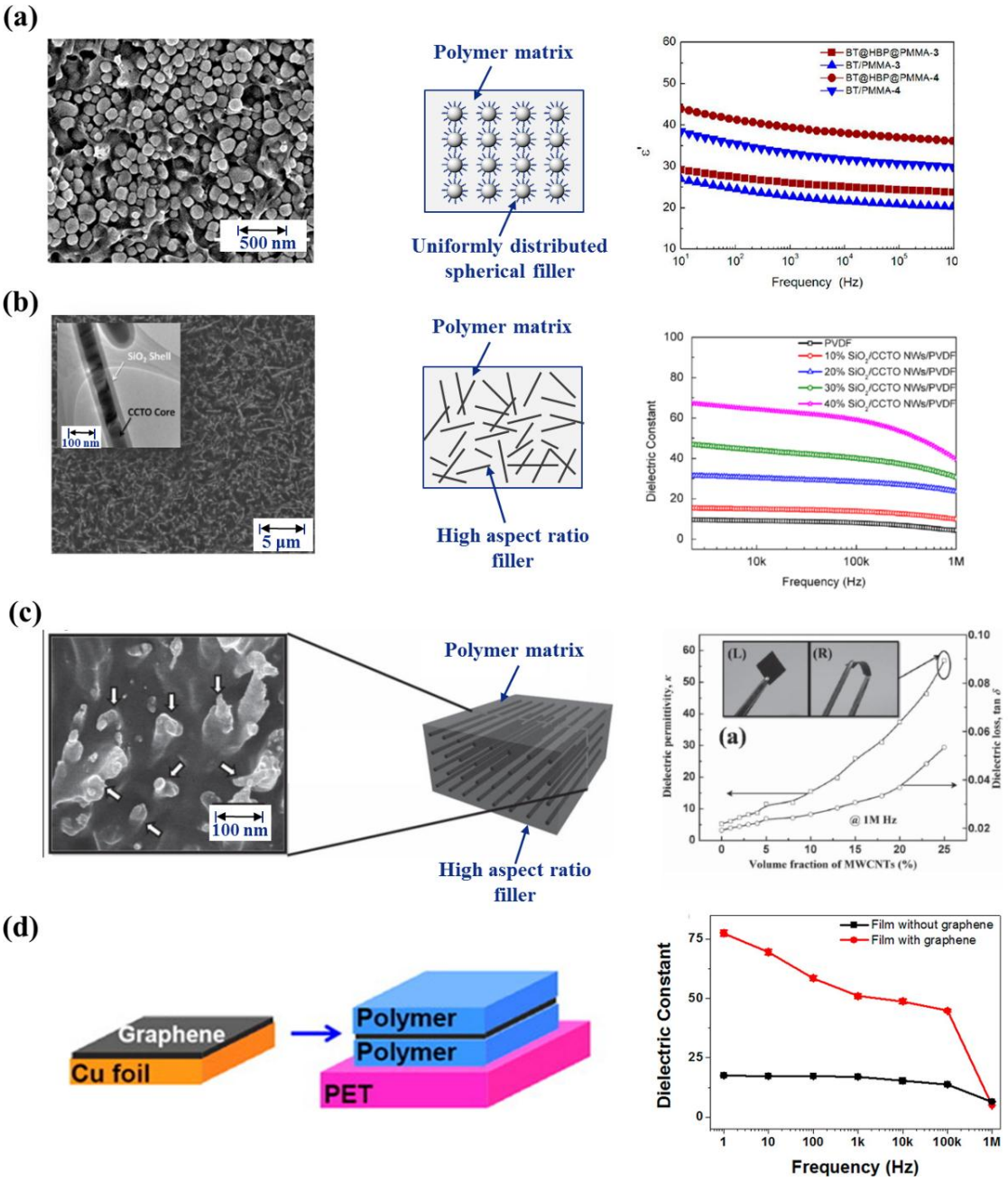

Figure 2.14. Effects of microstructure and interfaces of the matrix and the filler on the dielectric properties of composites: (a) core-shell structure with spherical filler,[69] (b) randomly distributed high aspect ratio filler,[72] (c) highly aligned conductive nanotubes,[74] and (d) layered structure with conductive interlayer.[73] Schematics in (a-b) were drawn by the author of this dissertation.

A tremendous effort has been put to enhance the dispersion of nanofillers into polymer matrices and to improve the interfaces between the phases. One of the effective ways is to create interfacial bonding between the phases prior to use. For these purposes, the surfaces of nano-fillers are often modified with some organic groups such as fluoro, amino, silanol and carboxylic.[11, 75, 76] This increase in interfacial bonding not only enhances the effective dispersion of nanotubes, but also improves the compatibility of the matrix and the filler phases at the interfaces, which, in turn, improves the dielectric properties. In a broad view, this approach can be classified as one of the core-shell strategies. Core–shell strategies are versatile for improving properties and processability of high-*k* PMCs for energy storage and dielectric applications. Figure 2.15 illustrates three methods for obtaining core-shell structures:[52] (1) direct use of core–shell nanoparticles prepared by "grafting from"; [23, 77] (2) direct use of core–shell nanoparticles prepared by "grafting to";[78-80] (3) using core–shell organic–inorganic nanoparticles as fillers.[81-86] It is also possible to use other types of core–shell nanostructured fillers such as BT/SiO_2 NPs, CCTO/SiO_2 NWs and BT/TiO_2 NWs.[51, 72, 87]

The "grafting from" method relies on the formation of nanocomposites by the in situ polymerization of monomers on initiator-functionalized surfaces of nano-fillers. Atom transfer radical polymerization (ATRP) and reversible addition-fragmentation chain transfer (RAFT) polymerization are feasible and powerful "grafting from" technique [52]. The "grafting to' method utilizes the formation of nanocomposites by grafting the pre-prepared polymer chains onto the surface of the nano-fillers via a reaction between the polymer end-groups and the functional groups on the nanoparticle surfaces.[52] The "grafting to" method has some advantages over the "grafting from" method in such a way that it allows us to control the composition and the molecular weight of the polymer chains for the desired properties of composites. These grafting methods have some advantages such as: (1) the agglomeration of nanoparticles can be prevented by the shell layer; (2) highly defect-free nanocomposites can be formed

directly from core–shell nanoparticles using the shell layer as a matrix, (3) polymer chains are robustly bonded on the nanoparticle surfaces, improving the interfaces between the matrix and the filler.[52] Other core-shell methods involve nanocomposites fabrication using core-shell structured nano-fillers. In these methods an organic-inorganic and an inorganic-inorganic core-shell structured nano-fillers can be prepared. The concentration of nano-fillers can be controlled and the fundamental role of the interface on the electrical properties of the nanocomposites can be analyzed and enhanced by optimizing the fabrication methods. Furthermore, the shell layer can work as a buffer layer that can be made in between the high-*k* or highly conductive core and the polymer matrix, resulting in the reduced local electric field distortion, lower dielectric loss and the enhanced breakdown strength of composites.[51, 52]

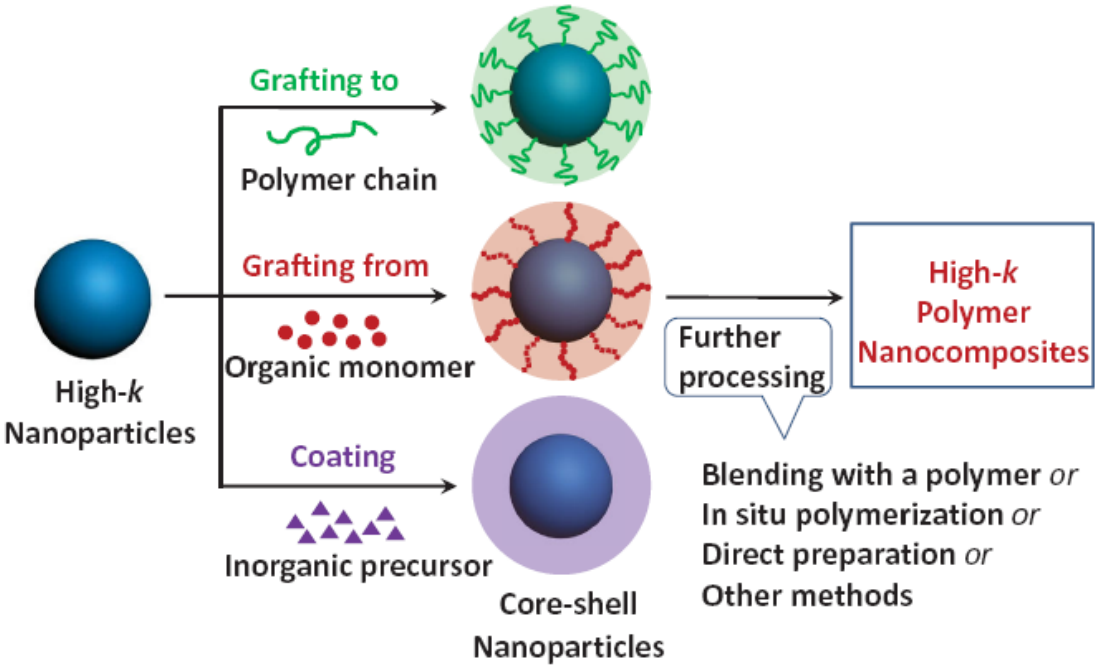

Figure 2.15. General methods associated with design and construction of core–shell nanoparticles for high-*k* polymer nanocomposites.[52]

2.2.4 Effects of Filler Materials on Dielectric Properties

2.2.4.1 Effects of High-*k* Ceramic Fillers Composition

The increase in the effective permittivity of PMCs is generally assumed to be due to the relatively high permittivity of inorganic fillers compared to the polymer matrix. As the filler concentration increases, the effective permittivity and dielectric loss of PMCs also increase. However, further increase in filler loading may decrease the effective permittivity of the composites due to agglomeration of filler particles, which results in increased porosity in the composites. In general, dielectric properties are based on compromise. The improvement of the dielectric permittivity of PMCs without sacrificing dielectric loss or breakdown strength for a given filler concentration requires: (1) effective dispersion of fillers, (2) minimizing pores, (3) improving the interfaces in the composites as well as (4) developing novel ceramic fillers with colossal permittivity. As the size of a filler particle decreases and becomes nanometer scale, the properties of PMCs are increased because they are determined by the interfaces due to high surface area of fillers.[63, 88] This concept is improved by effective dispersion of fillers and better compatibility between the matrix and the fillers using the core-shell approach.

Many inorganic high-*k* fillers have been used in dielectric PMCs. Barium titanate (BT) has been the most widely investigated material as a filler. After doping (using La, Mg or Sr), BT ceramics can show higher permittivity up to 25,000.[89] As a result, doped-BT/polymer composites can show higher effective permittivity than that of un-doped BT composites. Other ceramics with colossal permittivity (CP) were also investigated as fillers such as calcium copper titanate (CCTO).[68] The internal barrier layer capacitance (IBLC) is often believed to be the origin for the observed CP behavior in which the core of the grain is semi-conducting and the grain boundary layer is just electrically insulating (Fig. 2.16).[90] However, ceramic particles of nanometer scale are not large enough to have IBLC structure. More recently, a new type of a CP material, (Nb, In) co-doped

TiO_2, was developed based on electron pinned defect-dipoles.[91] In this new design, hopping electrons are confined by localized lattice defects, generating stable CP with low dielectric loss. If it is possible to have a colossal permittivity in nano-scale particles, it will be a good candidate as a filler.

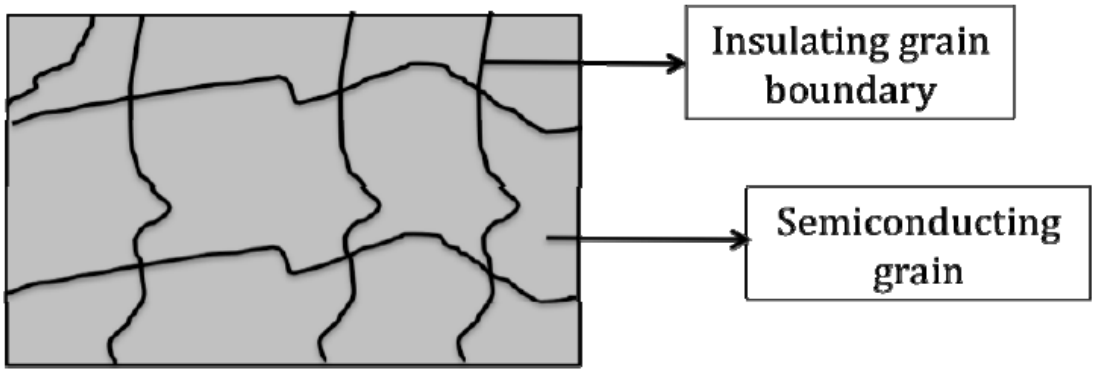

Figure 2.16. General schematics of the IBLC theory associated with CCTO's giant dielectric constant.[12, 90]

2.2.4.2 Effects of the Size and Shape of Fillers

Dielectric properties can be largely affected by the size of the fillers used. The effects of grain size on the dielectric properties in ferroelectric ceramics have been extensively studied.[92-94] However, the grain size effects on the bulk properties could be different from the particle size effects on the nano-sized fillers in the composite materials. There has been some works on the effects of the nano-particle size on the dielectric properties of polymer matrix composites.[95-97] Figure 2.17 shows some examples of particle size dependent dielectric properties of composites. The real permittivity is obviously dependent on the particle size; however, the trends are not always systematic. In general, fillers with smaller particle size should form more interfacial area with matrix materials, resulting in more interfacial polarization. However, the intrinsic dielectric properties of the filler itself is also affected by the particle size. Furthermore, the smaller particles are prone to agglomerate which makes it more difficult to effectively disperse

the filler particles in the matrix. The effective permittivity and the dielectric loss of PMCs are determined by the interactions between the matrix and the fillers, thus the surface conditions of the fillers can differently affect the dielectric properties of composites. The surface conditions of fillers can be different, depending on the particle synthesis roots, surface treatments and the composite fabrication methods.

To reasonably validate the filler size dependent dielectric properties of composites, the fillers have to be synthesized and treated by the same method and the composite fabrication method should guarantee the effective dispersion of the fillers without serious agglomeration and induced defects or voids.

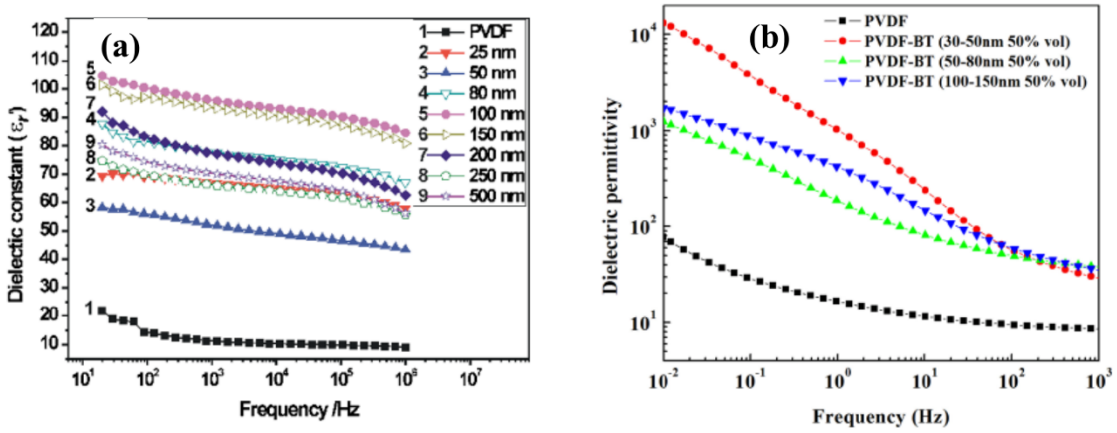

Figure 2.17. Effects of filler particle size in some PVDF/BT composite: (a) 60 vol % BT in PVDF[95] and (b) 50% BT in PVDF.[96]

The morphology, especially the aspect ratio of fillers can also largely affect the dielectric properties of composites. Nanowires have been widely investigated as fillers in the dielectric PMCs.[71, 98, 99] The high aspect ratio fillers with high dielectric permittivity can improve the dielectric properties of the polymer matrix composites with smaller loading. Figure 2.18 shows the effects of the aspect ratio of fillers on the dielectric constant of polymer matrix composites.[99] However, high aspect ratio fillers can be more susceptible to agglomeration than their spherical counterparts.

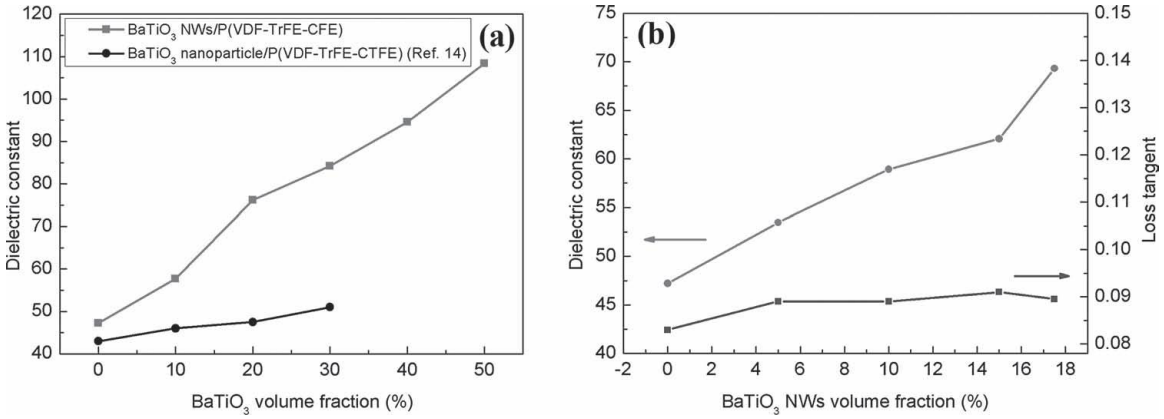

Figure 2.18. Dielectric properties of nanocomposites at 1kHz in terms of filler morphology and concentration.[99]

2.2.4.3 Effects of Organic / Inorganic Conductive Fillers

In recent years, conductive 1D or 2D materials have been incorporated into polymer matrices to prepare flexible high-*k* nanocomposites. Carbon nanotubes have been selected as fillers in the high-*k* composites. The incorporation of CNTs can substantially improve the dielectric permittivity of the composites when CNT content is approaching its percolation threshold.[100] However, CNTs tend to easily aggregate due to their high surface energy[101] and form percolation networks, which make it difficult to control the dielectric properties of the composites. To utilize CNTs as a filler, the effective dispersion of CNTs is essential, but it is hard to achieve. The uniform dispersion of CNTs is not simply achieved by surface modification or using surfactant.[102] There have been several works to improve the dispersion of CNTs in polymer matrix by the aids of simulation.[101, 103] However, experimental proof is yet to meet the requirements of low dielectric loss and high breakdown strength.

Graphene is also widely investigated as a filler in polymer nanocomposites.[104-106] The huge surface area of graphene nano-sheets can generate high permittivity by forming a number of nano-capacitors in the matrix. But the reasonable combination between the dielectric permittivity, dielectric loss, and the breakdown strength has a long way to go.

Recently more-effective core-shell approaches have been implemented; however, they often have low yield and require high cost. [52, 102, 107]

2.2.5 Applications of High-*k* PMCs

Polymer matrix dielectric composites with high permittivity (high-*k*), light weight, good processability and flexibility deserve special attention because of their many potential applications including energy storage devices,[82] embedded capacitors,[108] electromechanical transducers,[109] gate dielectrics[110] and electroactive materials.[111]

There is growing need for electrical energy storage in mobile devices, stationary power systems, hybrid electric vehicles and pulse power applications. Especially, the electrostatic energy storage that can deliver a large amount of stored energy almost instantaneously is gaining special attention. Electrostatic capacitors are the only type of storage capable of delivering an extremely high power density (on the order of MW).[51] This kind of "pulse power" energy storage can be used in many military and commercial applications.[5] However, the commercially available electrostatic capacitor, biaxially oriented polypropylene (BOPP), shows low energy density (~2 J/cm^3) due to its low relative permittivity, which is far behind for the reliable, compact, and efficient electric power system.[51, 112] High-*k* polymer matrix composites with high dielectric permittivity, low loss, high energy density and processability can be used in these applications if reliable high-*k* PMCs can be cost effectively fabricated on a large scale.

2.2.6 Background on Materials to be Made Into Dielectric Composites in this Dissertation

2.2.6.1 Barium Titanate (BT)

Barium titanate (BT) is one of the most widely investigated oxides. BT is a crystalline material, which crystallizes with the perovskite structure. Figure 2.19 shows a perovskite structure that has the general composition of ABO_3. BT shows a paraelectric cubic phase in which the center of negative and positive ions coincides as shown in the cubic form obtained in Fig. 2.19 above the ferroelectric Curie temperature (130 ℃). Thus the net dipole moment is negligible. When the temperature is in the range of 0 ℃ to 130 ℃, the ferroelectric tetragonal phase is stable as depicted in Fig. 2.19 (right). A structural change where the centers of Ba^{2+} and Ti^{4+} cation are displaced relatively to the O^{2-} ions, leads to the formation of electric dipoles. This distorted structure gives spontaneous polarization. Each unit cell of the BT crystal processes a reversible dipole moment that is spontaneously aligned parallel to the direction of dipole moments of adjacent unit cells, resulting in a net dipole moment.

There have been many efforts to study the effects of substitutions for A- and B-site. For instance, A- site can be substituted by Sr^{2+} and Pb^{2+}, resulting in changes in the Curie temperature. The substitution of both A- and B- sites with different cations has been used to adjust properties of BT.[113, 114] Conventional ferroelectric materials such as barium titanate (BT), lead zirconate titanate (PZT), lead manganese niobate (PMN), and potassium niobate (KNO) can be made into thin films by using chemical solution deposition and high temperature processing, resulting in a high real permittivity up to a few thousands and a relatively low dielectric loss. However, the high temperature processing is not suitable with many substrates, especially polymeric flexible substrates.[115] The polymer matrix composites containing ferroelectric nanoparticles have been extensively studied for the past decade to overcome this problem.

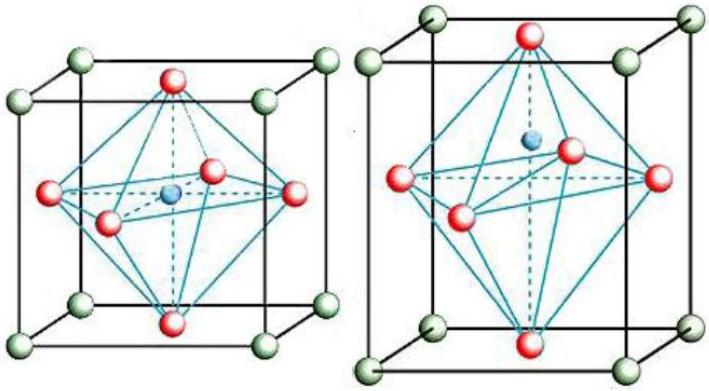

Figure 2.19. The structure of (left) cubic and (right) tetragonal $BaTiO_3$. The red spheres represent oxygen centers, blue Ti^{4+} cations, and green Ba^{2+}, respectively. The off-center position of Ti^{4+} ions are shown in tetragonal structure. (copyright Army High Performance Computing Research Center (AHPCRC), Stanford University)

2.2.6.2 Poly(vinylidene fluoride) (PVDF)

PVDF is a highly non-reactive and pure thermoplastic fluoropolymer, which is widely investigated due to its pyroelectric and piezoelectric properties. The glass transition temperature (T_g) of PVDF is about −35 °C and it is a semi-crystalline polymer. PVDF exists in several forms: α (TGTG'), β(TTTT), and γ (TTTGTTTG'), δ and ε phases, depending on the chain conformations as trans (T) or gauche (G) linkages. The α and β phases are the most general and important ones. In the α phase, the chains with a TGTG' conformation, are packed in an antiparallel fashion, thus the net dipole moment is negligible.[116] The β phase, which is all trans (TTTT) conformation, has an orthorhombic unit cell where the chains are parallel. The β phase is usually obtained by stretching and poling the α phase.[117-119] The molecular dipoles in the β phase are aligned in the same direction normal to the chain axis, generating a strong net dipole moment. Figure 2.20 shows the structures of PVDF non-ferroelectric α and ferroelectric β phases.[120]

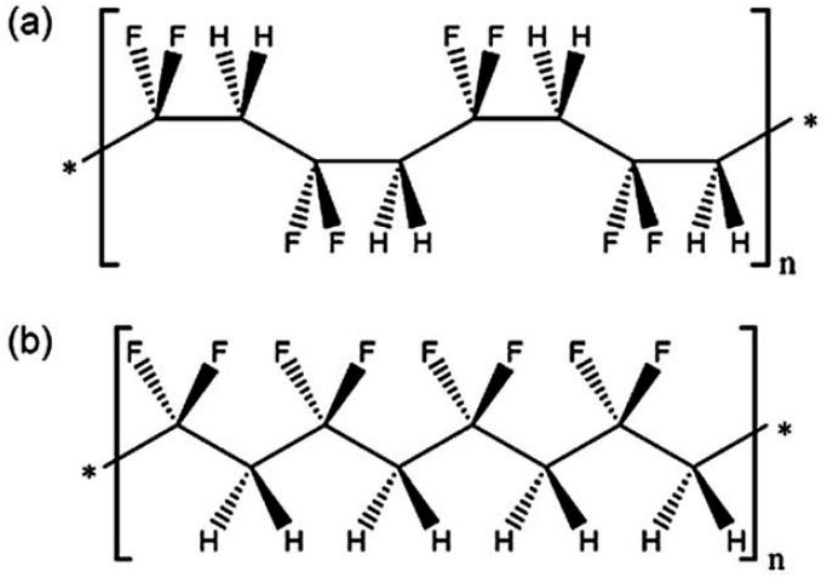

Figure 2.20. Structures of (a) non-ferroelectric α phase and (b) ferroelectric β phase PVDF.[120]

2.3 Simulation and Characterization Tools

2.3.1 COMSOL Multiphysics®

Finite element analysis (FEA) is a numerical method useful for solving problems with complicated geometries, loadings, and materials properties where analytical solutions cannot be obtained.[121] FEA has been widely used to analyze structural engineering mechanics such as deformation and stresses in solid bodies, dynamics of structures and heat flow.[121]

In recent years, FEA has been extended to nanoscale electrical characterization of materials. For example, the roles played by geometric parameters of thin films and electrodes have been studied.[122, 123] In these works, the numerical simulation of the impedance of thin films was carried out and the related quantities such as capacitance and resistance were deduced. However, to the best of our knowledge, FEA has not yet been widely employed in the study of the electrical properties of composites. In the literature, the vast majority of impedance related work is experimental in nature, and simulation

studies are very limited. However, several approaches for impedance simulations have been reported.[124-126] For example, Chen et al. used the finite element method to simulate the effects of mixed ionic electronic conductors (MIECs) thin film electrodes in solid oxide fuel cell.[125]

FEA can be used in both conductive and dielectric PMCs if a realistic modeling geometry, which illustrates the microstructures of the PMCs, is available. COMSOL Multiphysics® (Comsol Inc., Burlington, MA) is a commercial FEA tool which was used in this thesis. It provides all of the necessary factors for a complete model by coupling related physical applications, making it a comprehensive, user-friendly simulation software environment for a wide range of applications. The impedance response of composite materials can be simulated using a time harmonic-electric current solver in the AC/DC module of COMSOL Multiphysics®, which implements a finite element method to solve partial differential equations. The objective is to solve Maxwell's equations for the time harmonic electric potential phasor in 2D or 3D geometry, which contains matrix and filler materials and their microstructures. The real and imaginary components of the impedance (Z) can be calculated using built-in functions in COMSOL Multiphysics®. When voltage is applied to the port electrode, the current that flows through it is extracted. The total current flowing from the port electrode to the ground electrode is calculated by integrating the current density. The complex impedance can be calculated from the electric potential distribution. Then other dielectric functions such as admittance (Y), electric modulus (M), permittivity (ε) can be calculated using the following relationships:

$$Z^* = \frac{1}{Y^*} = Z' - jZ'' \tag{2.15}$$

$$Y^* = Y' + jY'' \tag{2.16}$$

$$Y^* = j\omega C^* = j\omega C_g \varepsilon^* \tag{2.17}$$

$$\varepsilon^* = \frac{1}{M^*} = \varepsilon' - j\varepsilon'' \tag{2.18}$$

$$M^* = M' + jM'' \tag{2.19}$$

where the term j *is* $\sqrt{-1}$ and C_g is geometric capacitance.

2.3.2 Impedance Spectroscopy

The electrical properties of a material system result from multiple microstructural processes such as the movement, concentration, and hopping of charge carriers like electrons and ions. These properties can change if additional features are present in the material, such as defects and interfaces.[127] Composite materials which contain matrix and filler materials may have more than one current path. It is very useful to characterize the matrix-filler interfaces and the percolated networks in composite materials.[127] When measuring with a direct current (DC), it is assumed that the system is time-invariant and that the electrical measurement is at a steady state.[35, 128] As a result, many of these microstructural processes that contribute to the overall properties are lost in the DC measurement. However, impedance spectroscopy (IS) is an alternating current (AC) technique, which is able to show the influence of these processes.[127] Impedance spectroscopy involves the measurement of the current (I), voltage (V), and the phase angle (θ) between the current and voltage over a wide range of frequencies so that the impedance vector (Z^*) may be defined as follows:

$$Z^*(\omega) = V(\omega)/I(\omega) \tag{2.20}$$

where $V(\omega) = V_m sin(\omega t)$, $I(\omega) = I_m sin(\omega t + \theta)$ and $\omega = 2\pi f$. The relationship between the complex impedance and the phase angle is defined as follows:

$$|Z| = [(Z')^2 + (Z'')^2]^{1/2} \tag{2.21}$$

$$\theta = tan^{-1}\left(Z''/_{Z'}\right) \tag{2.22}$$

$$Z' = |Z|cos\theta \tag{2.23}$$

$$Z'' = |Z|sin\theta \tag{2.24}$$

where Z' is the real part of the impedance and represents the energy that passes through the material, Z'' is the imaginary part of the impedance and represents the energy lost or stored in the material and $|Z|$ is the impedance magnitude.[129]

The real and imaginary components of the impedance are often plotted with the real component along the x-scale and the imaginary component on the y-scale. The convention with the imaginary component is to have the negative values along the y-axis in the first quadrant. These types of plots are known as either complex plane plots or frequency independent/implicit plots. While the frequency is not shown explicitly for a semicircle in the impedance complex plane, the frequency increases from right to left.[127]

Figure 2.21 shows some examples of complex impedance plots (Figs. 2.21 (a-d)).[35, 127] The DC resistance can be obtained from the intercept onto the real impedance axis on the complex impedance plot. The capacitance can be extracted from the complex impedance plot in Fig. 2.21 (a) by using the impedance and frequency at the apex of the semicircle.[35, 127] A similar method can be used to calculate the inductance in Fig. 2.21 (b).[35, 127] Semicircles in the complex impedance plots are indicative of behavior represented by equivalent circuit elements in parallel (Figs. 2.21 (a-b)).[35, 127] On the other hand, if the complex impedance is linear, such as Figs. 2.21 (c-d) there are elements in series.[35, 127] The impedance plots as a function of frequency, known as Bode plots, can show the onset of a relaxation process as an increase or decrease in the real part of the component, or as a peak in the imaginary part.[127, 129] Figures 2.21 (e) shows the Bode plot of the phase angle.[35, 127] This plot can show the explicit behavior of a capacitor, a resistor or an inductor, where the phase angles of -90°, 0°, 90° are purely capacitive, purely resistive or purely inductive behaviors respectively.[35, 127]

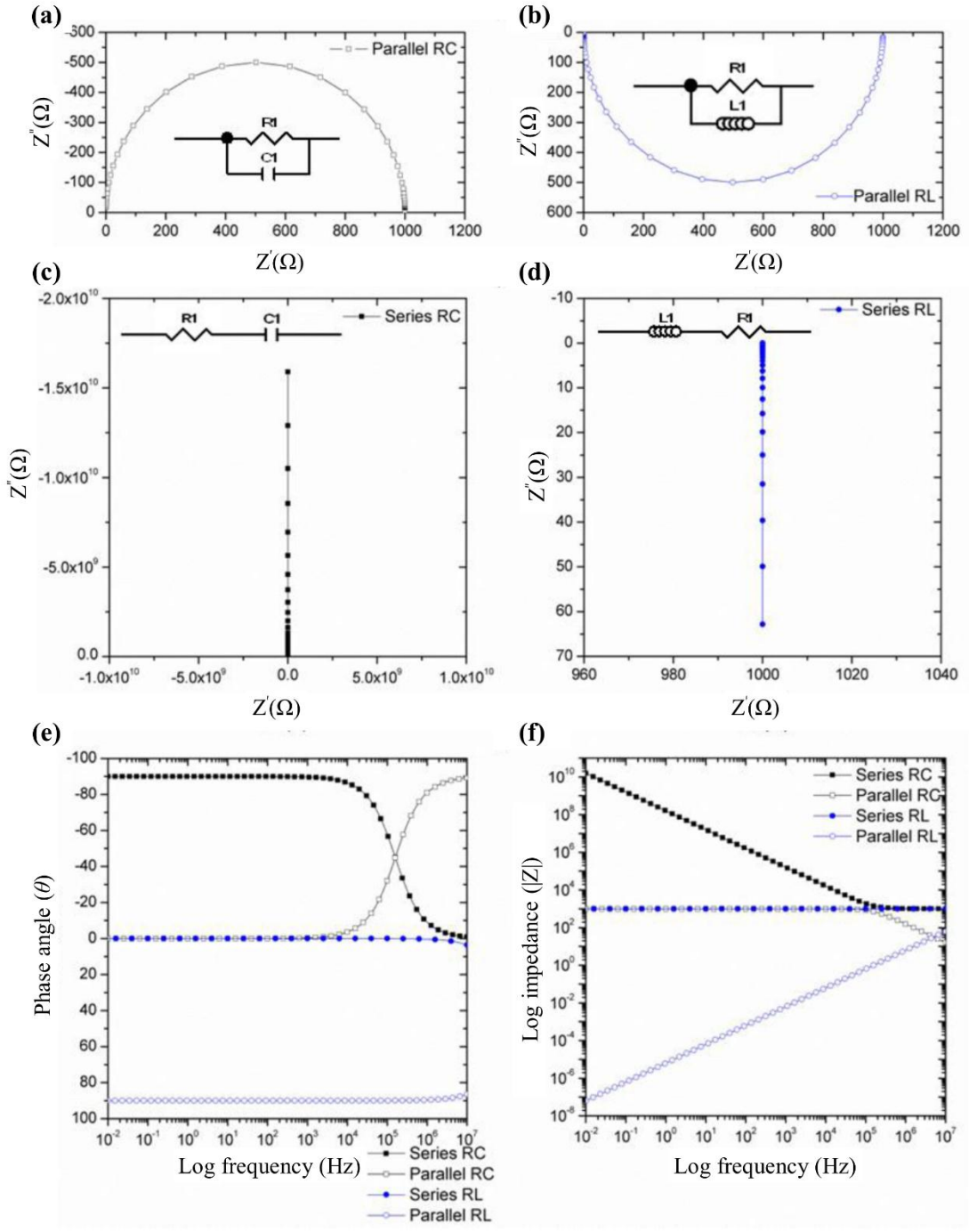

Figure 2.21. (a) Complex impedance plot for a resistor (1000 Ω) and a capacitor (1 nF) in parallel. (b) Complex impedance plot for a resistor (1000 Ω) and an inductor (1 μH) in parallel. (c) Complex impedance plot for a resistor (1000 Ω) and a capacitor (1 nF) in series.(d) Complex impedance plot for a resistor (1000 Ω) and an inductor (1 μH) in series. (e) Phase angle Bode plot of the circuit impedance from (a-d). (f) Impedance magnitude plot of the circuits from (a-d).[35, 127]

The data can also be plotted in terms of other dielectric functions such as admittance, Y^*, electric modulus, M^*, and permittivity, ε^*. While it is not uncommon that the electrical analysis is conducted using only impedance plots, it is very important to investigate the responses using all four dielectric functions, because different responses in the materials such as polarization or conduction processes, may not be detectable when using only one formalism.[127, 129]

CHAPTER 3

CONDUCTIVE NANOCOMPOSITES WITH SELF-ASSEMBLED NANOPARTICLES

In this chapter results obtained from polymer matrix composites with phase segregated conductive networks are presented and discussed. The addition of an electrically conducting filler to an insulating material will eventually result in percolation. Forming a segregated conductive network is the most promising strategy to lower the percolation threshold (ρ_c).[4, 30] The conductive fillers are primarily located at the interfaces between matrix-rich regions rather than randomly distributed in the matrix polymer. The particular focus in this chapter is on how to fabricate the composites to lower electrical percolation threshold (ρ_c) for improved electrical conductivity while maintaining semi-transparency. 2D/3D finite element analysis was conducted to improve predictability of the electrical properties in the composites with phase segregated percolation networks.

3.1 Experimental Procedure

3.1.1 Filler and Matrix Components used

Poly(methyl methacrylate) (PMMA) was selected to be used as a matrix in this study because it undergoes glass transition around 105 ℃ and several studies have been previously conducted.[10, 25, 30, 47, 130] It is highly insulating and also transparent. A transparent and conductive composite can be fabricated if the electrical percolation can be achieved at a low concentration of the conductive nanofillers.

Monosize PMMA was obtained from Cospheric LLC. The particle size was in the range of 90 ~ 106 μm (Fig. 3.1 (a)). The polydisperse PMMA was obtained from Buehler Ltd (Transoptic powder). The particle size was in the range of 10 ~ 100 μm (Fig. 3.1 (b)) and the average size was 52.4 ± 4.37 μm with a standard deviation of 27.8μm. The glass

transition temperature of PMMA was 105 ℃ as obtained by differential scanning calorimetry (Fig. 3.3). Antimony tin oxide (ATO), containing 10 wt % Sb_2O_5 to SnO_2, was selected as a conductive nanofiller, because it shows good electrical conductivity, optical transparency and is cheaper than ITO, which is the most widely used transparent conductive metal oxide. ATO was obtained from Alfa Aesar (Ward Hill, MA). According to the manufacturer, the size range was 20 ~ 40 nm. From the TEM micrographs (Fig. 3.1(c)), the average size was found to be close to this value.

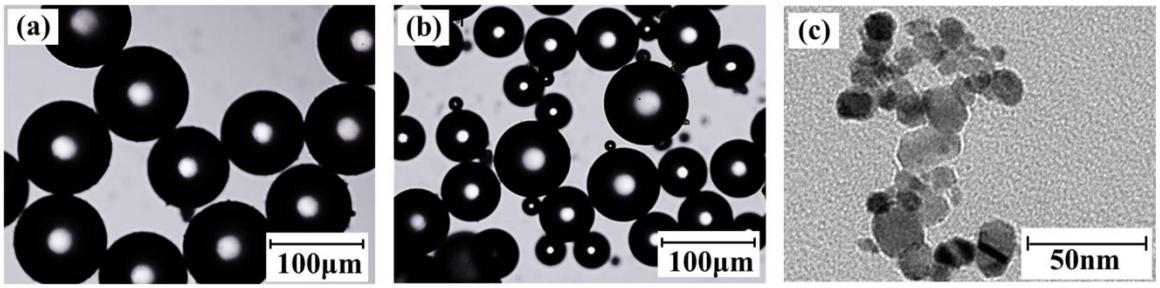

Figure 3.1. Optical images of (a) monosize PMMA, (b) polydisperse PMMA and (c) TEM image of ATO nanoparticles.[6]

3.1.2 Composite Fabrication Procedure

PMMA and ATO particles were mechanically blended for 10 min at room temperature. The surface of the PMMA microspheres was covered with ATO nanoparticles. The nanoparticles on the surface of the matrix were uniformly distributed as blending time increased. However, care must be taken to avoid localized heating in the blender which can partially liquefy some polymer spheres and decrease the connectivity of the filler-chain network during compression molding. The conductive nanoparticles can be surface modified for better interaction with the polymer matrix. However, doing so might prevent good electrical contact between the nanoparticles. Therefore, ATO particles were not surface modified prior to blending. The composition of PMMA/ATO composites was varied between 0.09 vol % ~ 1.75 vol %. The ATO coated PMMA microspheres were compression molded using a Struers mounting press at a temperature

between 150 and 190 ℃ for 15 min. The pressure applied during molding was in the range of 12.67 to 50.68 MPa. The nanocomposites were hot pressed as disks with diameter of 31.7 mm. The sample thicknesses were controlled to be 2.0 mm and 0.6 mm.

3.1.3 Microstructural, Optical, and Electrical Characterization

3.1.3.1 Microscopy and UV-Vis Spectroscopy

For microstructural analysis, a Hitachi S3700 scanning electron microscope (SEM) (Dallas, TX) was used. Selected samples were polished with silicon carbide paper and alumina polishing solution. Samples were imaged on both the as-polished surfaces and the as-polished cross-sections. Additionally, some samples were fractured at room temperature to expose fractured cross-sections without polishing disruption. As a word of caution, it is important to post-process the composite samples below their glass transition temperature to avoid polymer flow and deformation.[10] All specimens were scanned using a backscattered detector at 15 kV accelerating voltage and 40 to 50 Pa. The variable pressure mode enabled the acquisition of SEM images without metal coating.

Optical transmittance of the composites was measured using an Agilent technology Cary 60 UV-Vis spectrophotometer at a scan speed of 1200 nm/min between 390 nm and 700 nm wavelength. Air was taken as the reference. For the optical transmittance measurements, samples with 0.2 mm thickness were compression molded at 170 ℃ and 12.67 MPa.

3.1.3.2 In-situ Electrical Measurements

In order to perform electrical measurements in-situ under pressure and temperature, a special die with an inner diameter of 10 mm was used that involved two stainless steel pins and an insulating alumina sleeve.[35] The steel pins would compress the samples with attached leads to the top and bottom pins so that both AC and DC measurements can be made. Figure 3.2 illustrates a schematic of the in-situ measurements set up. A Keithley model 2000 multimeter was used for DC measurements and an impedance spectroscopy frequency response analyzer (Solartron 1260) together with a 1296 dielectric interface (Solartron 1296) were used for the AC measurements. A closed circuit would be made by the steel pins and the samples, because the alumina sleeve is highly insulating. A Carver dry press was used to apply pressure and OMEGALUX™ flexible heating tape and BriskHeat® benchtop temperature controller were used to control the hot pressing temperature. The electrical response of the ATO powder and the composite samples could be measured as a function of the applied pressure and temperature. An insulating layer was also placed between the steel pins and the plates of the Carver dry press in order to prevent any signal going through the press.

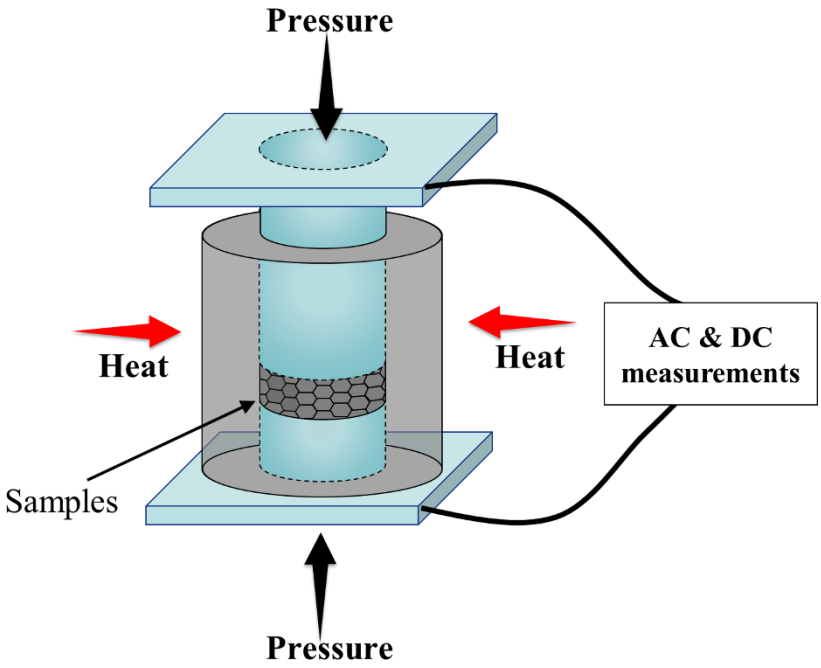

Figure 3.2. Schematic of the in-situ measurements configuration.

3.1.3.3 AC Electrical Measurements

An impedance spectroscopy frequency response analyzer (Solartron 1260) together with a 1296 dielectric interface (Solartron 1296) were used for electrical characterization of the composites. All of the electrical measurements were taken using 0.5 V_{rms} with a frequency range 0.1 Hz to 10 MHz without any DC bias. Prior to impedance measurements, a Denton Vacuum Desk II Turbo Sputter Coater (Denton Vacuum, Moorestown, NJ) was used to apply silver coating to both surfaces as contact electrodes. The complex impedance was obtained from at least 3 samples for each composition or processing condition evaluated. The DC conductivity was obtained by taking the intercept of the imaginary impedance onto the real impedance axis on the complex impedance plot (Z" vs. Z′) then, converted into resistivity value using the dimensions of each sample. The impedance response measured as a function of applied frequency can detect percolation in insulator-conductor nanocomposites.[131]

3.2 Results and Discussion

3.2.1 Properties of the Precursor Materials

3.2.1.1 Thermal Analysis and Electrical Conductivity of Matrix Polymer (PMMA)

Figure 3.3 displays a differential scanning calorimetry (DSC) scan of the PMMA particles taken with a ramp rate of 20 ℃/min. The data shows that the PMMA has a glass-transition temperature around 105 ℃ and a degradation temperature around 255 ℃. Figure 3.4 shows complex impedance plot of a compression molded PMMA pellet. DC resistance was obtained from the intercept of simulated impedance complex curve on the x-axis. DC conductivity of PMMA was 1.09×10^{-13} S/m based on the sample dimensions.

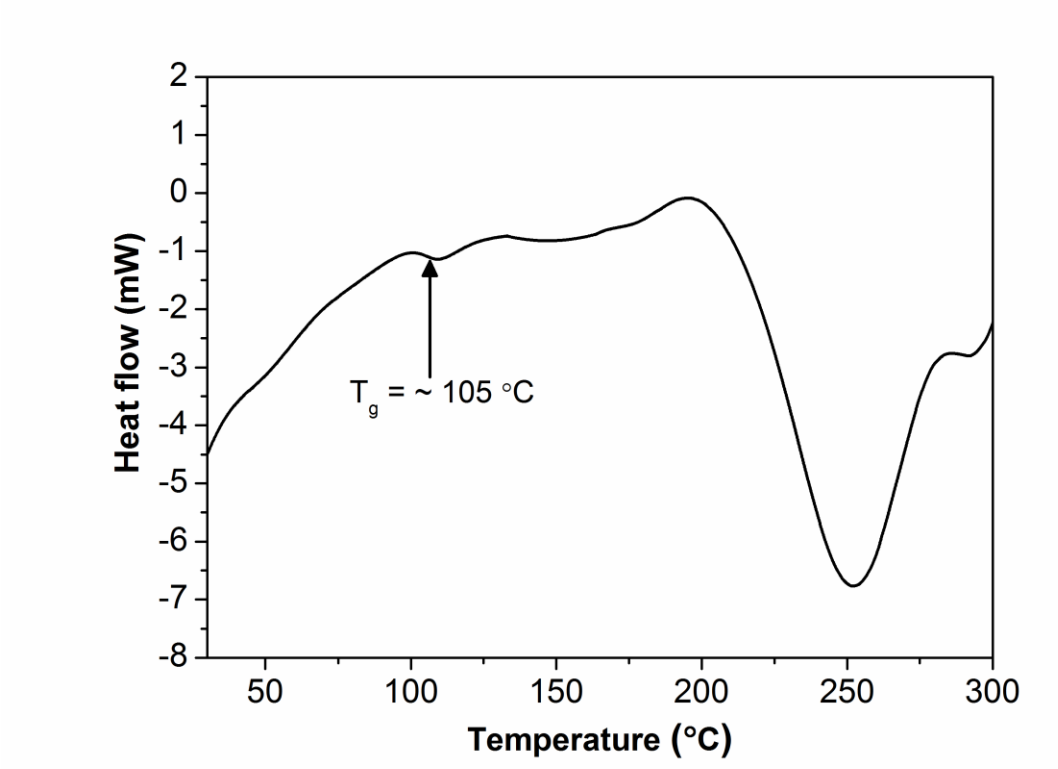

Figure 3.3. Differential scanning calorimetry (DSC) scan of PMMA particles.

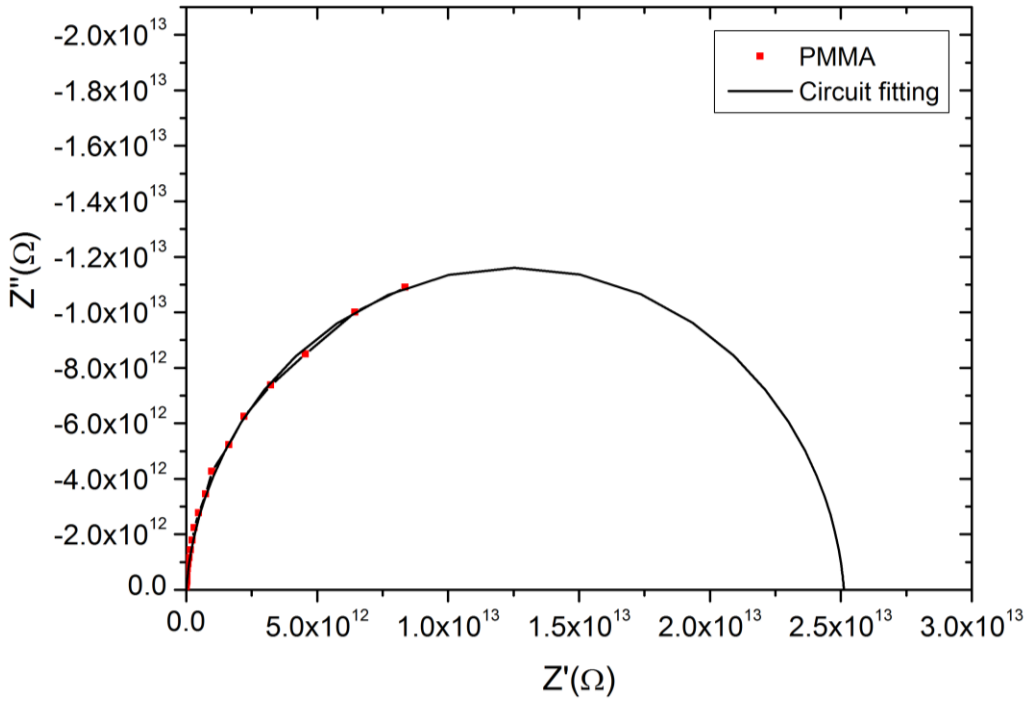

Figure 3.4. Impedance complex plot of compression molded PMMA pellet (diameter: 31.7mm and thickness: 2mm).

3.2.1.2 Electrical Conductivity of Antimony Tin Oxide

Figure 3.5 illustrates the complex impedance plots of the compressed ATO NPs. Since ATO is a highly conductive metal oxide, the complex impedance response is similar to that of metallic materials, which is normally represented by a resistor and an inductor in series (series RL circuit). As the pressure increases, the overall resistance decreases. The change in the resistance is due to the thickness decrease of the compressed powder batch and the change in the physical point contacts between the ATO particles.[132] Considering the final dimensions of the compressed ATO powder pellet and resistance of in-situ pressing electrodes (1.4 Ω), the electrical conductivity of the compressed ATO powder from AC measurements was 12.1 S/m. The electrical conductivity from direct DC measurements was 11.2 S/m.

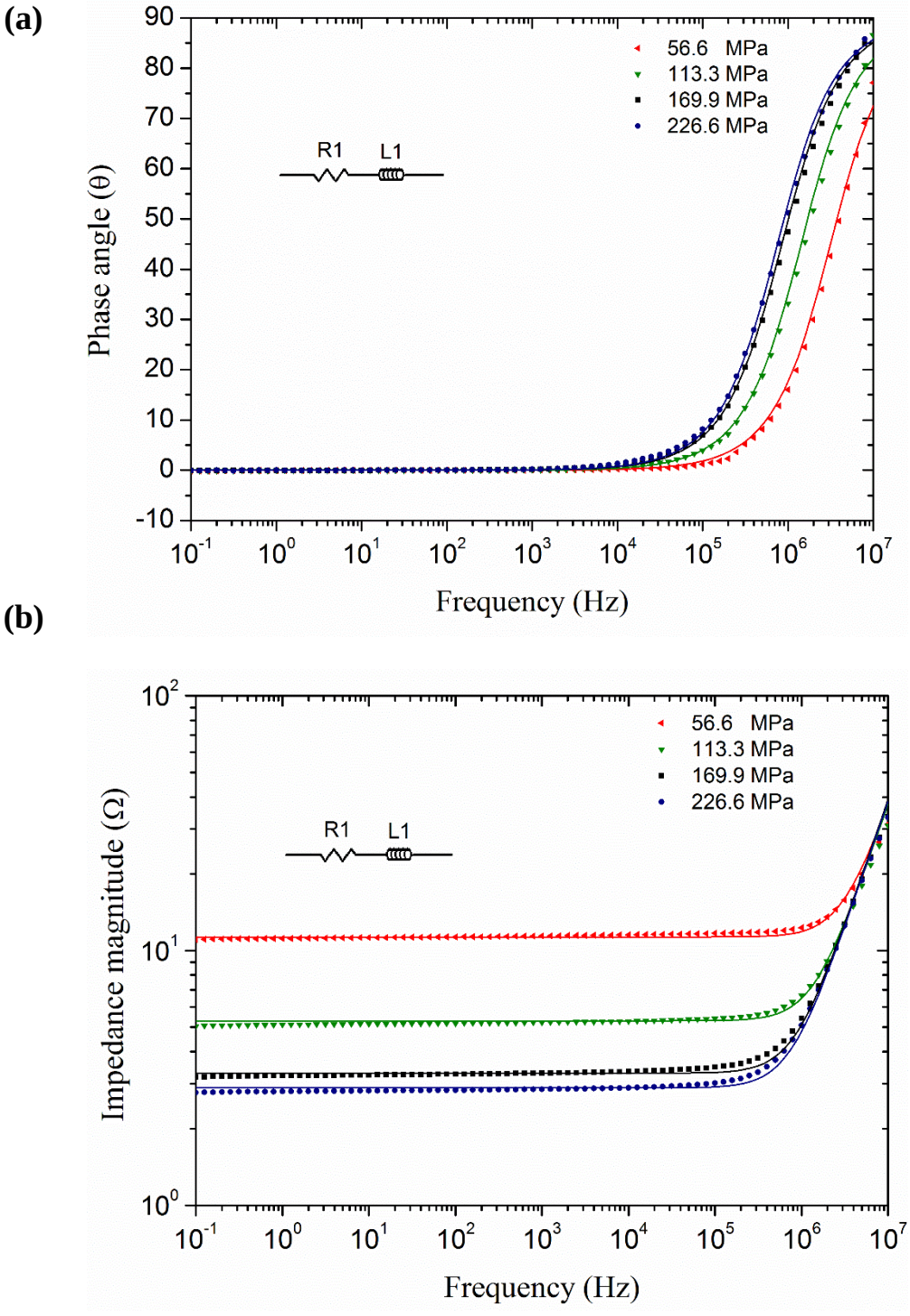

Figure 3.5. (a) Impedance magnitude and (b) impedance phase angle of compressed ATO powder at pressures from 56.6 to 226.6 MPa (Solid lines are fit data; diameter and thickness of pellet at 226.6 MPa are 10 mm and 1.3 mm respectively).

3.2.2 Characterization and Analysis of Results

3.2.2.1 Electrical Conductivity Percolation Curves of Conductive Nanocomposites with Monosize and Polydisperse PMMA

Figure 3.6 (a) and (b) show complex impedance plots for PMMA/ATO composites containing different concentrations of ATO, where the imaginary part of impedance is plotted against the real part of impedance. A semicircle is expected on these plots when a long range conducting process is occurring.[129] The intercepts of the semicircles with the real axes therefore indicate the DC resistance of the composites. For an insulating sample with a low ATO content, the complex plot did not intercept the real axis, which is commonly observed on insulating or dielectric materials.[127] The measured data was fitted using equivalent circuit elements such as a resistance, R, and a CPE (constant phase element) in parallel. The CPE was used to describe the slight deviation from a perfect semicircle in the complex plot as a replacement for a capacitor. A CPE can be expressed by the following equation.

$$Z = 1/[Y_0(i\omega)^{\alpha}] \quad (3.1)$$

where the Y_0 is the constant and α is the CPE power index ($0 \leq \alpha \leq 1$). If α is 1, Y_0 works as a perfect capacitor as in the following equation:

$$Z = 1/[i\omega C] \quad (3.2)$$

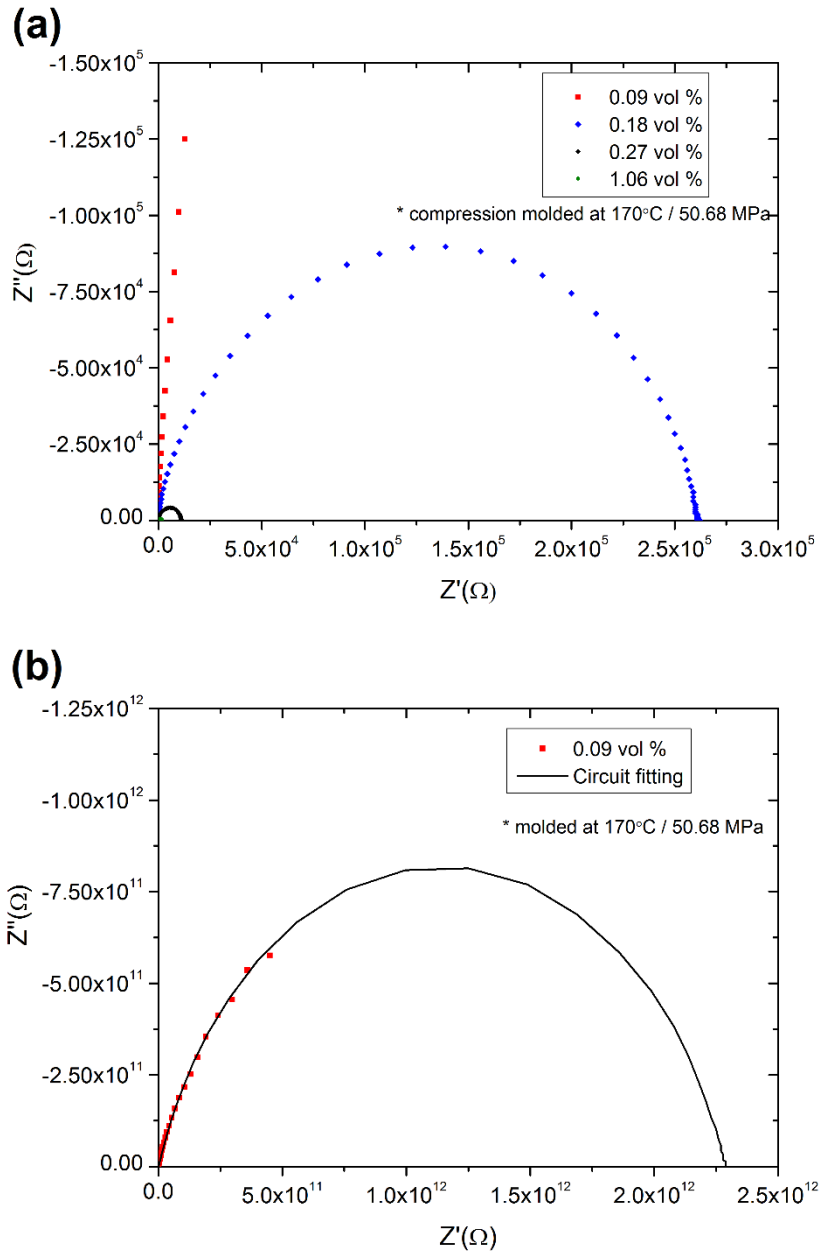

Figure 3.6. (a) Complex impedance plots for several PMMA/ATO composites. (b) Complex impedance plot for the 0.09 vol % PMMA/ATO composite, fitted using a parallel R-CPE model (shown by the solid line).

DC conductivity values were obtained from the intercepts of complex impedance curves onto real impedance axis considering sample geometry, as described above. Figure 3.7 represents DC conductivity as a function of ATO content. Electrical percolation is apparent at 0.27 vol % for the polydisperse PMMA (10 ~ 100 μm) and 0.18

vol % for the monosize PMMA (90 ~ 106 μm) as a matrix, where the electrical conductivity increases by about nine orders of magnitude. The percolation threshold is mostly affected by the size ratio of the matrix and the filler ($\rho_c \propto r_{filler}/r_{matrix}$), where the larger the ratio is, the larger ρ_c is.[7] In this study, it was found that the percolation threshold is lower for the composites made with the monosize starting materials because the size ratio between the matrix and the filler is lower than in the polydisperse samples. These results are consistent with other insulator-conductor composites fabricated by a similar procedure,[19, 25, 30, 132] all of which percolate at much smaller volume fractions than the theoretically estimated and previously reported values.[15] It is certain that the sharp increase in DC conductivity is due to the onset of the first chain of conductive particles.

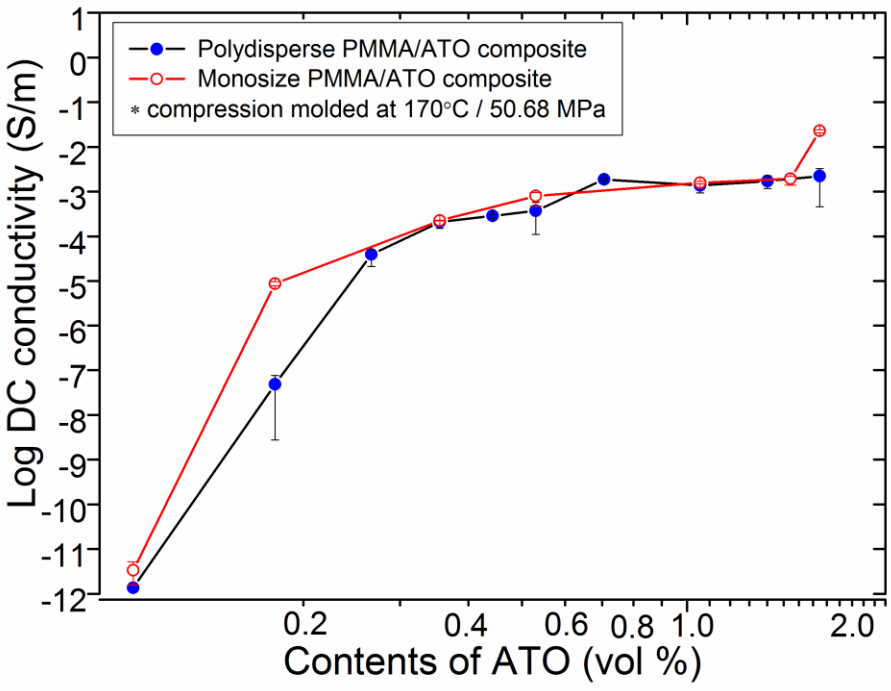

Figure 3.7. DC conductivity of PMMA/ATO nanocomposites as a function of ATO content (molded at 170 ℃, 50.6 MPa for 15 min).[6]

Figure 3.8 shows the AC conductivity as a function of frequency for the two sets of samples measured. These graphs further illustrate the effect of the starting PMMA size distribution where the change from the insulating behavior to the conducting behavior occurs at different ATO contents and the critical frequency at which this occurs shifts to a different value. The composites with the ATO concentration below ρ_c remain frequency dependent throughout the whole frequency range. Insulating materials normally show this frequency dependent behavior, which is characteristic of capacitive behavior.[30] In contrast, the composites with the ATO concentration above ρ_c show frequency independent behavior (i.e. plateau region) at low frequencies, which is characteristic of conducting materials. This reflects the onset of the first continuous chain of nanoparticles. The plateau region becomes wider as the ATO content increases, until only the conducting behavior is observed, as seen for the 1.75 vol % sample in Fig. 3.8 (b). The changes are related to the number of ATO nanoparticle chains that are connected. The frequency dependent to independent transition appear at the critical frequency (f_c), which is also marked on the plots in Fig. 3.8. The electrical conductivity is exponentially proportional to the frequency above the critical frequency according to the power law, $\sigma(\omega) \propto \omega^x$.[30] It can be seen that for samples with composition near the percolation threshold, the critical frequency (f_c) moves to a higher frequency for the homogeneous PMMA composites as compared to the polydisperse materials. It is also notable that the composites made with the monosize materials are able to reach a higher conductivity than those made with the polydisperse materials (e.g. see data for 1.75 vol %). More information regarding the critical frequency as a function of composition has been described elsewhere.[30]

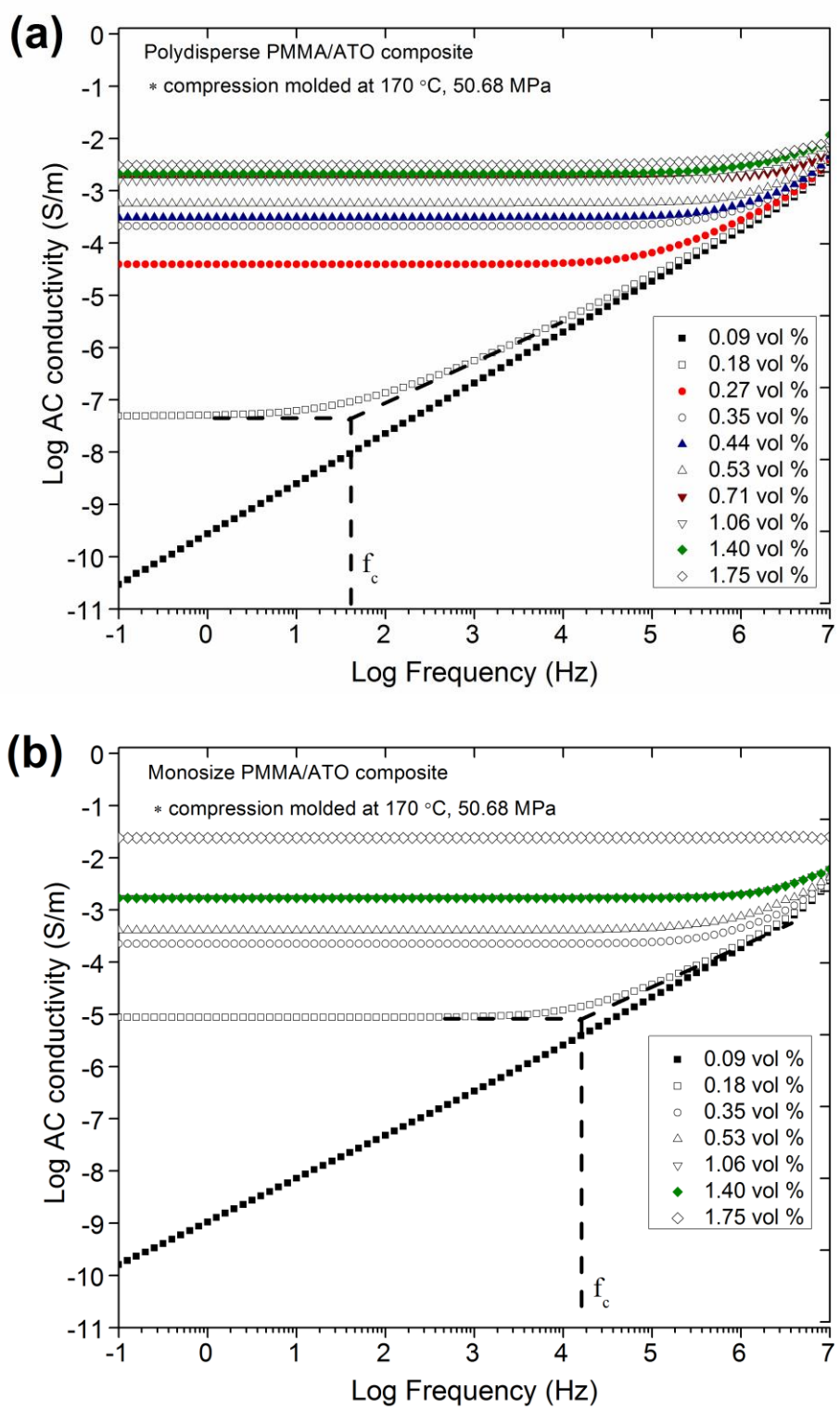

Figure 3.8. AC conductivity of PMMA/ATO nanocomposites for different ATO contents (molded at 170 ℃, 50.6 MPa for 15 min) using (a) monosize PMMA and (b) polydisperse PMMA.[6]

3.2.2.2 Correlation between Microstructure and Electrical Properties

Figure 3.9 (a) ~ (d) display SEM micrographs obtained using a backscattered detector at the accelerating voltage of 15kV in a variable pressure mode SEM (40 Pa). All images were taken on polished surfaces of the specimens. In the microstructure, the polymer matrix appears dark and the ATO nanoparticles appear as the bright regions, as would be expected since the density of ATO is 5 times greater than that of PMMA. The pressure transmitted to the polymer matrix during compression molding results in shape transformation of the matrix micro-spheres into space filling polyhedra, because the ATO NPs, which are coated on the surfaces of PMMA micro-spheres, prevented coalescence of PMMA.[130, 133, 134] During this shape transformation, ATO NPs are forced to be aligned along the edges to form percolation networks, while quite a number of ATO NPs still occupy the interfaces. As the filler concentration increases above ρ_c, ATO NPs are more packed along the edges and a considerable ATO NPs remain on the interfaces. Figure 3.9 (a) and (c) show the polydisperse PMMA composites with the composition 0.09 vol % and 1.06 vol %, whereas Fig. 3.9 (b) and (d) show composites made with the monosize PMMA containing the same amounts of ATO respectively. It is clear that the monosize materials give a more ordered structure, which in turn allow for better properties.

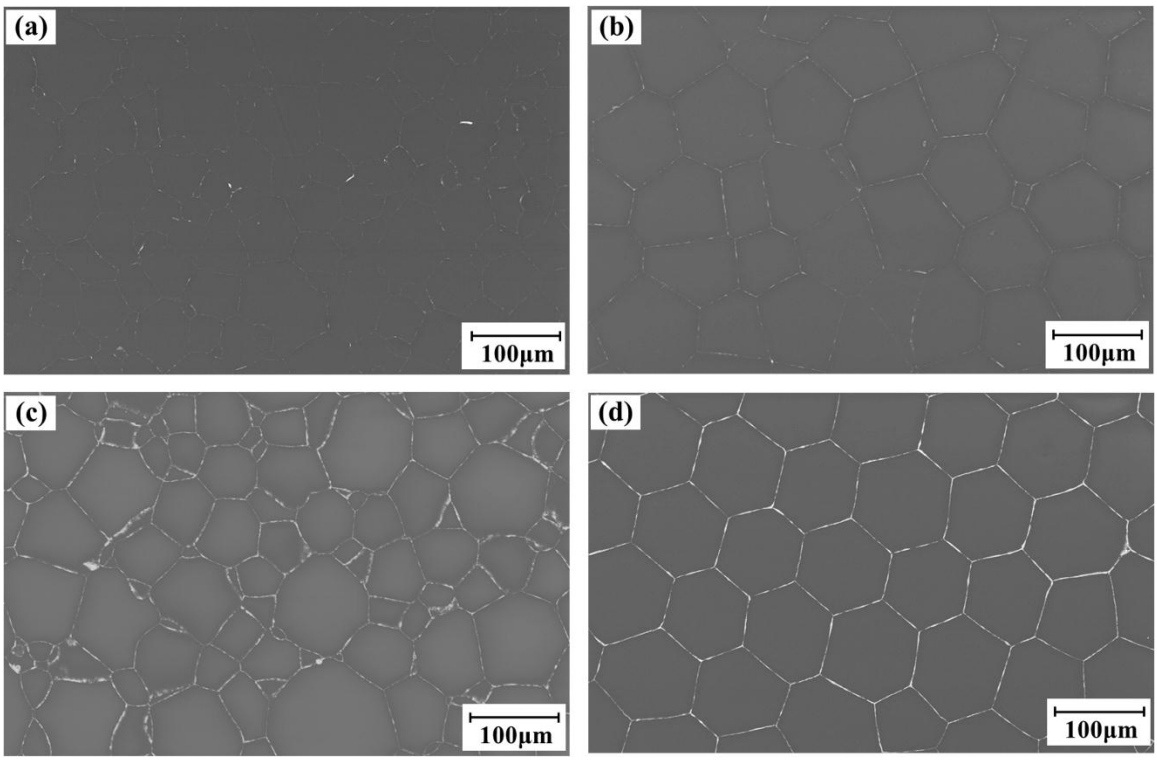

Figure 3.9. SEM images of polished surfaces of PMMA/ATO nanocomposites containing 0.09 and 1.06 vol % ATO for the polydisperse PMMA (shown in panels a and c) and the monosize PMMA (shown in panels b and d), respectively.[6]

The electrical conductivity, shown in Fig. 3.8, increased by several orders of magnitude, when the first continuous chain of conductive nanoparticles was achieved. In the composites with a low filler content of 0.09 vol % (Fig. 3.9 (a) ~ (b)), the boundaries are not clearly detected, because the majority of ATO NPs are packed along the edges. The electrical percolation is not achieved yet, because the filler NPs do not form a direct physical contact through the volume. As the filler content is increased to 1.06 vol %, the electric percolation is achieved and the boundaries become more detectable, because more excess ATO NPs occupy the interfaces. (Fig. 3.9 (c) ~ (d)).

Energy dispersive spectroscopy (EDS) was used to confirm the location of ATO NPs. Two different locations (the center and the edge of matrix) in the composite were scanned, as shown in Fig. 3.10 and labeled ① and ②. The EDS spectra (shown in Fig. 3.10 (b)) showed strong peaks of Sb and Sn in the edge scans (region labeled ①), while

no Sb or Sn peak was detected in the center of a polymer grain (labeled region ②). The presence of ATO NPs coated on the surfaces of PMMA micro-spheres prohibits the polymer coalescence, which in turn produces this microstructure.[25, 130] The ATO NPs are preferably compressed along the edges of matrix lattice to form the percolation networks and excess ATO NPs occupy the interfaces. This is consistent with previous reports published by Gerhardt's group on other composites systems.[7, 15, 19, 25, 26, 30, 130]

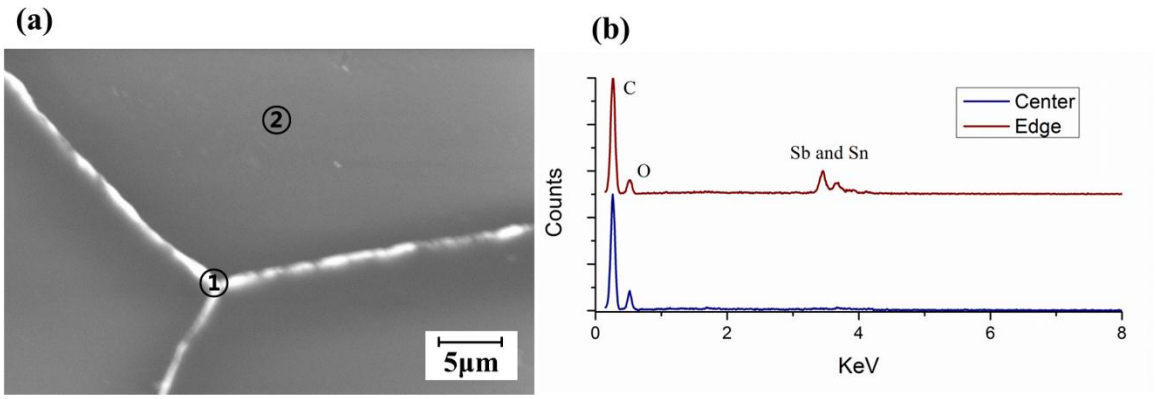

Figure 3.10. (a) SEM image of nanocomposite (1.06 vol %). (b) EDS spectra at different locations : ① edge ② center.[6]

3.2.2.3 Effects of Processing Parameters on the Electrical Conductivity of Phase Segregated Nanocomposites

Figure 3.11 (a) shows the AC conductivity as a function of frequency for the composites with 2 mm thickness containing different ATO concentrations that were fabricated at the same temperature (170 ℃) and different pressures (12.67 and 50.68 MPa). These conductivity curves mirror the formation of the conductive filler network, where the change from the insulating to the conducting behavior occurs at different ATO contents as has been discussed above. The AC conductivity was higher when the higher compression molding pressure (50.68 MPa) was used at low content of ATO (0.18 vol %). However, the difference of the AC conductivity between the samples fabricated using different molding pressures became smaller as the filler content increased. Figure.

3.11 (b) displays the AC conductivity for 1.06 vol % ATO specimens with 2 mm thickness made at different molding temperatures (150, 170 and 190 ℃) and constant pressure (12.67 MPa). At this composition, the behavior is well above the percolation threshold and shows little to no frequency dependence as would be expected. The AC conductivity of the composites containing the same ATO content showed molding temperature dependence. As the molding temperature increased from 150 ℃ to 190 ℃ the AC conductivity decreased from 3.52×10^{-3} S/m to 1.33×10^{-3} S/m. It is obvious that the processing temperature and pressure influence the AC conductivity of the composites.

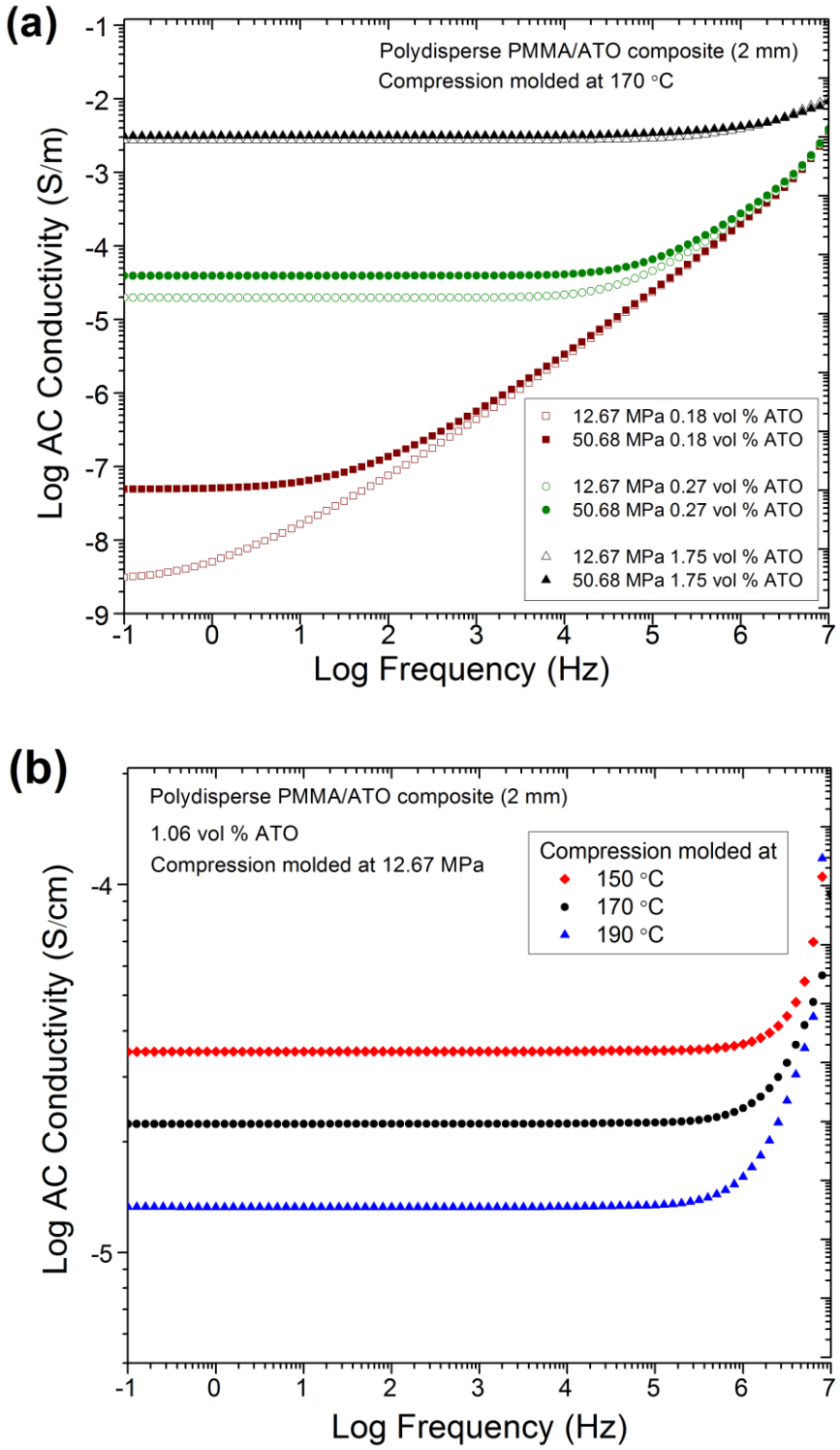

Figure 3.11. AC conductivity as a function of frequency for PMMA/ATO composites containing different (a) ATO contents as well as molding pressures and (b) molding temperatures for 2 mm pellets at constant 12.67 MPa.

Figure 3.12 (a) shows pressure dependence of DC conductivity of PMMA/1.06 vol % ATO composites with different thicknesses. DC conductivity of the thick composite (2 mm) slightly increases, as the compression molding pressure increases. This is due to better physical contacts between the ATO particles. However, DC conductivity of the thin composite (0.6 mm) decreases as the pressure increases. In the case of the thin composite (0.6 mm), the actual transmitted pressure has exceeded the critical value above which the ATO NPs can penetrate the faceted interfaces of the matrix polymer as observed before.[10] Figure 3.12 (b) describes the combined effects of molding pressure and temperature on the electrical conductivity of composites with ATO content above ρ_c. Electrical conductivity increased with pressure when the sample thickness was 2 mm. As the molding pressure increased, nanoparticles were aligned and compressed more by the matrix and the current path had higher filler packing density with respect to the generalized percolation model.[6]

The pressure transmitted to each filler particle can be expressed as

$$P_x/P = exp[-4uzH / D] \tag{3.3}$$

where P_x is the transmitted pressure at any position x below the molding die, P is the molding pressure, u is the coefficient of friction between the powder and the die wall, z is a proportionality factor that represents the ratio of radial stress and axial stress, and H and D are the height of the powder and diameter of the punch respectively.[135] The height of the powder bed is proportional to the amount of powder used to form the composites. Therefore, the transmitted pressure during compression molding, increases as the thickness of the powder bed decreases. As shown in Fig. 3.12, the DC conductivity slightly increased as the applied pressure was increased at all temperatures when the sample thickness was 2 mm. In contrast, when the thickness was 0.6 mm, the DC conductivity decreased as the temperature and pressure were increased simultaneously.

These results illustrate the importance of maintaining the applied pressure below the critical pressure needed to cause penetration of the ATO NPs into the faceted interfaces of the polymer matrix at a given temperature. The critical pressure should be related to the viscosity and shear modulus of the matrix polymer at the molding temperature as well as the size, shape and density of filler nanoparticles. Thus, for samples that were 2 mm in thickness, the critical pressure value was not exceeded, while for the samples that were 0.6 mm in thickness, the critical value was exceeded.
DC conductivity also decreased as the molding temperature was increased. This means that more ATO NPs penetrated the matrix as the temperature increased because the matrix became softer. The minimum temperature to fabricate the conductive nanocomposite with phase segregated conducting network was 150 ℃, and the maximum temperature should be less than the degradation temperature of PMMA (~255 ℃). This is consistent with the previously reported results by Gerhardt group that the molding temperature for the mechanically blended composite batch has to be at least 40 degrees higher than glass transition temperature of the amorphous polymer.[136] The electrical conductivity was the highest when the composites were made at 150 ℃ and 50.68 MPa. However, the processability and flexibility of the composite can be improved by using a higher processing temperature.

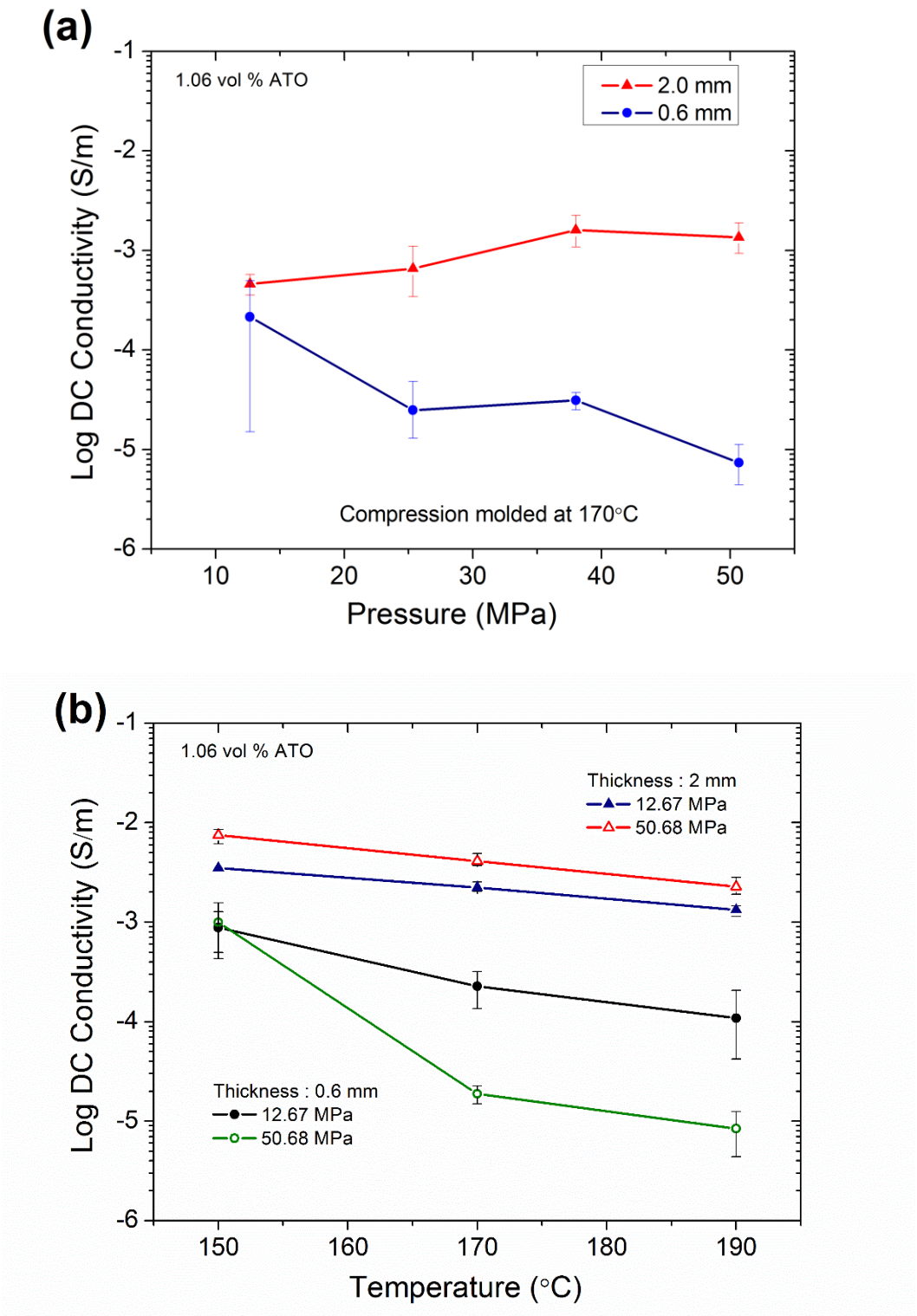

Figure 3.12. DC conductivity of PMMA/1.06 vol % ATO nanocomposite as a function of (a) molding pressure and (b) molding temperature as well as sample thickness.

Figure 3.13 (a) shows in-situ electrical resistance during heating with continuous pressure (50.68 MPa). At an ATO content of 0.27 vol %, the DC resistance decreased by several orders of magnitude as the temperature was increased up to glass transition temperature of PMMA (~105 ℃) (dash line illustrates extrapolated values, because the DC resistance was out of the measurement limit of the multimeter used). It is evident that the ATO NPs on the PMMA surfaces were realigned and forming percolation networks as the PMMA micro-spheres transformed into space filling polyhedra. At an ATO content of 1.06 vol %, the DC resistance gradually decreased with temperature up to 105 ℃. The initial DC resistance of the pressed powder mixture was already low, because the PMMA micro-spheres were coated with interconnected conductive ATO NPs. As the temperature was increased further, DC resistance increased sharply, unlike the sample containing 0.27 vol % of ATO NPs. It is believed that the excess ATO NPs penetrated into the matrix polyhedra and partially destroyed the microstructure.[10] Figure 3.13 (b) shows in-situ DC resistance of composite containing 1.06 vol % of ATO during compression molding procedure (heating-holding-cooling; pressure applied at 170 ℃). As the temperature was increased towards the glass transition temperature (T_g), the DC resistance decreased with temperature, because ATO NPs had better contacts as PMMA microspheres started to deform. Near T_g, the DC resistance remained almost the same, because the matrix and the filler were not compacted yet. At temperatures above 140 ℃, the DC resistance increased sharply with temperature, illustrating that the matrix was subject to hydrodynamic movements. To prove this point, a pressure (50.68 MPa) was applied at 170 ℃, and this temperature was maintained constant for 10 min. The DC resistance suddenly decreased, because the matrix deformed into space filling polyhedra and the ATO particles were pressed along the edges of the matrix polyhedra. As temperature cooled down, the DC resistance underwent a small increase near T_g. It has been reported that the viscosity of PMMA abruptly changes with temperature near T_g.[49] Although the origin of this low peak near T_g is unclear, it is believed that the highly

temperature dependent viscous behavior of PMMA near T_g resulted in slight changes in the DC resistance during cooling toward T_g. As temperature goes down below T_g, DC resistance gradually decreased, because ATO NPs were compressed further by the rigid matrix polyhedra. Due to the sensitivity of the electrical measurements, the in-situ electrical measurements can detect the viscosity changes near and below the glass transition temperature (T_g) but that traditional viscosity measurements done in shear deformation will not, although the study of viscosity below T_g is of great interest since the true glassy state is realized there.[49]

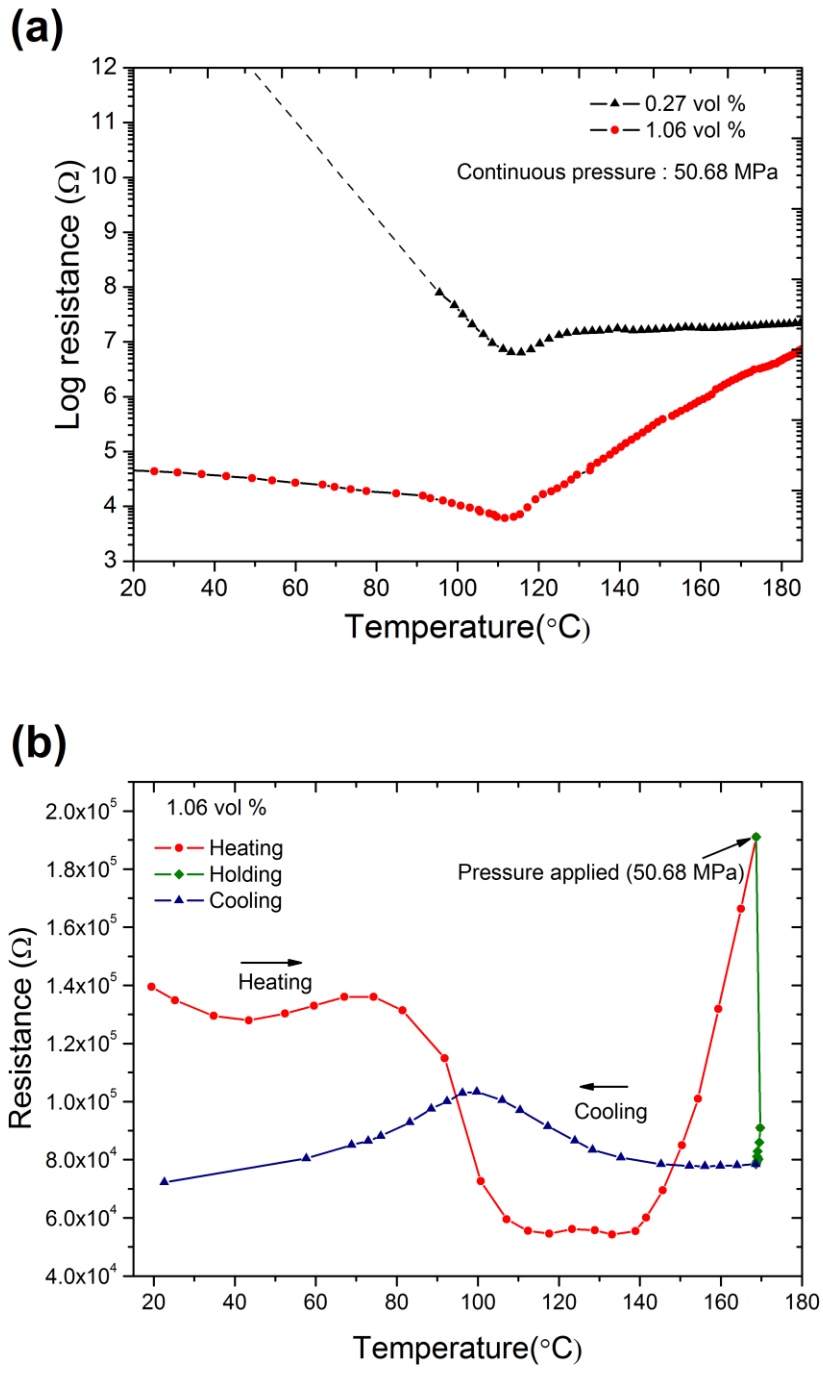

Figure 3.13. In-situ DC resistance during (a) heating with continuous pressure and (b) compression molding of composites.

Figure 3.14 displays the fractured cross sections for the percolated PMMA/ATO composites (thickness: 0.6 mm) containing 1.06 vol % ATO. The fractured cross section of the composites compression molded at 150 ℃ (Fig. 3.14 (a)) shows inter-granular fracture and a large amount of ATO NPs on the faceted surfaces. This occurred because the filler nanoparticles were preferably stacked on the edges and the excess particles remained on the boundaries of the matrix polyhedra. However, for nanocomposites compression molded at 190 ℃, the SEM image shows smooth regions with some waviness, which are characteristic features of trans-granular crack propagation in the pure PMMA and are commonly observed in thermoplastic polymers.[137] This illustrates that more ATO penetration took place during compression molding at the higher temperature in these specimens. However, a considerable amount of ATO remaining along the boundaries still prevented a complete coalescence of the matrix polymer and the specimens still had a measurable conductivity albeit a lower one that resulted in a more flexible composite as depicted in the inset of Fig. 3.14 (b).

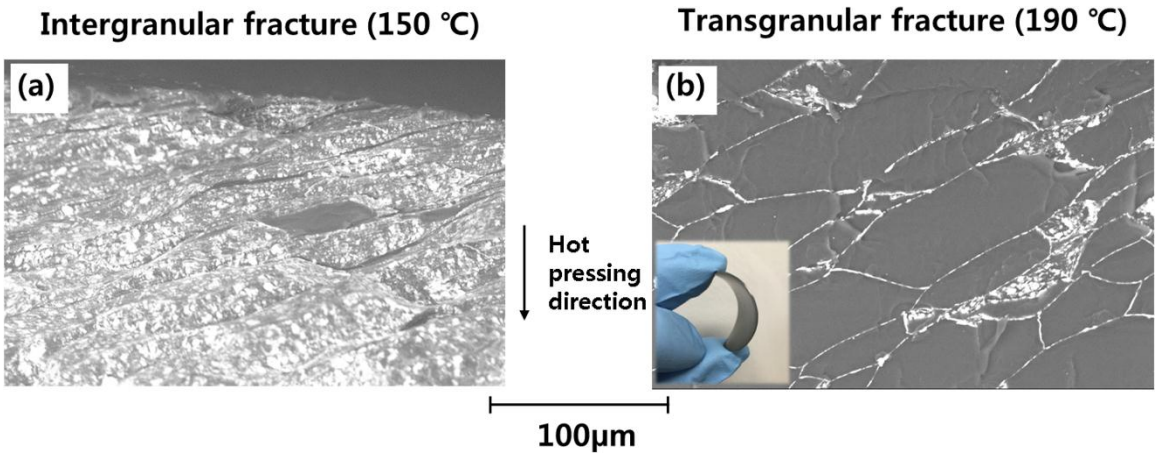

Figure 3.14. Fractured cross sections for PMMA-ATO nanocomposites (thickness: 0.6 mm) containing 1.06 vol % ATO molded at 50.68 MPa and (a) 150 ℃ (b) 190 ℃ (taken perpendicular to the pressing direction).

Figure 3.15 shows schematics to demonstrate the microstructural changes observed with respect to the molding pressure accompanied by SEM images of nanocomposites containing 1.06 vol % ATO made at 190 ℃. The SEM images of the composites molded at 190 ℃ on the polished cross sections (viewed perpendicular to the pressing direction) showed more deformation of the polymer matrix when the higher pressure was used because the nanoparticles destroyed the edges of the faceted matrix (Fig. 3.15 (c) and (e)). But there was no noticeable difference in the SEM images on the polished top surfaces (viewed parallel to the pressing direction) of the composites molded at different pressures (Fig. 3.15 (b) and (d)). The electrical conductivity decreased more than 1 order of magnitude when the molding pressure was increased from 12.57 to 50.68 MPa at 190 ℃ when the thickness was 0.6 mm. This change in electrical conductivity can be explained by the formation of some disconnected current paths and more ATO penetration into the polymer matrix as observed in Fig. 3.15 (e).

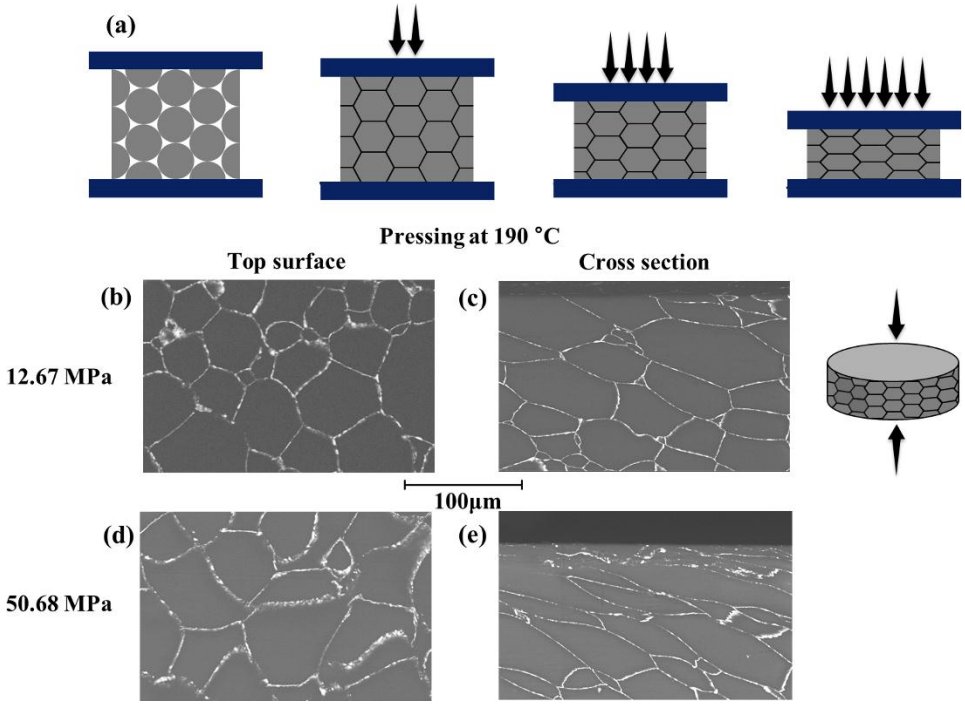

Figure 3.15. (a) Schematics of the microstructure with respect to increasing molding pressure (images modified from reference [18]), (b-e) SEM images on the polished top surfaces and cross sections of PMMA/1.06 vol % ATO nanocomposites (thickness: 0.6 mm) molded at 190 ℃ with 12.67 MPa and 50.68 MPa.

Figure 3.16 illustrates the DC conductivity of the composites (thickness: 2 mm) using the polydisperse PMMA at different ATO contents and molding pressures. DC conductivity values were calculated from the intercepts of complex impedance curves onto real impedance axis adjusting for sample geometry as described earlier in section 3.1.3.3. The percolation threshold (ρ_c) appeared at 0.27 vol % regardless of the molding pressure used, where the electrical conductivity increased by several orders of magnitude. For more accurate ρ_c, however, more data points are necessary at low concentrations of the filler. The DC conductivity slightly increased as the molding pressure was increased, however the pressure dependence of the percolation threshold (ρ_c) was not critical. The DC percolation curves do not fully show the effects of the processing pressure which were clearly shown in the frequency dependent graphs (Fig. 3.11). These results suggest that the transmitted pressure used during molding in the specimens reported in Fig. 3.16 was not exceeding the critical pressure above which the DC conductivity can undergo a sharp decrease as reported by Capozzi et al.[10] because the thickness of the specimens was large enough to prevent penetration of the ATO fillers into the matrix as has been discussed above. The inset in Fig. 3.16 shows a semi-transparent composite with 0.27 vol % ATO and 0.6 mm thickness.

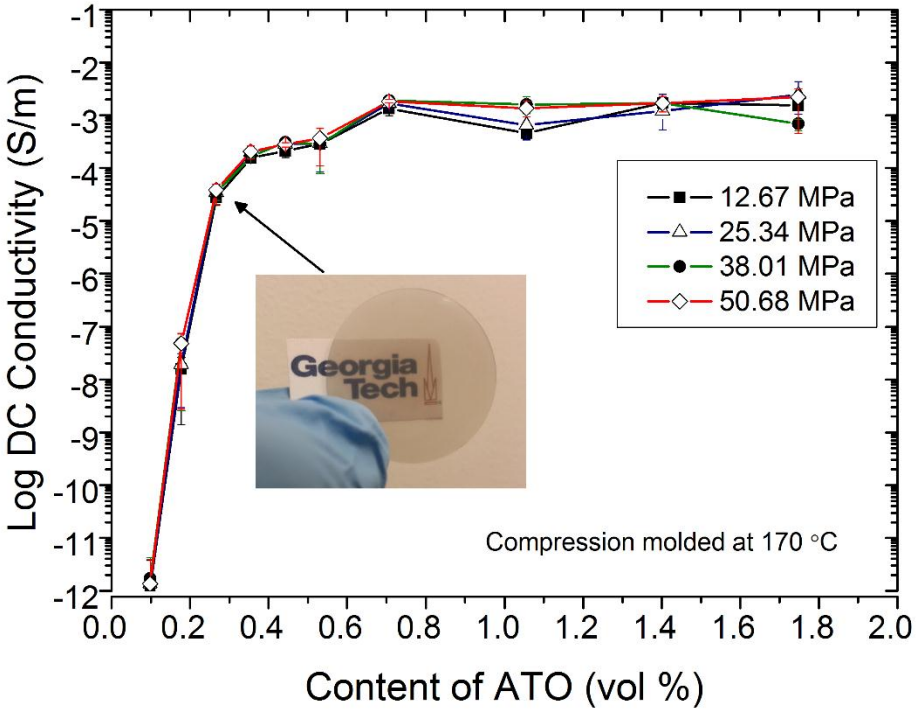

Figure 3.16. DC conductivity of 2 mm thick PMMA/ATO composites as a function of ATO content for samples made at 170 ℃ and different molding pressures.

The conductivity data show correlation with the optical transmittance data which show more gradual reduction in the transmittance as the ATO content increases (Fig. 3.17). A reduction in optical transmittance is common for the phase segregated composites containing transparent materials, due to the significant scattering effects caused by the continuous inter-particle contacts established between the filler particles.[25] Above the percolation threshold, the number of ATO particles in the flat faces of matrix polyhedra substantially increased which resulted in reduced transmittance. The transmittance at 550 nm wavelength of pure PMMA of 0.2 mm thickness was 88.1%, and it decreased to 49.5, 37.5, and 28.0 % transmittance for composites containing 0.18, 0.27 and 0.35 vol % of ATO respectively.

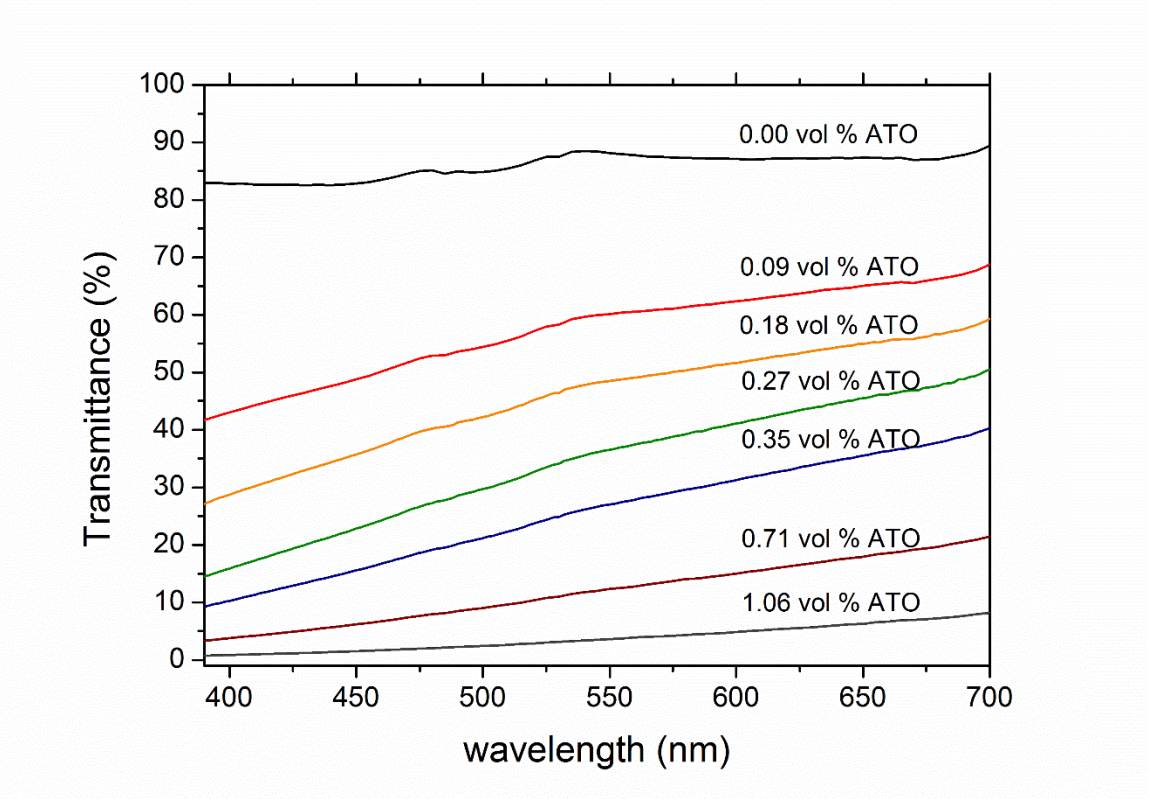

Figure 3.17. Optical transmittance spectra of PMMA/ATO composites made at 170 ℃ and 12.67 MPa (thickness: 0.2 mm) between 390-700 nm (visible light region) as a function of ATO content.

3.2.2.4 Electromagnetic Interference Shielding Effectiveness of Phase Segregated Nanocomposites

Electromagnetic interference (EMI) can be defined as conducted and/or radiated electromagnetic signals emitted by electrical circuits which, under operation, perturb proper operation of surrounding electrical equipments or cause radiative damage to living/biological species.[138] Electromagnetic interference shielding effectiveness (EMI SE) was tested using an Agilent FieldFox Handheld Network Analyzers (Keysight Technologies) in conjunction with a coaxial test cell. The polydisperse PMMA composites containing 1.06 and 1.75 vol % ATO were compression molded at 170 ℃ and 50.68 MPa with 2 mm in thickness. The reference and load samples were measured, according to ASTM D 4935-99 standard. An EMI SE value of at least 20 dB is typically

required to be commercially applicable in EMI shielding devices.[37] Usually a high loading of a filler is necessary to achieve EMI SE value of 20 dB or higher.[37] For example, an EMI SE of 21 dB was reported in an Epoxy matrix composite with 2 mm thickness using up to 10 vol % of reduced graphene oxide (rGO)[29] and an EMI SE of 20 dB was obtained in the polyetherimide matrix composite with 2.3 mm thickness using 5.9 vol % of rGO.[139] These high nanofiller concentrations may result in high production costs and poor composite processability.[37]

Figure 3.18 displays the EMI SE of some of the most conductive PMMA/ATO composites. The EMI SE is the difference between the SE values of the reference and the load samples. The EMI SE of the composites with 1.75 vol % and 1.06 vol % ATO were 18.8 and 15.6 at 1 GHz respectively. These values are not high enough to be commercially used however, the phase segregated conductive PMCs are promising candidates for the EMI SE applications because of the low percolation threshold of these composites. Typically, a volume electrical conductivity at least 1 S/m is required to achieve an EMI SE of 20 dB.[138] Note that the electrical conductivity of the compressed ATO was 12.1 S/m, which is 3~4 orders of magnitude lower than that of rGO.[140] It may be possible to fabricate a phase segregated conductive PMC with a higher electrical conductivity and a higher EMI SE using fillers with higher intrinsic electrical conductivity, such as graphene or CNT in the future.

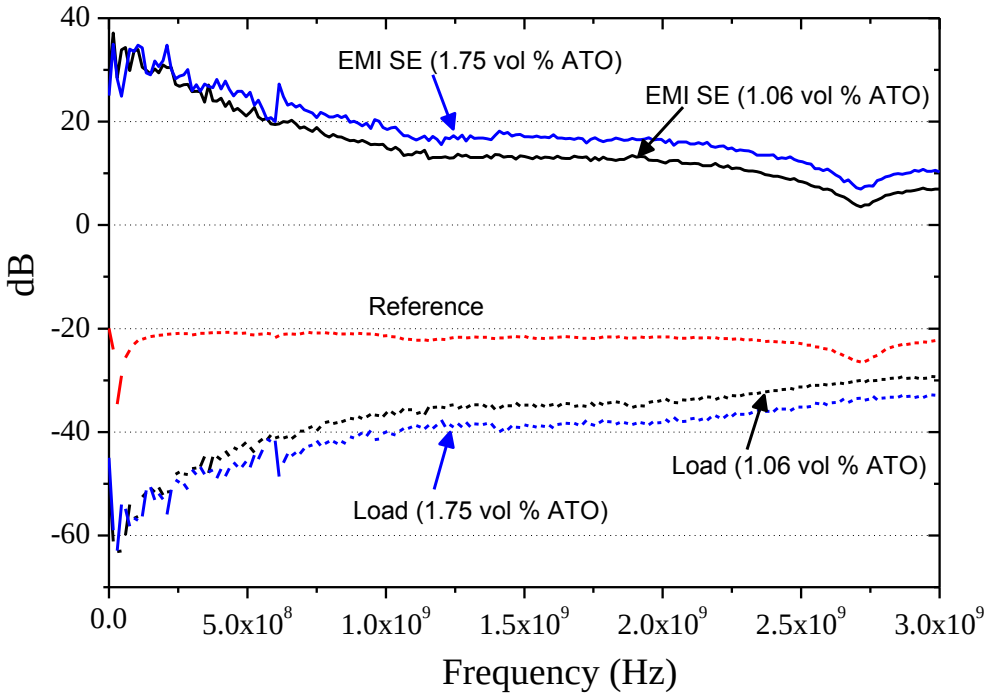

Figure 3.18. Electromagnetic interference shielding effectiveness (EMI SE) of PMMA/ATO composites (compression molded at 170 ℃ and 50.68 MPa with thickness of 2 mm). Note that EMI SE data are taken from S_{12} values because S_{11} values are negligible.

3.2.3 Finite Element Modeling of Percolation Behavior of Conductive PMCs

3.2.3.1 Modeling Overview

Electrical percolation is possible in insulator-conductor nanocomposites at very low concentration of fillers, when an insulating matrix is coated with conductive nanofillers using blending followed by compression molding into a nanocomposite.[6, 10, 30, 132] This concept can be applicable to all kinds of insulator-conductor composites and not just those mentioned here. It is very important to understand the mechanisms of this percolation to expand the possible applications. In this study, we used a finite element approach to solve the electric potential in the AC environments to calculate the impedance and conductivity using 2D and 3D models for the insulator-conductor composites.

The modeling steps used in this study include:

1. Selecting the mode in the COMSOL Multiphysics® AC/DC module.
2. Drawing the composite geometries.
3. Generating the mesh.
4. Defining the electrical properties in the domains and boundary conditions.
5. Solving and finding the field distributions.
6. Using the post-processing capabilities in COMSOL Multiphysics® to compute impedance and related electrical quantities.

Electrical conductivity in polymer matrix nanocomposites, with respect the microstructure driven percolation behavior, was studied by a finite element analysis in the AC environments. In the case of impedance measurements, the potential/current is time varying and usually harmonic. Impedance measurement setups involve small length scales (orders of mm) and low frequencies (mHz-MHz range). Hence, the electric field wavelength is typically several orders of magnitude larger than the dimensions of the

sample that is measured. In such a situation, the quasi-static approximation can be used.[141] The quasi-static form of Maxwell's equations for the electric potential was solved in the frequency domain using the AC/DC module of COMSOL Multiphysics® version 5.2.

3.2.3.2 2D Impedance Simulation of PMMA/ATO Nanocomposites

Figure 3.19 shows schematics of 1D percolation in 2D lattice as well as two possible filler distributions, i.e. a partially connected filler distribution and a disconnected filler distribution. Figure 3.19 (b) illustrates the changes in the electrical potential for the two different filler distributions.

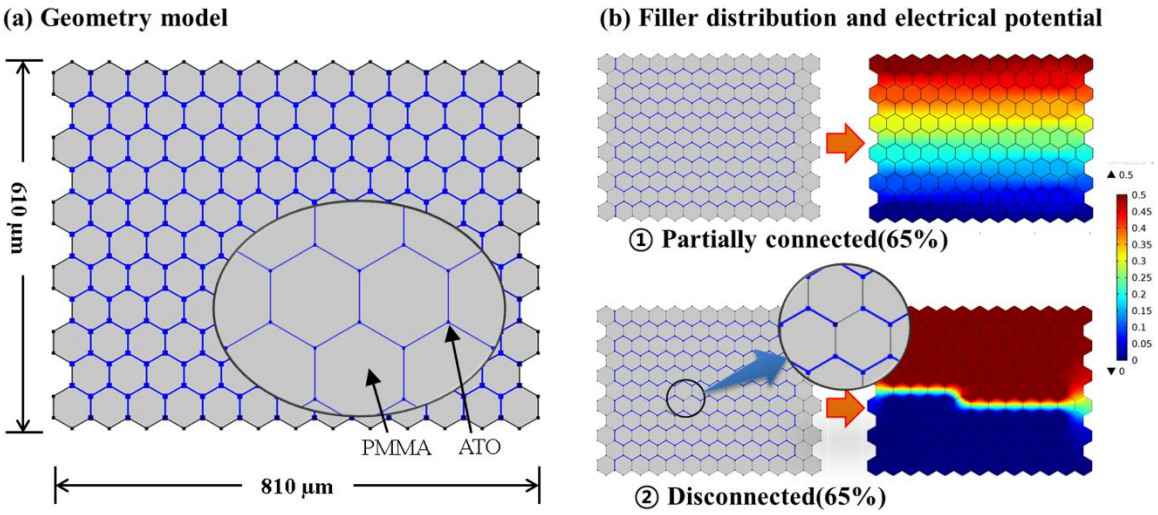

Figure 3.19. Schematic of 1D percolation in 2D lattice (a) 2D simplified geometry (b) filler distribution (partially connected and disconnected) and corresponding calculated electrical potentials.[6]

The impedance of the nanocomposites was obtained by postprocessing of the solved electric potential as previously described.[122, 123] The impedance simulation using perfect filler networks can predict the percolation threshold of phase segregated composites if the size ratio between the matrix and the filler is known. It can also predict the maximum electrical conductivity of the composite assuming that there is no size

distribution in the matrix and the filler, and the fillers are aligned in a perfect network. However, it needs to be modified to describe real composite systems with size distributions and imperfect filler chains.

First, the filler packing density model was introduced to accommodate disconnected filler chains while maintaining the percolated state. Filler packing density ranges from 1 (perfect network connection) to 0.65 (lower limit of 1D percolation in 2D lattice). The lower limit of percolation threshold (0.65) of 1D chain in 2D lattice is consistent with theoretical percolation theory by Frary and Schuh.[142] Figure 3.20 shows simulated DC conductivity for different filler chain density. There was a 3 orders of magnitude difference in DC conductivity.[6] The DC conductivity at the 65 % filler packing density can be considered as the conductivity at the percolation threshold. And the DC conductivity at the 100% filler packing density can illustrate the theoretical maximum conductivity in phase segregated composites.

Second, the electrical conductivity value of the filler should be representative of the properties of the real filler in the composite. Figure 3.20 shows the difference of simulated DC conductivity at different ATO conductivity values. The maximum DC conductivity of ATO can be above 5.8×10^3 S/m for spin coated films.[143] However, hot pressed ATO showed much lower value due to non-densification mechanism of ATO.[43, 132] For the simulation input, the electrical conductivity of compressed ATO NPs was measured in a specially designed in-situ measurement cell. The measured electrical conductivity of compressed ATO NPs showed 12.1 S/m.[1] It should be noted that the electrical conductivity of compressed ATO powder is the most realistic value for the fillers of the phase segregated composites, considering the possible packing states of ATO nanoparticles in the composite.

---

[1] In our previous works, the electrical conductivity of compressed ATO NPs was 31.8 S/m.[6, 132] It has been re-measured and the simulation was updated accordingly.

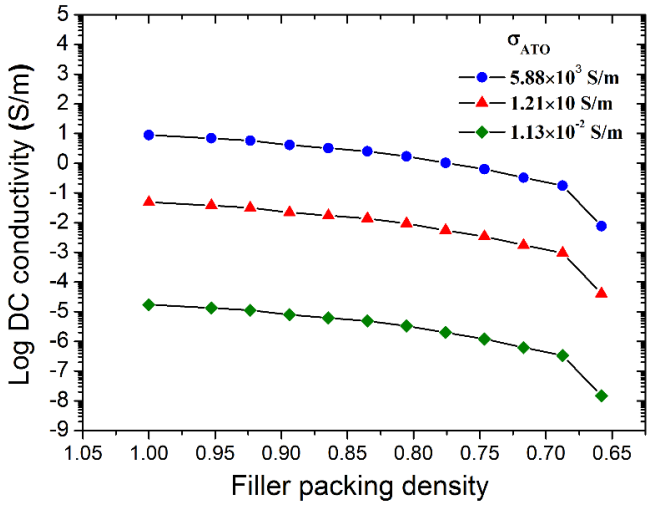

σ_{ATO} (S/m)	Conditions
5.88 x 10^{3}	Spin coated film[143]
1.21 x 10^{1}	Compressed powder
1.13 x 10^{-2}	Hot pressed bulk[132]

Figure 3.20. Predicted DC conductivity as filler packing density "1.0" illustrates perfect solid filler chains and "0.65" illustrates minimum density to maintain percolated state. Modified from reference.[6]

Figure 3.21 presents simulated AC conductivity curves as a function of frequency. Electrical percolation was clearly shown when the first continuous path of filler was connected between the top and bottom electrodes (port and terminal) similarly to what has been examined in the real materials. The onset of the first interconnected filler path was described as the "partially connected (65%)" in the 2D model. The electrical conductivity increased as additional percolation paths were connected. The transition from the frequency dependent to the frequency independent AC conductivity was monitored when the filler path was weakly connected.

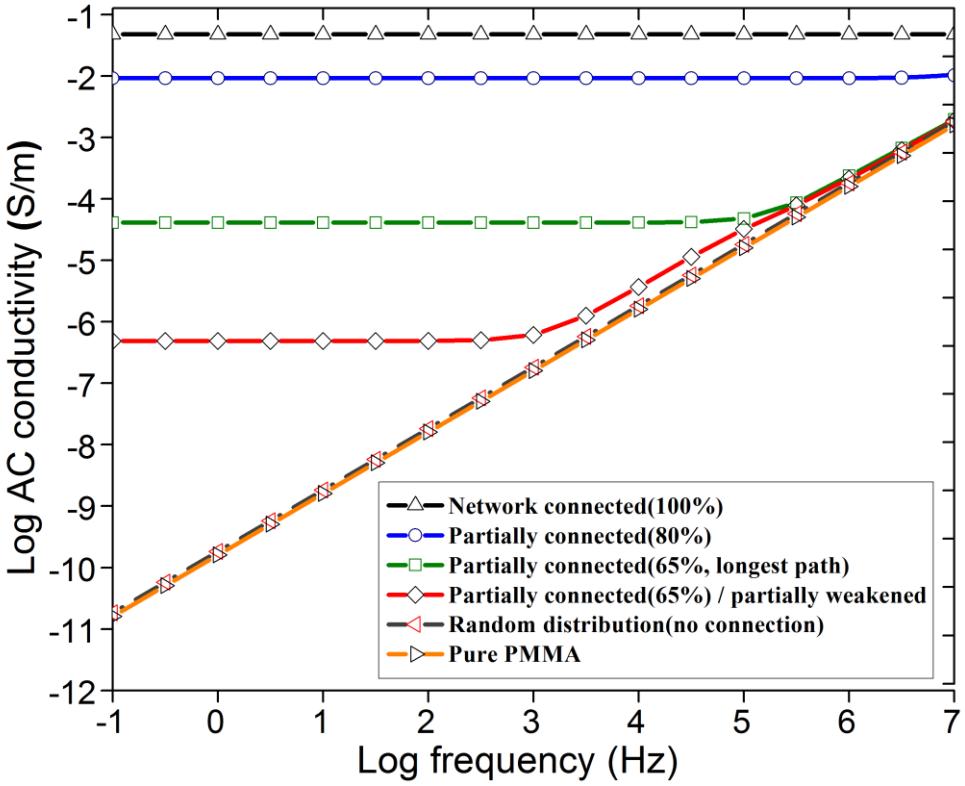

Figure 3.21. FEA simulated AC conductivity of PMMA/ATO nanocomposites using different 1D chain lengths and packing densities in 2D lattice. Modified from reference.[6]

Cappozzi et al. proposed a geometrical model to predict percolation threshold (ρ_c) of a phase segregated composite assuming;[130]

$$X_A = P_c \times X_B \tag{3.4}$$

where X_A is the volume percentage of the filler at which the edges of the polymer particles are completely occupied by the filler, X_B represents the amount of filler necessary to completely cover each faceted matrix particle. P_c is the critical percolation probability.[130] The critical percolation probability refers to the necessary probability that a single filler particle is part of a continuous chain in the matrix, and a value of P_C=0.775 was assumed, which is the critical probability estimated by Frary et al. for one dimensional percolation in a three dimensional lattice.[142]

The 2D simplified geometry, however, is not able to describe the actual geometry of the matrix, because it uses the extension of 2D geometry onto the 3rd axis to be able to calculate the impedance responses. Electrical percolation in the 2D simplified model occurred at the area fraction of the fillers to completely cover the edges of the matrix polygons. The FEA model assumes a perfect distribution of fillers rather than using the probability that the filler particles will touch in a given configuration.

Assuming the matrix particle geometry as truncated octahedra, the equivalent volume of the Voronoi types of matrix in terms of initial spherical PMMA particles can be estimated as,

$$\frac{4}{3}\pi r_P^3 = 11.31 a_p^3 \tag{3.5}$$

where, r_p is the average radius of the PMMA microspheres and a_p is the edge length of the truncated octahedra. Since the filler particles were assumed as cubes in the 2D model, the equivalent volume of a filler particle is

$$\frac{3}{4}\pi r_f^3 = a_f^3 \tag{3.6}$$

where, r_f is the average radius of filler nanoparticles and a_f is the edge length of the filler cube. In the simplified 2D model, the area fraction of the fillers to completely cover the edges of the matrix polygons is

$$3a_P \cdot a_f / 1.5\sqrt{3}a_P^2 \tag{3.7}$$

Combining (3.5) ~ (3.7), the area fraction can be written as 2.588 r_f/r_P. Figure 3.22 displays the change of area fraction of the filler to cover the edges of the matrix polygons in the 2D model as the size ratio between the matrix and the filler (r_{filler} / r_{matrix})

changes. It increases as the ratio (r_{filler} / r_{matrix}) increases. The area fraction of the network connected composite model in Fig. 3.21 was 0.1 %, which was lower than the experimental percolation threshold of monosize PMMA/ATO composites (0.18 %). This is because the total surface area of the matrix in 3D extension of the 2D model is smaller than that of the real 3D matrix.

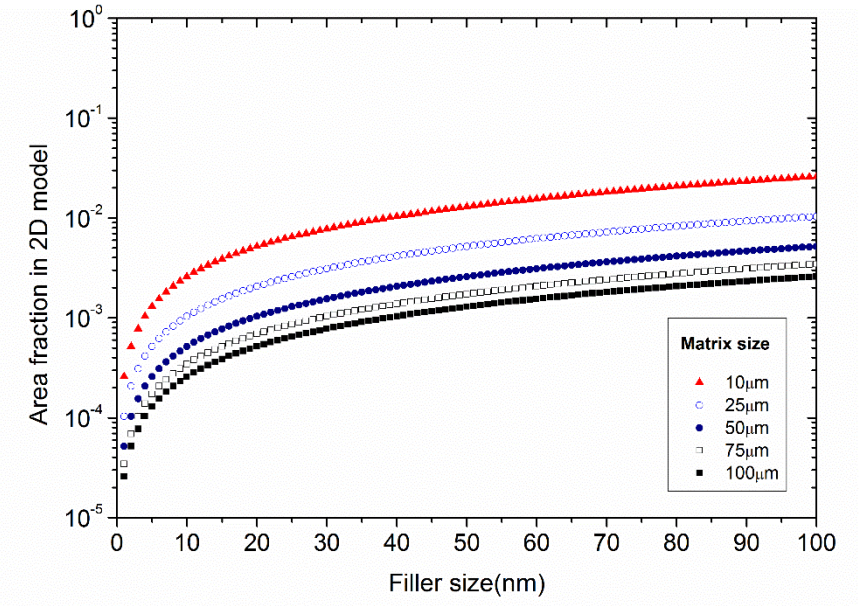

Figure 3.22. Area fraction of the fillers to completely cover the edges of the matrix polygons as a function of matrix and filler size derived from FEA simulations of 2D idealized segregated network microstructures.[6]

Although the 2D simplified model can describe percolation behavior of the phase segregated conductive composites using extremely low computational resources, it is not possible to describe a 1D percolation in a real 3D lattice using the 2D simplified model because the 1D percolation in the 2D simulation becomes a 2D percolation in a 3D lattice as the 2D simulation is based on the extension of the 2D geometry onto the 3rd axis. A 3D simulation is needed to improve predictability of the percolation behavior in the phase

segregated composite, because the percolation network is mostly along the edges (1D) of the matrix lattice near the percolation threshold.

3.2.3.3 3D Impedance Simulation of PMMA/ATO Nanocomposites

Figure 3.23 (a) shows the modeling geometry of the 3D simulation. A parallel plate capacitor configuration was used to calculate impedance responses between the top and the bottom electrodes. Various filler distributions in the 3D geometry were investigated to describe the inter-connectivity of nanoparticles along the edges of the matrix polyhedra. The thickness of the continuous filler chains was assumed to be 100 nm based on SEM images of a composite (Fig. 3.10). Figure 3.23 (b) shows simulated current density distributions in nanocomposites which contain different number of connected filler networks. Figure 3.24 shows simulated AC conductivity of nanocomposites with various percolation states. A filler packing density concept developed for the 2D simulation was also used in the 3D simulation with real geometry. According to the theoretical percolation study, the lower and upper limits of percolation threshold of 1D chains in 3D lattice are 0.225 and 0.775 respectively.[142] There was good agreement between the simulated and experimental electrical conductivities of the composites measured for 1.75 vol % ATO in PMMA (also shown in Fig. 3.24).

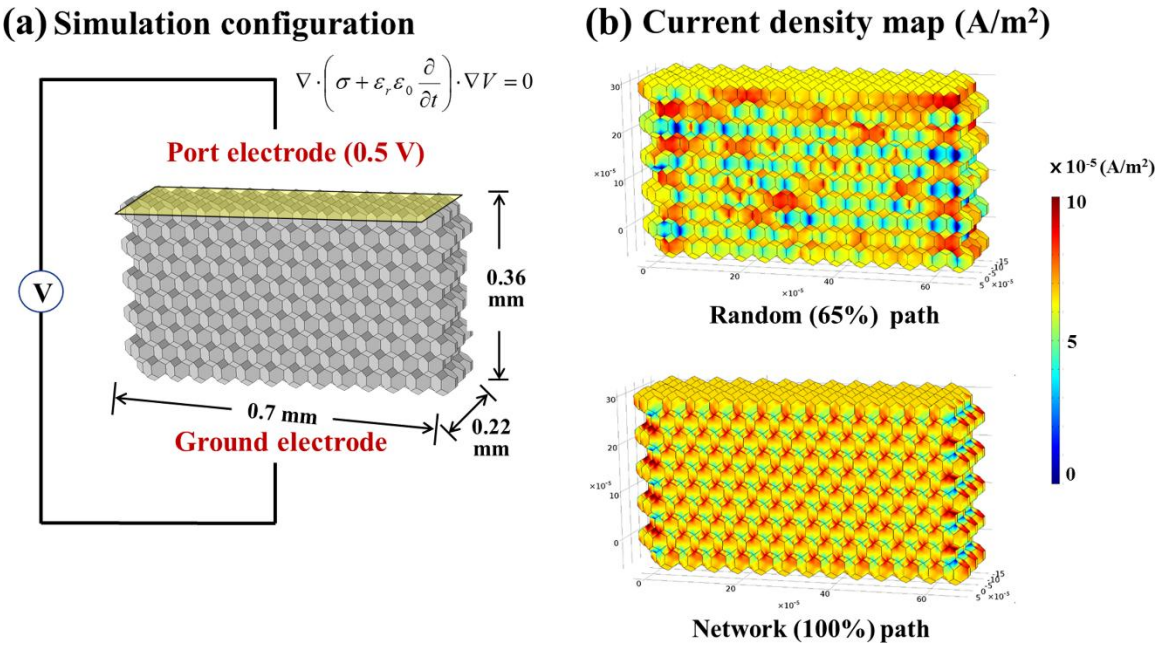

Figure 3.23. (a) FEA configuration and (b) simulated current density map of PMMA/ATO nanocomposites for different percolation paths (thickness of edges: 100 nm).

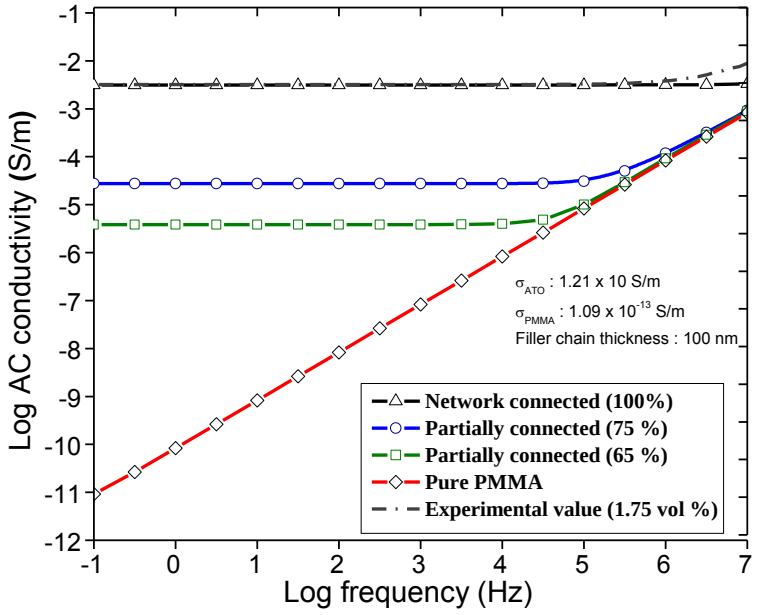

Figure 3.24. FEA simulated impedance of PMMA/ATO nanocomposites using different 1D chain paths and packing density. 100 % connected represents the maximum possible conductivity for the PMMA/ATO composites.

The geometry-based finite element model can be applicable to many different kinds of composite systems. Figure 3.25 shows examples of the three dimensional finite element analysis for some additional polymer matrix composites with different fillers. Figures 3.25 (a) and (b) show the FEA results of PMMA/indium tin oxide (ITO) composites and PMMA/carbon black (CB) composites respectively. The electrical conductivity values of ITO[2] and CB used in the simulation were 28 S/m and 251 S/m[144] respectively. The thickness of the continuous filler chains in the simulation was maintained as 100 nm for both composites. The FEA results of the PMMA/CB composites showed the maximum electrical conductivity about one order of magnitude lower than the previously reported experimental maximum value.[30] It is possible that the electrical conductivity of the filler used in the simulation was lower than the actual electrical conductivity of CB and/or the high degree of branching of the CB aggregates use in that study resulted in larger effective thickness of filler chains. However, the simulated maximum electrical conductivity of the PMMA/ITO composites was higher than the experimental maximum value.[130] It is also possible that the electrical conductivity of the filler used in the simulation was higher than the actual electrical conductivity value of ITO and/or the polydisperse PMMA used in the experiments resulted in a lower electrical conductivity than the FEA predicted value. In general; however, the three dimensional FEA models can predict the electrical properties of the phase segregated composites reasonably well if the electrical conductivity of the filler is known.

[2] The electrical conductivity of ITO was measured by T. Rudzik using the same method used for ATO.

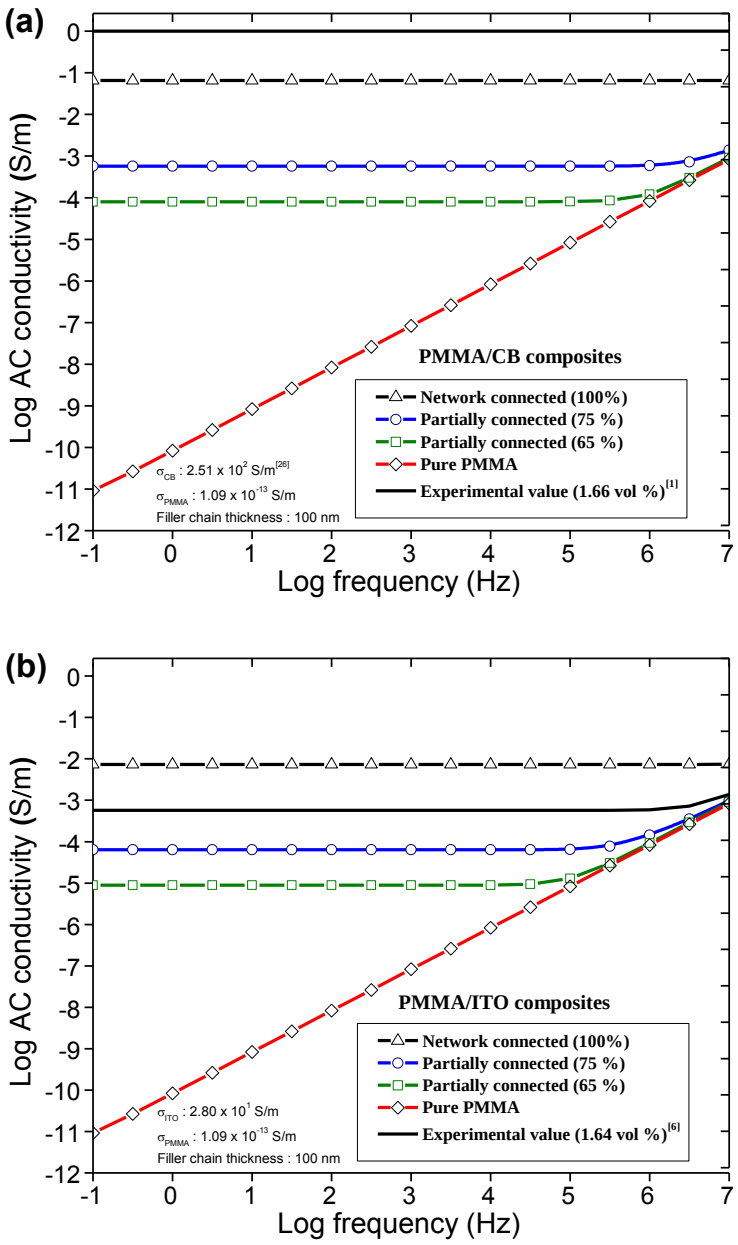

Figure 3.25. Examples of FEA study on PMCs with different fillers. (a) PMMA/CB composites and (b) PMMA/ITO composites

3.3 Conclusions

The phase segregated PMMA and ATO nanocomposites were made from monodisperse and polydisperse PMMA matrix polymer. Electrical percolation was achieved at very low concentration of ATO filler. The effects of the average size and the size distribution of the matrix polymer particles were analyzed. A lower percolation threshold was achieved for the composites containing the monosize PMMA which has a larger average particle size. (0. 18 vol % for the monosize materials and 0.27 vol % for the polydisperse materials). The composites with the monosize PMMA also showed a higher maximum electrical conductivity than the composites made with the polydisperse PMMA.

The correlation between processing, electrical conductivity and microstructure was investigated using impedance spectroscopy and SEM. The segregated lattice-like conductive network played a major role in achieving electrical percolation at low concentrations of the filler. It was evident that the microstructure was very sensitive to the processing conditions (i.e. temperature and pressure). The effects of the processing temperature and pressure were clearly detected in the thin composite samples with thickness of 0.6 mm. The processing conditions used resulted in two orders of magnitude difference in the electrical conductivity for the thin composite samples (0.6 mm) with the same ATO concentration. This was a result of the polymer matrix being squeezed and partially destroying the filler network when the molding temperature was too high and/or the pressure was high enough to cause filler penetration. The fractured surfaces showed trans-granular crack propagation due to low viscosity of the matrix and high filler penetration at the higher temperatures and pressures.

The finite element approach was selected for simulating the impedance of insulator-conductor nanocomposites, which have phase segregated microstructures. The 2D simplified model was used first to predict the percolation behavior of the phase segregated nanocomposites. The 3D simulation was used later to improve predictability

of electrical percolation of the nanocomposites. Good agreement was obtained between the experimental results and the modeling results by using a filler packing density model and realistic filler conductivity values. The simulation model can be applicable to many different kinds of nanocomposite systems with phase segregated structure and not just those that were presented here. It may be possible to fabricate a highly conductive nanocomposite using fillers with higher electrical conductivity, such as graphene, CNT, or metallic nanoparticles in the future. Future works also include more quantitative analysis of the fabrication conditions on the electrical, optical and mechanical properties of these composites for possible applications, including EMI shielding, novel interconnects, transparent electrodes, metal replacement and bipolar plates.

CHAPTER 4

DIELECTRIC NANOCOMPOSITES WITH UNIFORMLY DISTRIBUTED NANOPARTICLES

In this chapter polymer matrix composites in dielectric applications are presented and discussed. Unlike the polymer matrix conductive composites, polymer matrix dielectric composites should avoid electrical percolation. Therefore, physical contact between the nanofillers has to be prevented. Furthermore, a uniform distribution of nanofillers is more favorable in this case. The particular focus in this chapter is on the materials and fabrication method used to increase the effective dielectric permittivity while maintaining low dielectric loss. This chapter also focuses on dielectric characterization of the composites. For the quantitative analysis of charge migration and accumulation in the polymer matrix composites, an equivalent circuit model is proposed. Finite element analysis was conducted to help improve predictability of the dielectric properties of polymer matrix hybrid composites with filler interactions. The work presented in this chapter covers two topics: (1) the effect of BT content at different volume fraction with and without CNT additives and (2) the effect of BT particle size on the properties.

4.1 Experimental Procedure

4.1.1 Filler and Matrix Components used

Barium titanate (BT) was obtained from Sigma-Aldrich. The BT nanoparticles were imaged using Hitachi HT7700 TEM. Figure 4.1(a) shows a TEM image of commercial BT nanoparticles. The BT particle size was 77.8 ± 5.9 nm. Additionally, BT nanoparticles with different sizes ranging from 25 to 250 nm were prepared by a hydrothermal reaction method in a 200 ml Teflon-lined autoclave according to

references[145, 146] with some modifications. The details of the hydrothermal reaction will be discussed in Appendix A. Barium hydroxide octahydrate ($Ba(OH)_2 \cdot 8\ H_2O$, Sigma Aldrich, 98%) solution was used as barium fountain. Anatase titanium oxide nanoparticles (18nm, US Research Nanomaterials, 99.9%) were dispersed in the 0.2 M $Ba(OH)_2 \cdot 8H_2O$ solution using ultrasonication and magnetic stirring for 1 h. The molar ratio of titanium and barium was maintained as 1:1.5 throughout the whole process. After sealing, the autoclave was heated to 180 ℃ for different periods of time and then cooled down to room temperature. The precipitate was collected and washed several times through centrifugation and vortex mixing with dilute acetic acid, DI water and ethanol, then dried on a hot plate at 80 ℃ overnight. Poly (vinylidene fluoride) (PVDF) and 3-(Methacryloyloxy) propyltrimethoxysilane (MPS) were obtained from Alfa Aesar. Poly (vinylidene fluoride)-hexafluoropropylene (P(VDF-HFP)) was obtained from Sigma Aldrich (MW 400,000). Multiwall carbon nanotubes (MWCNT) were obtained from cheaptubes.com with the following specifications: 0.5–2.0 μm in length, 8–15 nm in diameter, > 95 wt % purity with < 1.5 wt % ash (Image of multiwall carbon nanotubes shown in Fig. 4.1(b)).

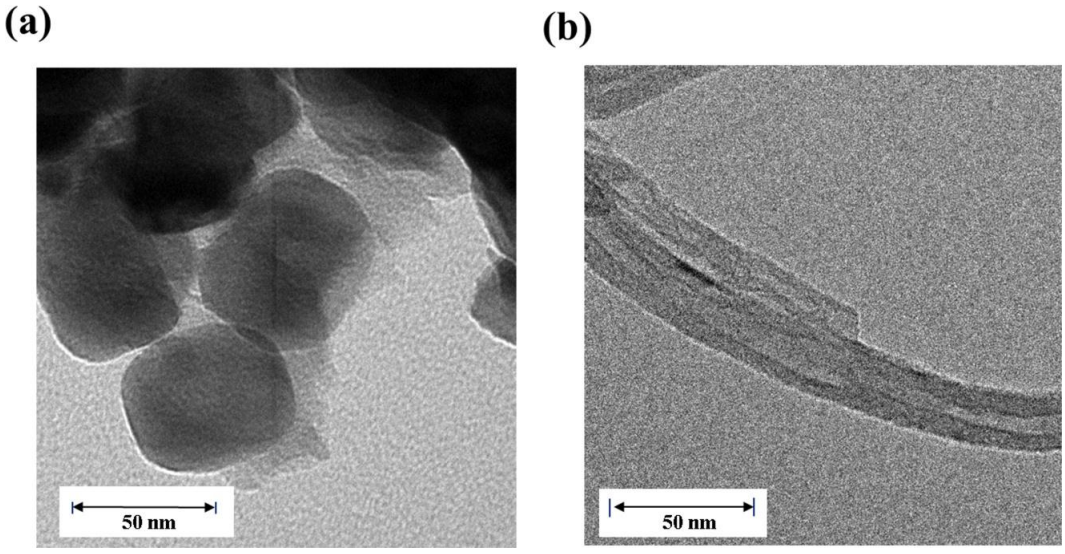

Figure 4.1. TEM images of commercial (a) BT nanoparticles (b) MWCNT.

4.1.2 Composite Fabrication Procedure

The matrix PVDF polymer was dissolved in DMF by ultrasonication and the solid to solvent weight ratio was 1:10. Different amounts of BT were added on the basis of the desired concentration of BT in the final composites. Homogeneous dispersion of nanoparticles can be achieved by ultrasonication and speed mixing (DAC 150 Speed Mixer) for 10 min. MWCNT was added to the mixture and dispersed in the ultrasonicator and speed mixer for another 20 min. Prior to blending, the surfaces of BT nanoparticles and MWCNT were modified by 0.5 wt % silane coupling agent (MPS) in 1:99 (v/v) acetone/H_2O mixture to improve the interfaces between the matrix and fillers and to prevent sub-microscopic agglomeration of nano-fillers. The surface modified fillers were rinsed repeatedly to remove un-reacted MPS. After drying on a hot plate at 80 ℃ overnight, surface modified BT nanoparticles (NPs) were pulverized using a mortar and pestle to break aggregated particles.

It is not uncommon for the nano-fillers to re-aggregate during the processing; especially carbon based 1D material.[102, 147, 148] A quick phase separation based on miscible and immiscible coagulation method was used to minimize re-aggregation of the fillers.[11, 83, 147] As shown in Fig. 4.2, a thin layer of composite suspension was spread on the glass substrate. Then, a thin layer of DI water was applied in between the composite and glass substrate. The solvent was extracted from the suspension immediately, preventing re-aggregation of the nano-fillers. The free standing thin films were dried on a hot plate at 80 ℃ for 10 min. To obtain void-free dense composite samples, the dried composites films were hot pressed at 190 ℃ for 20 min. To increase breakdown strength of the nanocomposites, composite samples were annealed at 200 ℃ for 10 min. and quenched in ice water. The thickness of the samples was controlled to be 100 μm for microstructural and dielectric analysis and 10 μm for high voltage breakdown strength test.

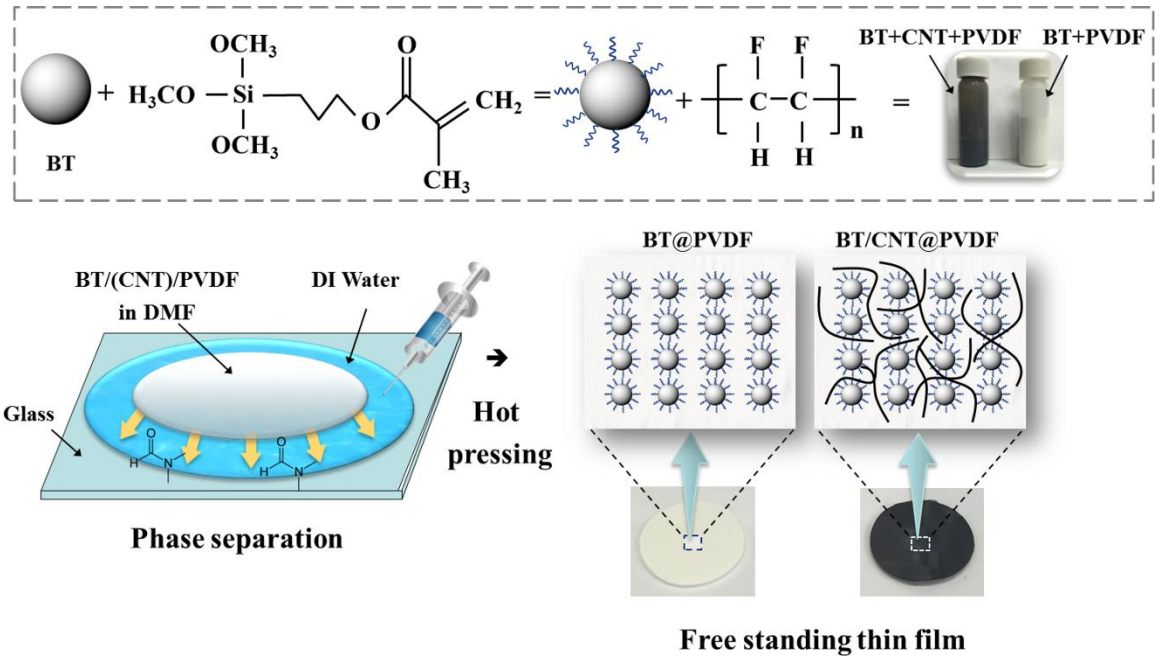

Figure 4.2. Schematics of steps for making BT/MWCNT/PVDF hybrid nanocomposites using a simple phase separation method. Optical images in the bottom right show appearance of composites containing 37.1 vol % BT with 0 vol % MWCNT (left), and 3 vol % MWCNT (right).

4.1.3 Microstructural, Thermal, and Electrical Characterization

4.1.3.1 Microscopy

A cold field emission scanning electron microscope (CFE-SEM, Hitachi SU8230) was used for microstructural characterization of the nanocomposites. Images were acquired from the top surfaces and fractured cross-sections of the nanocomposites using an accelerating voltage of 1.0 kV. A transmission electron microscope (TEM, Hitachi HT7700) was used to analyze the morphology of BT NPs and MWCNT with accelerating voltage of 120 kV.

4.1.3.2 Fourier Transform Infrared Spectroscopy

The crystalline phases present in PVDF samples were confirmed by Fourier transform infrared spectroscopy (FTIR spectrometer, Thermo Scientific iS5). PVDF and

PVDF-HFP films (10 μm thickness) were prepared by hot pressing at 190 ℃ with uni-axial pressure of 38 MPa for 20 minutes. The polymer films were scanned before and after an annealing heat treatment at 200 ℃ for 10 minutes, followed by quenching in ice water.

4.1.3.3 X-ray Diffraction and Thermal Analysis

X-ray diffraction (XRD) was primarily used for crystallographic analysis of pure PVDF, BT nanoparticles (NPs) and nanocomposite samples. An x-ray diffractometer (XRD, PANanalytical X'Pert PRO Alpha-1) with Cu Kα radiation was used and scans were conducted in the range of 20° to 80° with a step size of 0.0167°.

A thermogravimetric analyzer (TGA) combined with a differential scanning calorimeter (DSC) (TA Instruments SDT Q600) was used for thermal analysis of BT NPs, PVDF and nanocomposites. The values of the enthalpy (ΔH) of fusion, which is proportional to the degree of crystallinity of each sample, were determined by differential scanning calorimetry (DSC, TA Instruments SDT Q600) using a heating rate of 10 ℃ / min under a nitrogen atmosphere. A thermogravimetric analyzer (TGA, TA Instruments SDT Q600) was used to measure the surface coverage of MPS on BT nanoparticles using a heating rate of 20℃ / min under a nitrogen atmosphere.

4.1.3.4 AC Dielectric Measurements

An impedance spectroscopy frequency response analyzer (Solartron 1260) together with a 1296 dielectric interface (Solartron 1296) was used for the dielectric characterization of the nanocomposites. Prior to impedance measurements, a vacuum sputter coater (Denton Vacuum Desk II Turbo) was used to deposit Ag (nominal purity of 99.9%) electrodes (3 mm in diameter). All of the AC electrical measurements were taken using 0.5 V_{rms} without any DC bias. The real and imaginary permittivity values were calculated from the measured impedance data according to the following equations:

$$\varepsilon' = \frac{-Z''}{2\pi f \varepsilon_0 [(Z')^2 + (Z'')^2]} \cdot \frac{l}{A} \quad (4.1)$$

$$\varepsilon'' = \frac{-Z'}{2\pi f \varepsilon_0 [(Z')^2 + (Z'')^2]} \cdot \frac{l}{A} \quad (4.2)$$

where ε_0 is the permittivity of free space (8.854 x 10^{-12} F m^{-1}), Z' and Z'' are the real and imaginary impedances of the dielectric medium respectively, *A* is the area of the electrodes and l is the distance between the electrodes.

4.1.3.5 High Voltage DC Breakdown Tests

A RK2674 dielectric withstand voltage test system was used at a ramping rate of 20 V/s as a slow rate-of-rise breakdown strength test with a limit current of 1 mA. No samples broke down in less than 120 s. Prior to the breakdown tests, pure polymer and nanocomposite thin films were electroded (1mm in diameter) using a vacuum sputter coater (Denton Vacuum Desk II Turbo).

4.2 Results and Discussion

4.2.1 Component Synthesis and Properties

4.2.1.1 Hydrothermal Synthesis of Barium Titanate Nanocrystals with different sizes

The synthesized BT with different particle sizes was characterized by x-ray diffraction. The obtained XRD patterns were indexed with the X'pert High Score program. Figure 4.3 shows the obtained patterns of 5 samples, corresponding to BT particle sizes of 25, 38, 97, 154, 256 nm. The BT particle size increased with hydrothermal reaction time. The smallest nanoparticles (NPs) were obtained (25 nm), when the reaction was held for 3 h. However, the final BT NPs after washing contained up to 12.03 % of un-reacted TiO_2.[149]

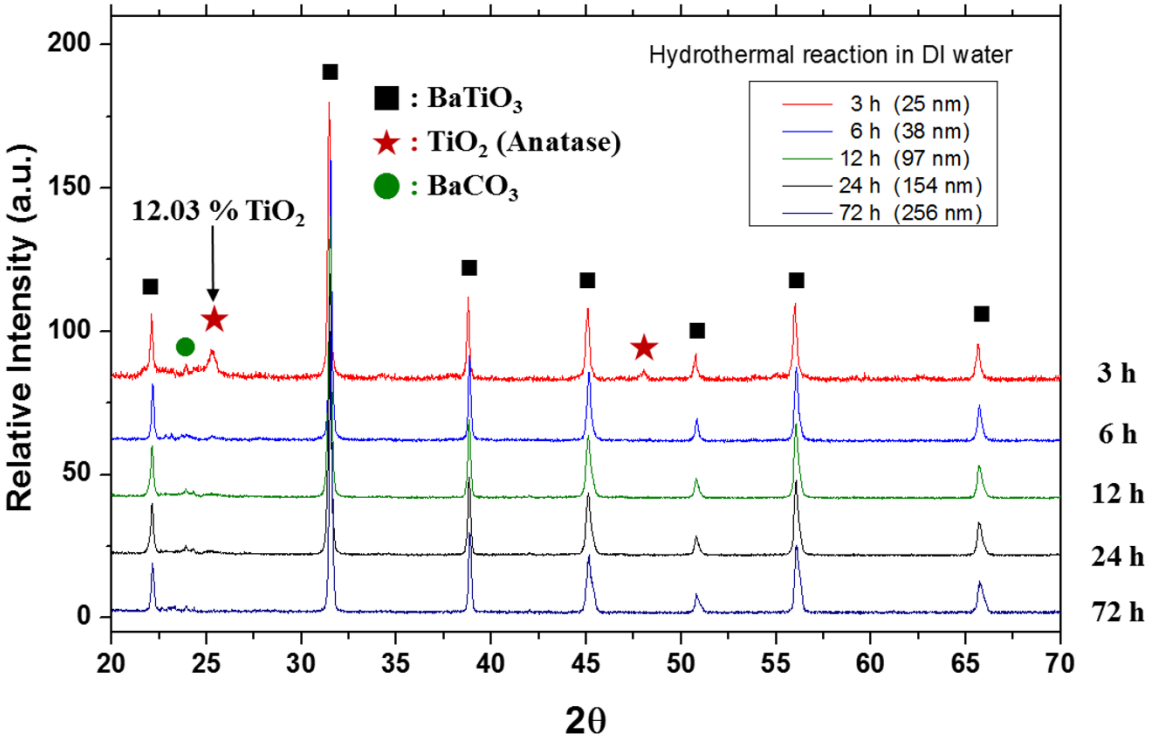

Figure 4.3. XRD patterns of synthesized BT nanoparticles.

XRD shows crystalline BT patterns (JCPDS, 81-2203) without any indication of un-reacted TiO_2 or barium carbonate ($BaCO_3$) when the reaction was held more than 6 h. The size of synthesized BT was 38.63 ± 1.89 nm for 6 h of reaction and increased to 97.21 ± 9.54 nm, 153.94 ± 6.42 and 256.23 ± 10.87 nm for 12, 24 and 72 h of reactions respectively. Although the spherical BT NPs were mostly used as fillers in this study, BT nanocrystals can be synthesized in different shapes, such as cubic, starfish-like and nanowire depending on the hydrothermal reaction parameters.[99, 145] More information about hydrothermal reaction for different morphology is described in Appendix A.

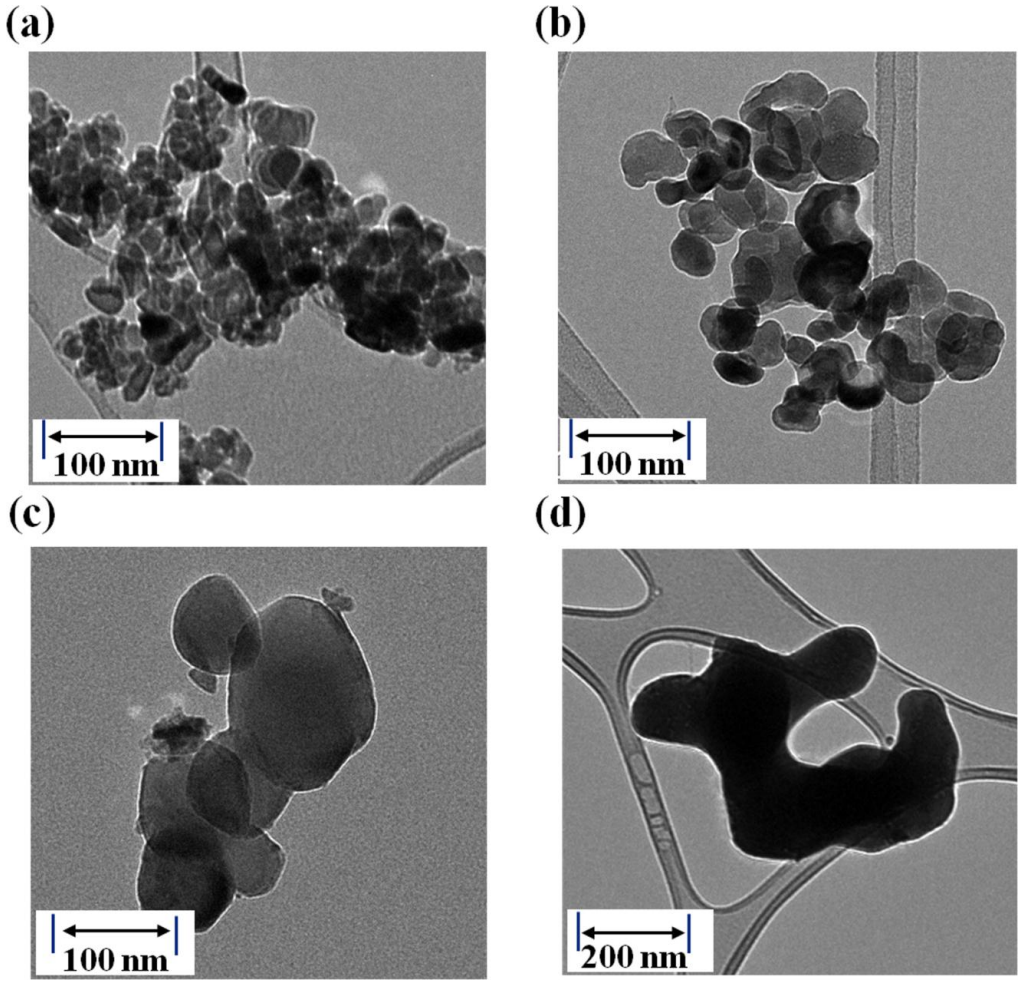

Figure 4.4. TEM images of hydrothermally synthesized BT in DI water at 180 ℃ for (a) 3 h, (b) 6 h, (c) 12 h and (d) 24 h.

Figure 4.4 shows TEM images of some synthesized BT NPs with different sizes, corresponding to (a) 25 nm, (b) 38 nm, (c) 97 nm and (d) 153 nm. All TEM samples were prepared by depositing a drop of diluted suspensions in isopropyl alcohol on a carbon film coated copper grid. Figure 4.5 shows the particle size of the synthesized BT as a function of reaction time. When BT was synthesized in a 30% ammonia solution, the particle size was much smaller[3] than the BT synthesized in water for the same reaction time. It was 33.09 nm for 24 h reaction and 47.81 nm for 48 h reaction. However, the synthesized BT in the ammonia solution was not used in the current works, because the ammonia may also change the surface chemistry of BT NPs, which can affect the interfaces between BT and the polymer matrix.

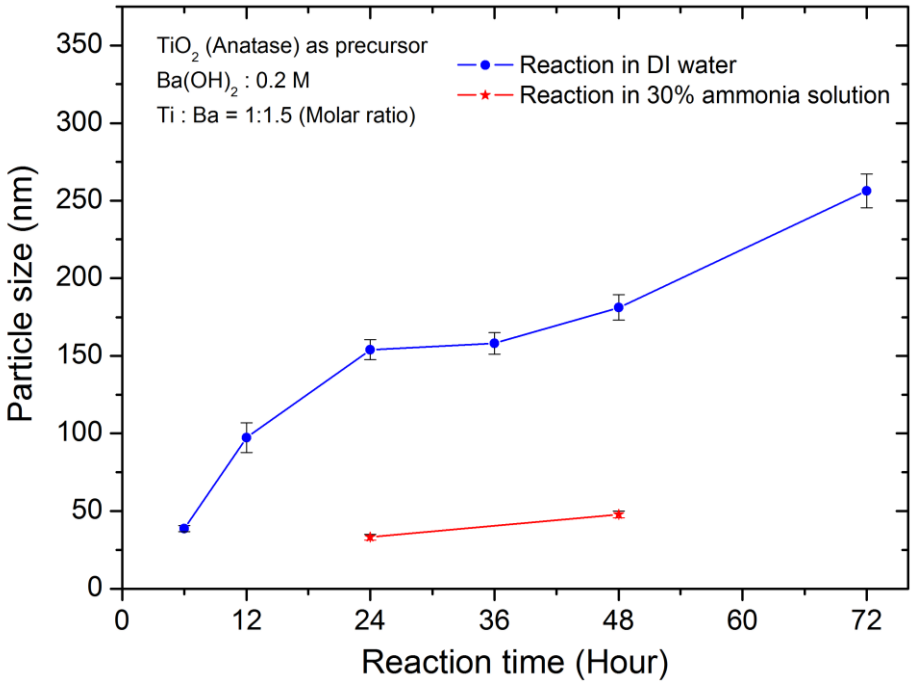

Figure 4.5. Particle size of synthesized BT as a function of reaction time at 180 ℃ in DI water (blue circle) and in 30% ammonia solution (red star)

[3] It is known that the ammonia can suppress the size and can lead narrower size distribution of BT nanoparticles.[146]

4.2.1.2 Surface Functionalization of Barium Titanate Nanocrystals

The surface modification of BT nanoparticles was carried out under acidic conditions, as suggested in the literature.[11, 149] The hydrolysis and condensation of organo-silane are slow and controllable, and most of the silanol molecules are covalently bonded to the surface of the BT nanoparticles. Figure 4.6 shows the TGA results for the unmodified BT and the surface modified BT. The overall weight loss from the surface layer of MPS was 2.15 %.

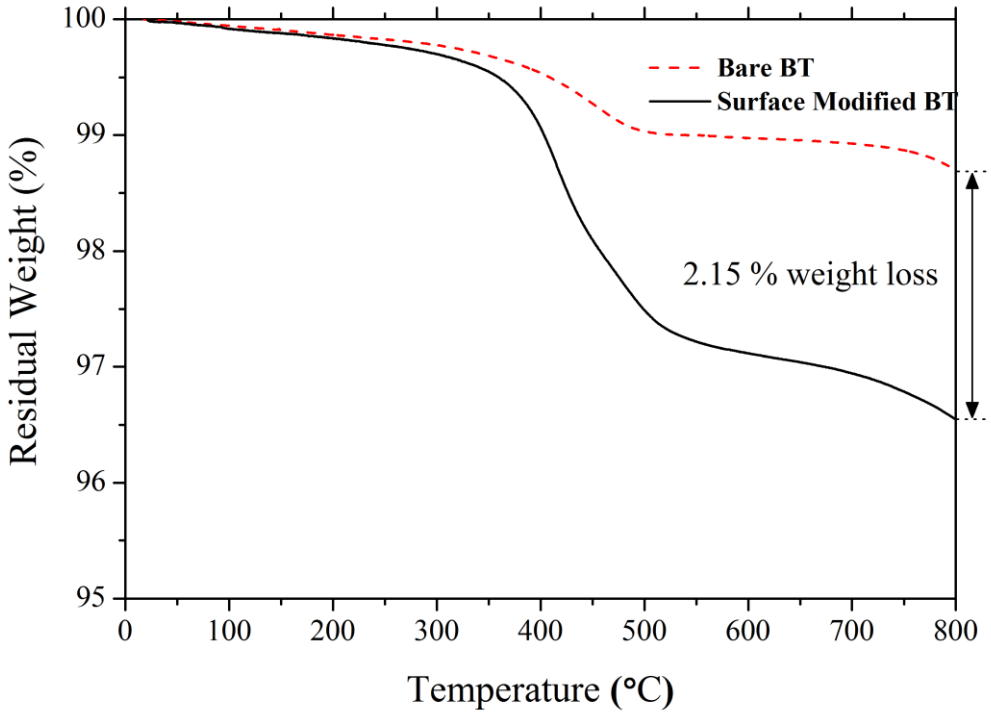

Figure 4.6. Thermogravimetric analysis of BT before and after surface modification with MPS.

The FT-IR spectra of the BT nanoparticles with and without MPS modification are shown in Fig. 4.7. In the BT NPs with MPS modification, some characteristic absorption bands were detected at 1296 cm^{-1} and 1195 cm^{-1}, which represent C–O–C bonds in the MPS molecule.[150] And a peak at 1125 cm^{-1} represents Si-O-C bond, which is assigned to the MPS molecule that is covalently bonded to the BT surface.[151] More

importantly, a peak was observed around 1040 cm^{-1}, which specifically represents the Si–O–Ti bond, confirming the successful MPS modification of the BT nanoparticles surface.[152, 153] Both commercial and synthesized BT nanoparticles were effectively modified by MPS.

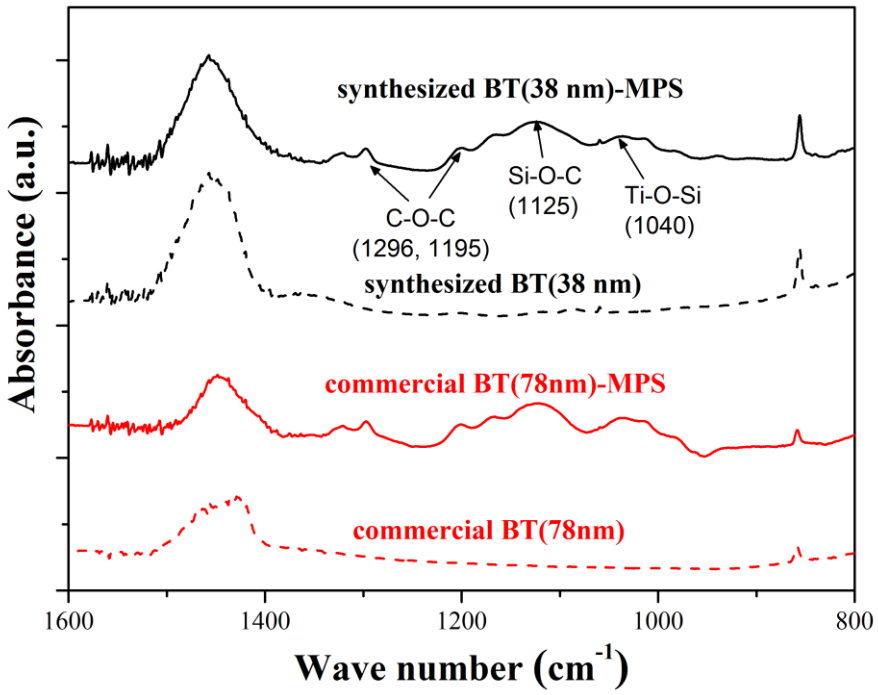

Figure 4.7. FTIR spectra of BT nanoparticles before and after surface modification with MPS.

4.2.1.3 Phase and Crystallinity of Matrix Polymer (PVDF)

PVDF has at least four crystalline phases (α, β, γ and δ). Among them, a non-polar α phase is most commonly obtained from melt crystallization at any temperature. A ferroelectric β phase is the desirable phase in many applications, due to its ferroelectric characteristics. The crystallinity and the ferroelectric characteristics of PVDF phases can affect the charge accumulation ability of the nanocomposites. Figure 4.8 (a) shows FTIR spectra. The characteristic absorption bands of α phase[154] were detected at 530, 615, 766,

795 and 974 cm^{-1} in the PVDF film hot pressed from powder, while the absorption bands of β phase[154] were mostly detected at 511 and 840 cm^{-1} in the PVDF film hot pressed after coagulation phase separation. The α to β phase transformation of PVDF has been previously reported when crystalline α phase is stretched at elevated temperature, typically 80-120 ℃.[154] The microstructural transformation was reported to occur from a ringed spherulitic structure of α phase to a micro-fibrillar structure of β phase when the PVDF α phase was stretched.[118] Interestingly, there was a phase transformation from α to β during our composite fabrication. The fraction of β phase of the PVDF film hot pressed after coagulation was 0.785, while that of the PVDF film hot pressed from powder was 0.326. Differential scanning calorimetry (DSC) results shown in Fig. 4.8 (b) indicate that the enthalpy of melting of the PVDF hot pressed after coagulation was 35.6 J/g while that of the PVDF hot pressed from powder was 23.85 J/g. The crystallinity of PVDF was calculated according to

$$\Delta X_c = \frac{\Delta H_m}{\Delta H_{100}} = \frac{\Delta H_m}{x\Delta H_\alpha + y\Delta H_\beta} \tag{4.3}$$

where x and y are the contents of α and β phases respectively, ΔH_α (93.07 J/g) and ΔH_β (103.4 J/g) are the enthalpies of melting of the 100 % crystalline α and β phases.[154] The calculated degree of crystallinity of the PVDF hot pressed after coagulation was 35.19 %, while it was 24.73 % for the PVDF hot pressed from powder. The increased crystallinity of PVDF can improve the interfacial polarization of nanocomposites with hybrid fillers.

The x-ray diffraction patterns of both PVDF films are shown in Fig. 4.9 (a). The most intense peak in the PVDF hot pressed after coagulation phase separation was β (200) at 2θ = 20.57 and the relative intensities of peaks from α phase were much smaller

to be clearly detected. These spectra confirm the assignment made based on FTIR and TGA data.

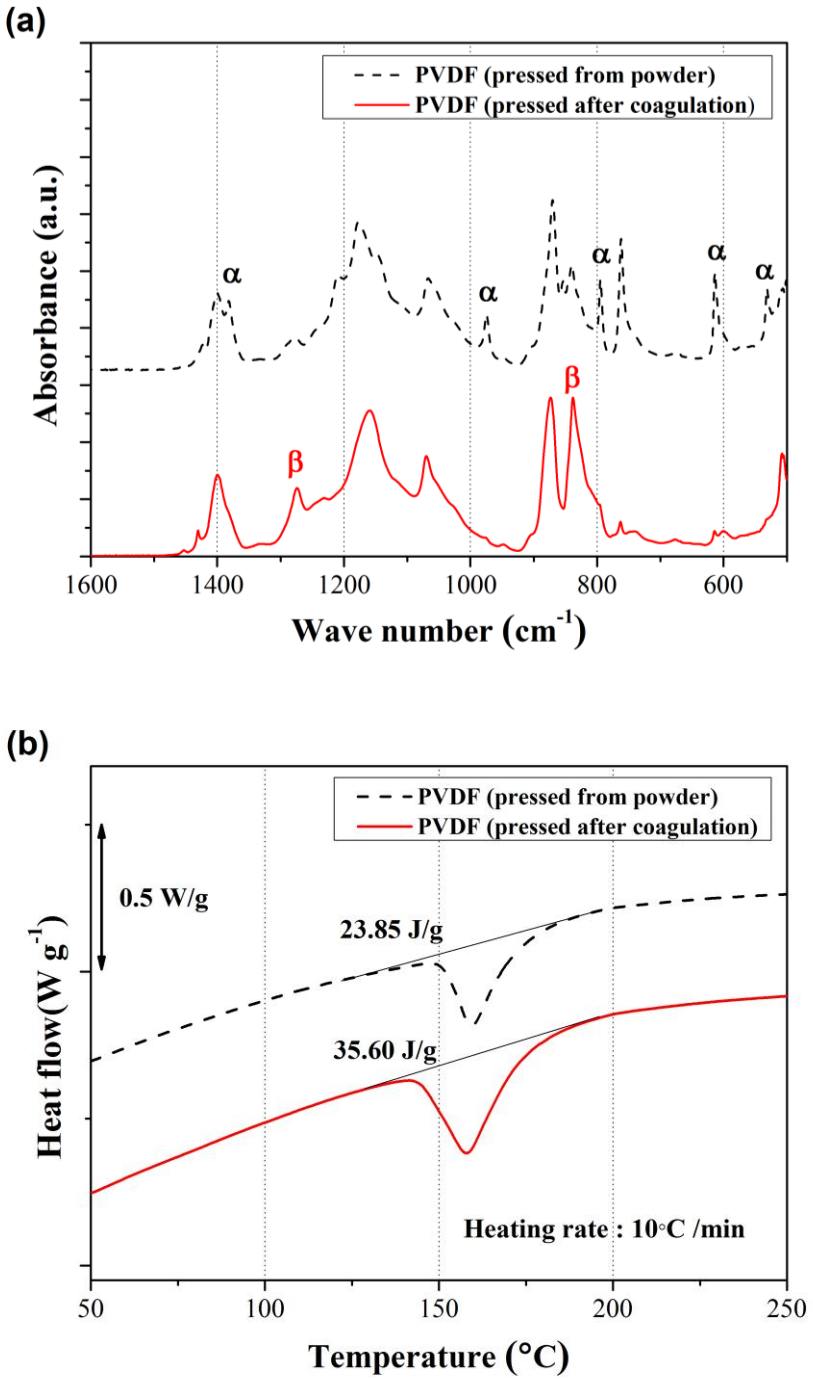

Figure 4.8. (a) FTIR and (b) DSC results for pure PVDF; hot pressed from powder (dash) and hot pressed after coagulation (solid).

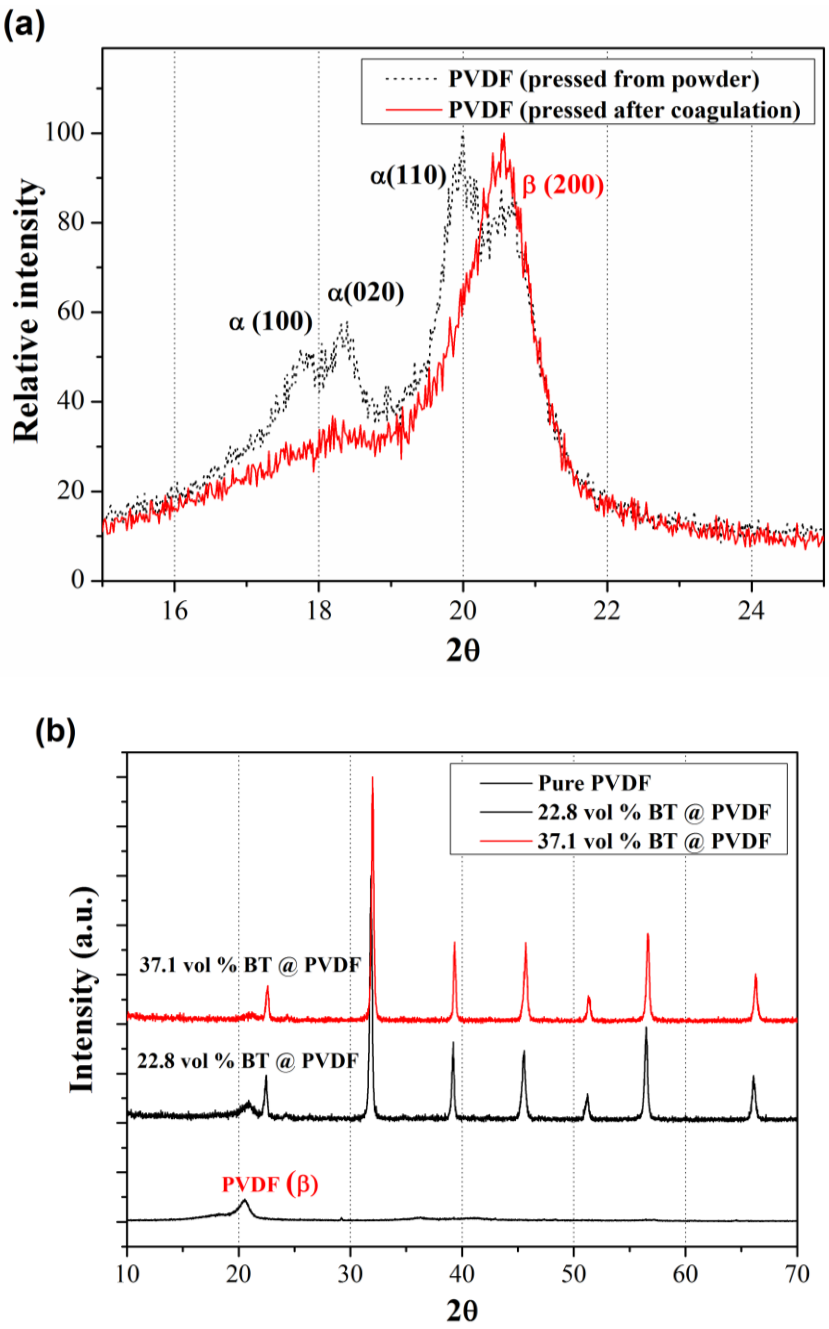

Figure 4.9. (a) XRD patterns for pure PVDF film; hot pressed after coagulation (solid) and hot pressed from powder (dash), (b) XRD patterns for pure PVDF (bottom), nanocomposites containing 22.8 vol % BT (middle) and 37.1 vol % BT (up).

Figure 4.9 (b) shows XRD patterns of the pure PVDF and the nanocomposites containing different amounts of BT NPs. As described earlier, PVDF matrix in the nanocomposites was β phase after composite fabrication.

A ferroelectric β phase is the desirable phase in many applications, due to its ferroelectric characteristics, however breakdown strength of β phase is often lower than that for the α and γ phases.[51, 67] PVDF α phase can be more favorable than β phase for some applications under high electric field, such as high energy density electric energy storage. The breakdown strength of the polymer matrix hybrid nanocomposite can be improved by phase transformation from ferroelectric β to non-ferroelectric α. To improve the breakdown strength of the polymer matrix hybrid nanocomposite, the β phase was transformed into α phase, during annealing heat treatment at 200 ℃ for 10 min followed by quenching in ice water.

Figure 4.10 (a) and (b) show FTIR spectra of PVDF and PVDF-HFP films respectively, before and after annealing heat treatments followed by quenching. The characteristic absorption bands of α phase[154, 155] were detected at 530, 615, 766, 795 and 974 cm^{-1} in the heat treated PVDF and PVDF-HFP films, while the absorption bands of β phase[154, 155] at 511 and 840 cm^{-1} were detected in the untreated films. The fraction of β phase of the untreated PVDF and PVDF-HFP films were 0.754 and 0.737 respectively, while those of the heat treated films were 0.318 and 0.357 respectively. Figure 4.11 (a) and (b) show, differential scanning calorimetry (DSC) results. The calculated degree of crystallinity of the PVDF was decreased from 34.75 % to 27.1 %, after annealing heat treatments, while that of the heat treated PVDF-HFP was unchanged. However, the melting temperatures of PVDF and PVDF-HFP films were increased by 1.54° and 1.1° respectively, after the annealing heat treatments. The results indicate that the annealing followed by quenching helped to reform the α phase, which is believed to have higher breakdown strength than the β phase.[51, 67] However, the positive influences of phase transformation

on the breakdown strength can be minimized in the heat treated PVDF film, which showed decreased crystallinity, unlike PVDF-HFP film.

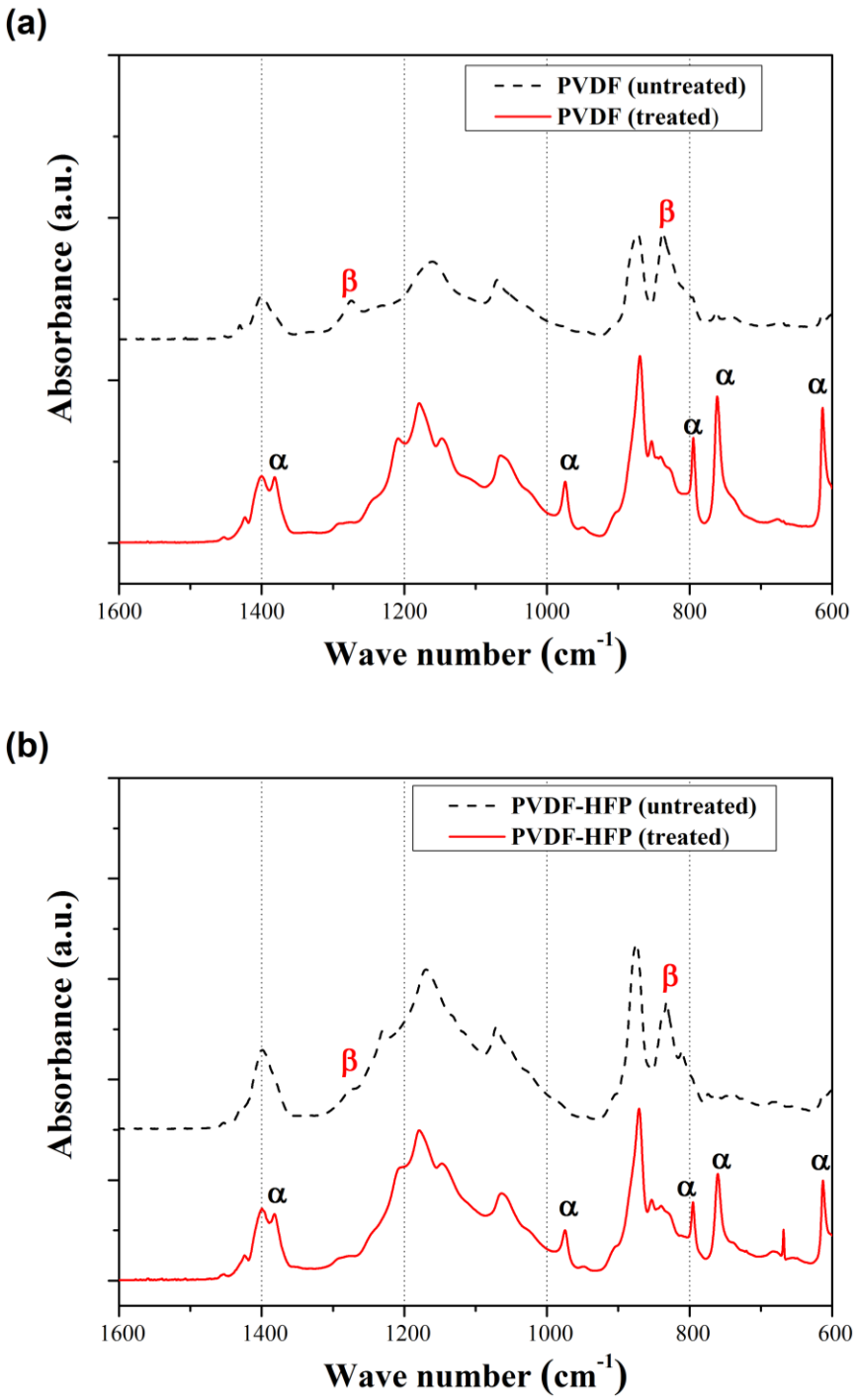

Figure 4.10. FTIR spectra of heat treated and untreated (a) PVDF and (b) PVDF-HFP films. [83]

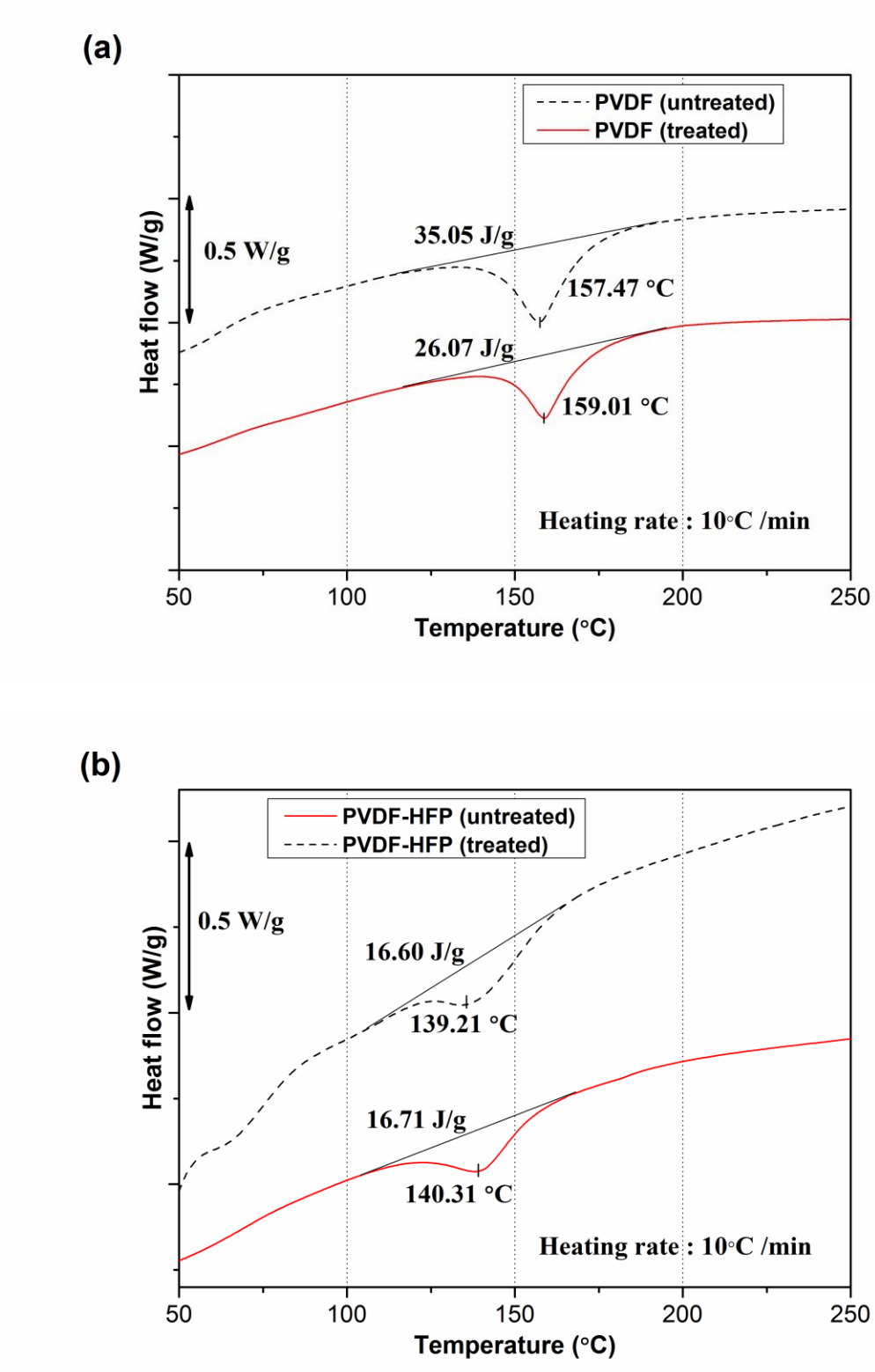

Figure 4.11. DSC results of heat treated and untreated (a) PVDF and (b) PVDF-HFP films. [83]

4.2.2 Characterization and Analysis of Results

4.2.2.1 Effects of Uniformly Distributed High-*k* Fillers

Figure 4.12 shows SEM images collected from the bulk nanocomposites containing 22.82 vol % of BT NPs. Figure 4.12 (a) was obtained from a composite with SDBS aided filler dispersion and Fig. 4.12 (b) was obtained from a composite with a MPS surface modified filler.[11] No evidence of macroscopic filler clustering was found in either composite. The BT NPs were uniformly dispersed. The immediate precipitation of PVDF prevented the macro clustering of nano-fillers. Using SDBS or attaching silane molecules on the surface of BT NPs helped to uniformly disperse the BT nanoparticles. However, the composites with surface modified fillers showed more homogeneous dispersion than composites made with surfactant. The inset in Fig. 4.12 (b) displays the flexibility of the dielectric nanocomposites, even in a thick (500 μm) sample.

Figure 4.13 (a) shows real permittivity and dielectric loss of PVDF matrix composites with different concentration of commercial BT NPs. As the filler content increased from 0 to 47.01 vol %, the dielectric permittivity gradually increased. At 1 kHz, the dielectric permittivity of pure PVDF was 8.7, which was increased to 76 when the filler content was 47.01 vol %. The increase in dielectric permittivity can be explained by the presence of many nano-capacitors formed by separation of BT NPs with the polymer matrix.[156] As insulating thin polymer layers separated the filler particles, the local electric field across these nano-capacitors increased. As a result, more charge carriers accumulated in the polymer layer and the dielectric permittivity increased. This phenomenon is known as interfacial polarization.[9] The dielectric permittivity was almost constant over the frequency range from 10 Hz to 1 MHz for composites containing < 30 vol % of BT NPs. For higher content of the filler, the low frequency response increased more rapidly because the space charge polarization became more prominent at high filler content.

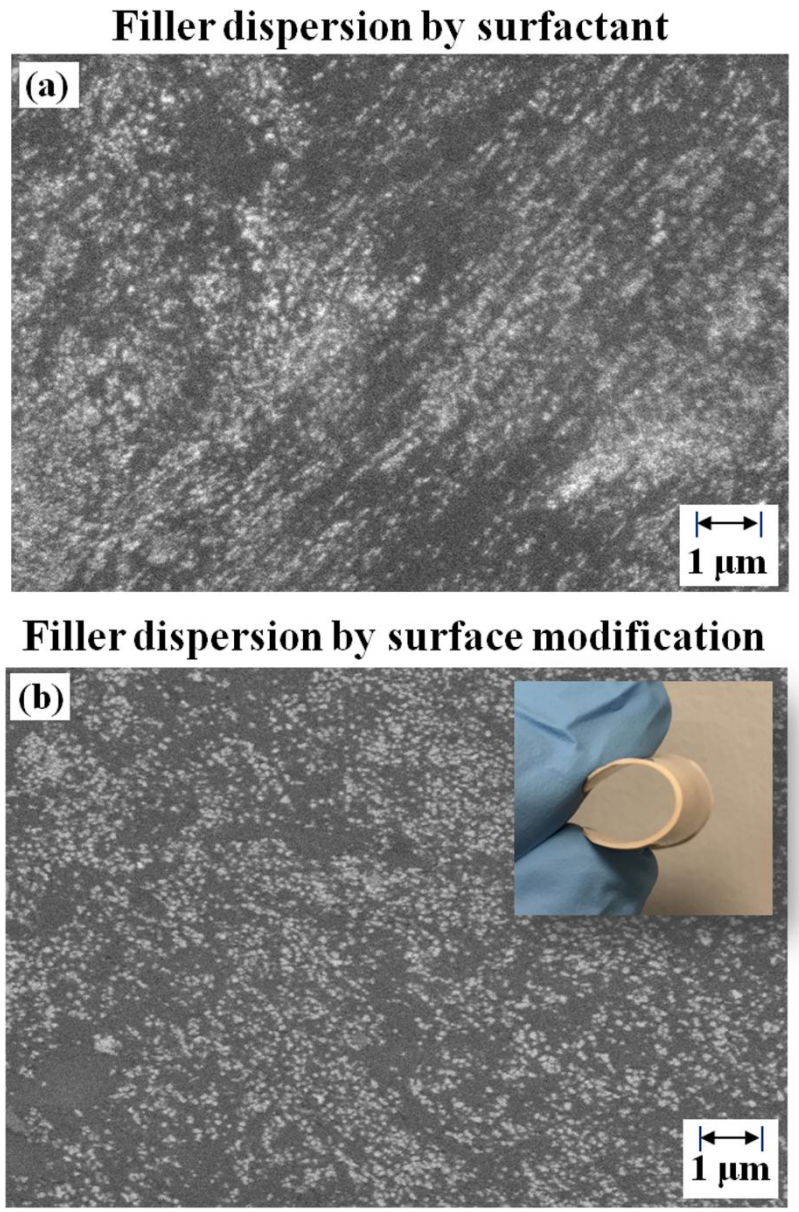

Figure 4.12. SEM images of nanocomposites (a) filler dispersion by surfactant and (b) filler dispersion by surface modification. Inset in (b) shows flexibility of the composite even in a thick (500 μm) sample.[11]

Figure 4.13 (b) shows the dielectric loss of the composites. The dielectric loss is described in terms of loss tangent. This is also known as dissipation factor, because it is the ratio of dissipated to stored electric energy, which is defined as the ratio of the imaginary part to the real part of the permittivity ($\varepsilon''/\varepsilon'$). The dielectric loss of polymer

matrix composites is mainly due to a resonance of the matrix material [157, 158] as evidenced by the reduction in loss tangent as a function of BT at frequencies above 10 kHz as shown in Fig. 4.13(b). However, as the filler concentration increased, the space charge induced dielectric loss increased at lower frequency region. The increase of dielectric loss in the low frequency region is also believed to be related to defects present in the matrix region. The loss tangent of composites remained below 0.1 for all compositions at frequencies from 1 kHz to 1 MHz. This implies that most of the filler nanoparticles were effectively surrounded by insulating polymer matrix. When the filler content was low, the frequency dependence of loss tangent was relatively low, whereas it became more noticeable as the filler content increased. The increase of energy loss at low frequency is unfavorable, because it causes leakage current and eventually reduces the life of the power supply and devices.[159]

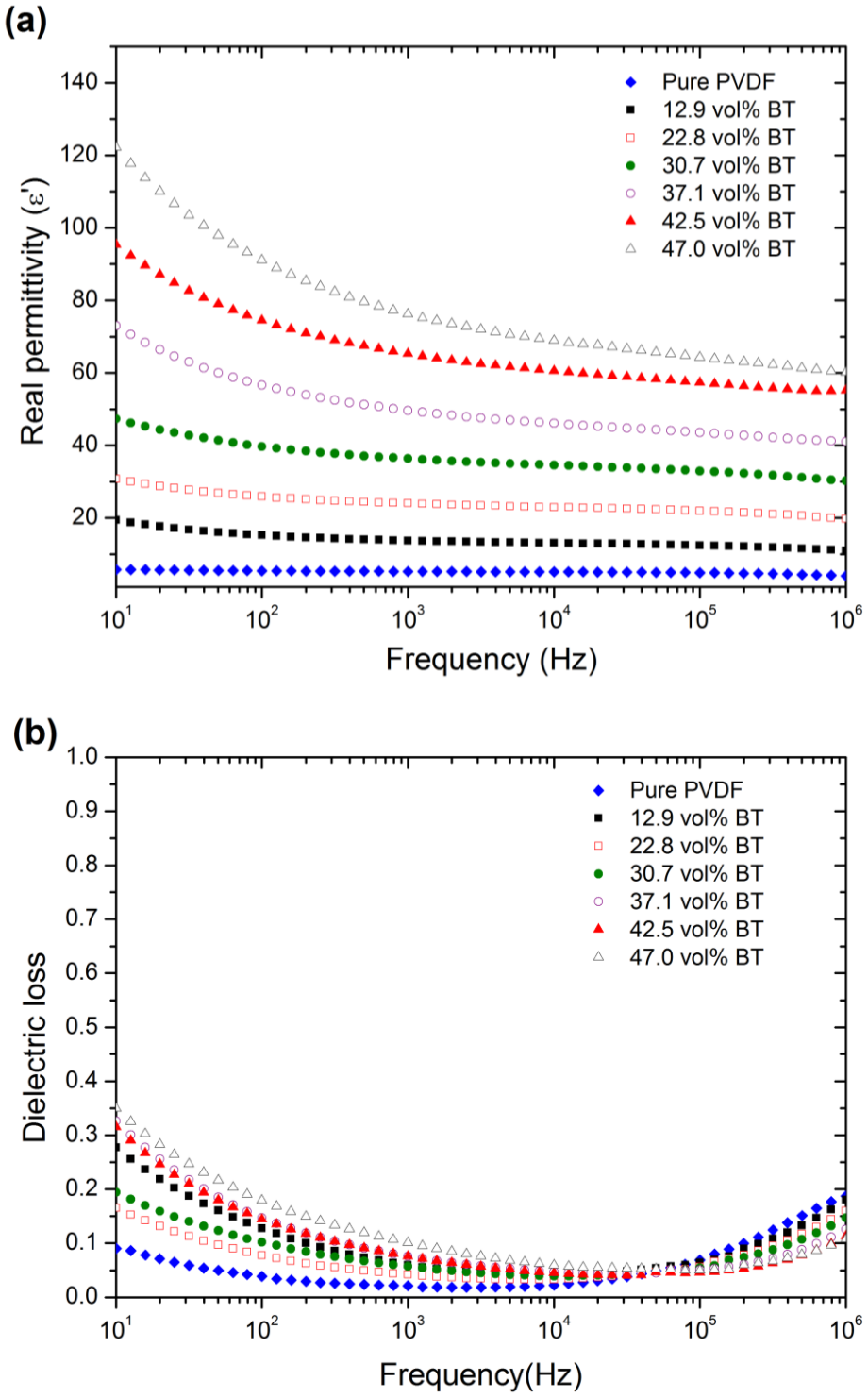

Figure 4.13. (a) Real permittivity and (b) dielectric loss for composites containing different amounts of BT.[11]

4.2.2.2 Effects of Conductive Fillers in Conjunction with High-*k* Fillers

Figure 4.14 shows SEM images of multi-phase nanocomposites containing 37.1 vol % BT and 3 vol % MWCNT. Figure 4.14 (a) shows the top surface of the nanocomposite and Figs. 4.14 (b-d) show the fractured cross sections of the nanocomposites with different magnifications. The BT NPs functionalized with MPS were uniformly dispersed in the polymer matrix. There was no evidence of macroscopic filler agglomeration. The immediate phase separation prevented macroscopic re-agglomeration of nano-fillers. And the surface modification of the fillers helped to prevent sub-microscopic filler agglomeration and improve the interfaces between the matrix and the fillers.

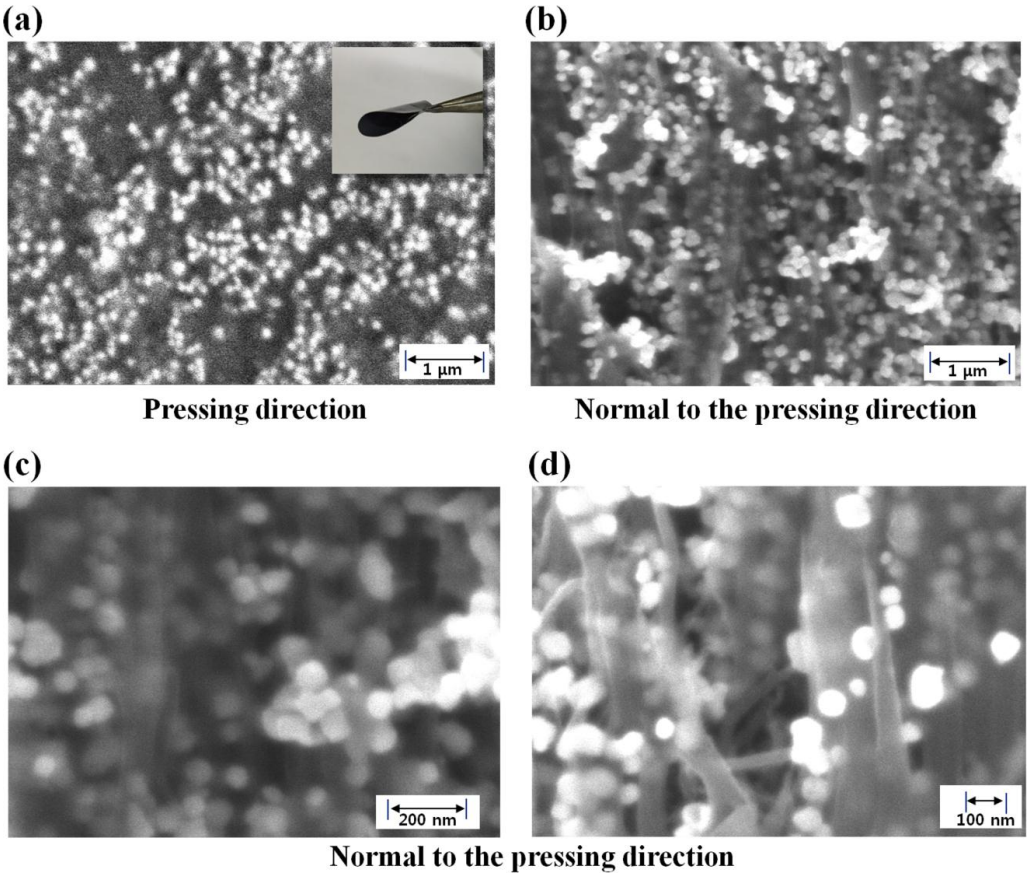

Figure 4.14. SEM images of BT/MWCNT/PVDF hybrid nanocomposites containing 37.1 vol % BT and 3 vol % MWCNT (a) top surface of the nanocomposite (b-d) fractured cross sections of the nanocomposites with different magnifications.[83]

The highly flexible free standing composite thin films were obtained after hot pressing even with the highest concentration of fillers. The presence of MWCNT was detected in Fig. 4.14 (d); however, it was difficult to obtain low magnification images showing MWCNT distribution in the matrix due to the small fraction of MWCNT used.

The frequency dependent real permittivity and dielectric loss of the multi-phase nanocomposites with respect to the MWCNT contents are shown in Fig. 4.15 (a) and (b) respectively. The real permittivity gradually decreased with increasing frequency due to the decreased dipole mobility, which is not sufficiently mobile to displace as the frequency of the applied electric field exceeds the relaxation frequency.[72] At a BT content of 22.8 vol %, the real permittivity was increased from 26.9 to 52.68 at 1 kHz with 4 vol % of MWCNT which is 6 times higher than that of pure PVDF and there was no noticeable increase in dielectric loss (0.049 to 0.055 at 1 kHz) due to the uniformly dispersed BT NPs and MWCNT in the polymer matrix. According to the micro-capacitor model, each two adjacent MWCNTs can be treated as local nano-capacitors with MWCNTs as two electrodes. The permittivity of the nanocomposites can be further increased if the distance between MWCNTs is decreased or the relative permittivity of the matrix region in between MWCNTs is increased.[12] The distance between the adjacent MWCNTs can be decreased by increasing MWCNT content which are effectively separated by the matrix. The improved real permittivity with low loss over a wide range of frequency (10 Hz to 1 MHz) in Fig. 4.15 (a) and (b) can be explained by the induced interfacial polarization due to charge transport effects of uniformly dispersed MWCNT in the matrix. The relative permittivity of the dielectric medium between the adjacent MWCNTs can be increased by using a mixture matrix which consists of the pure polymer and ferroelectric BT NPs.

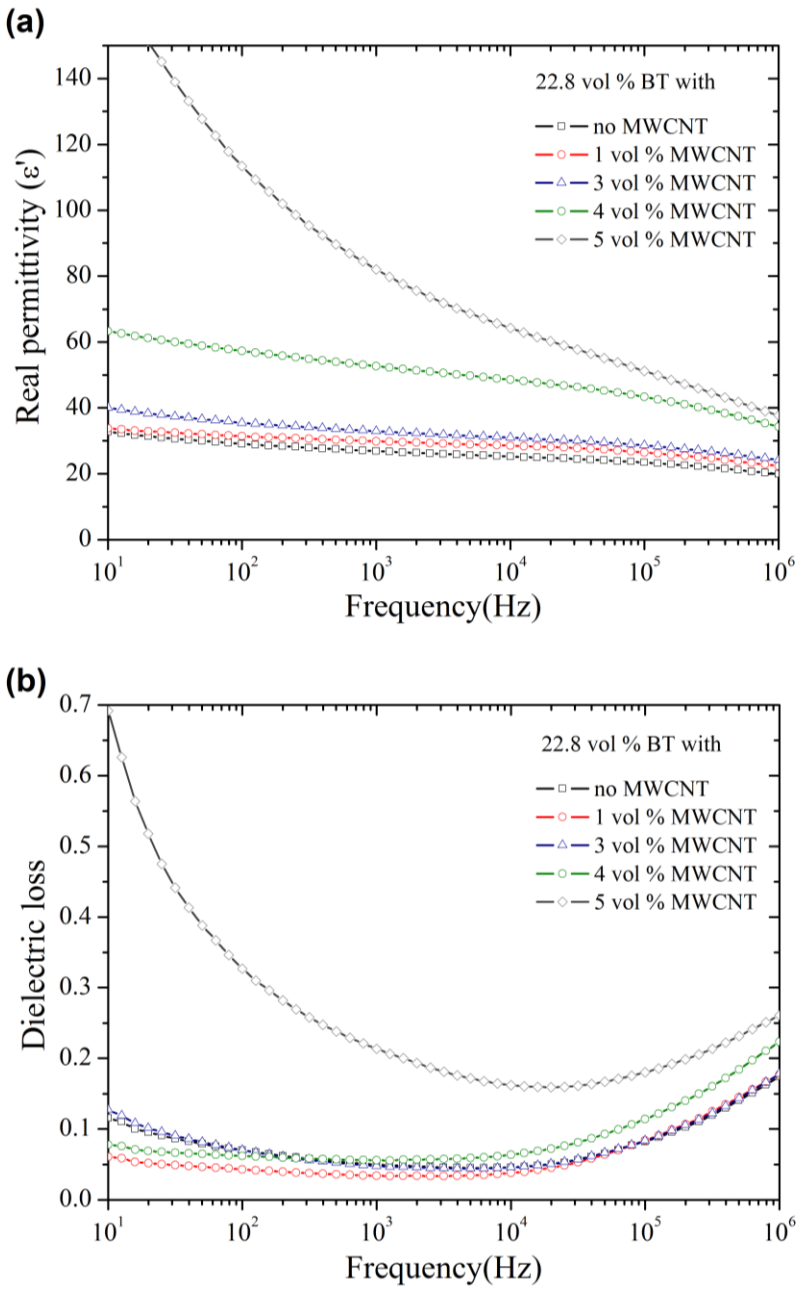

Figure 4.15. (a) Real permittivity and (b) dielectric loss of nanocomposites containing 22.8 vol % BT and MWCNT varying contents of 0 to 5 vol % .[83]

Figure 4.16 (a) and (b) show real permittivity and dielectric loss of the multi-phase nanocomposites with respect to BT contents. At a MWCNT content of 3 vol %, the real permittivity was increased from 36.79 to 71.65 at 1 kHz and the dielectric loss was

even decreased (0.051 to 0.045 at 1 kHz) when the BT content was increased from 22.8 to 37.1 vol %.

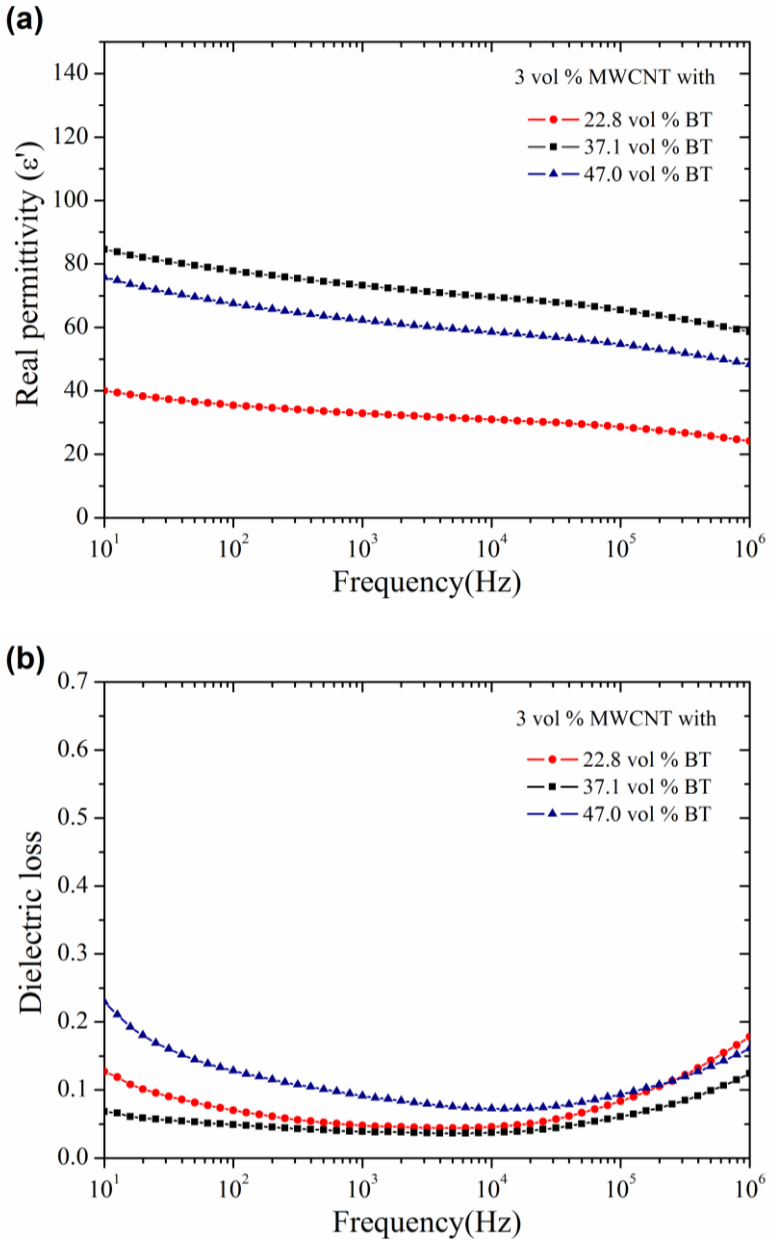

Figure 4.16. (a) Real permittivity and (b) dielectric loss of nanocomposites containing 3 vol % MWCNT and 22.8, 37.1 and 47.0 vol % BT.[83]

The improvement in dielectric properties can be explained by more charge accumulation due to relative permittivity in the mixture matrix. BT NPs, which were effectively dispersed in the polymer matrix, help to separate MWCNT bundles and work as

insulating barriers in between nearby MWCNTs, even when MWCNT is near the percolation threshold. The electrical charges coming from an external electrode will be migrating and accumulating near the interfaces of different phases, due to charge storage effects of the ferroelectric phase (BT NPs) and the charge transport effects of the conductive phase (MWCNT) and different relaxation times of each phase.[102]

Figure 4.17 shows AC conductivity of the multi-phase nanocomposites containing different amounts of BT and MWCNT. At 22.8 vol % BT, the nanocomposites containing 5 vol % MWCNT show frequency independent behavior (i.e. plateau region) at low frequencies while the others show frequency dependent behavior throughout the whole frequency range, which means the onset of the first continuous conductive path of MWCNT. At 37.1 vol % BT, the plateau region becomes wider with 4 vol % MWCNT. The percolation threshold (ρ_c) of MWCNT decreased with increased BT NPs content due to shorter inter-particle distance between BT NPs. The frequency where the transition from frequency dependent to frequency independent regime appears is called the critical frequency (f_c). According to the power law, $\sigma(\omega) \propto \omega^x$, the AC conductivity is exponentially proportional to the frequency above the critical frequency.[6, 30] It is obvious that the composites containing 22.8 vol % of BT with less than 5 vol % of MWCNT and the composites containing 37.1 vol % of BT with less than 4 vol % of MWCNT are highly insulating.

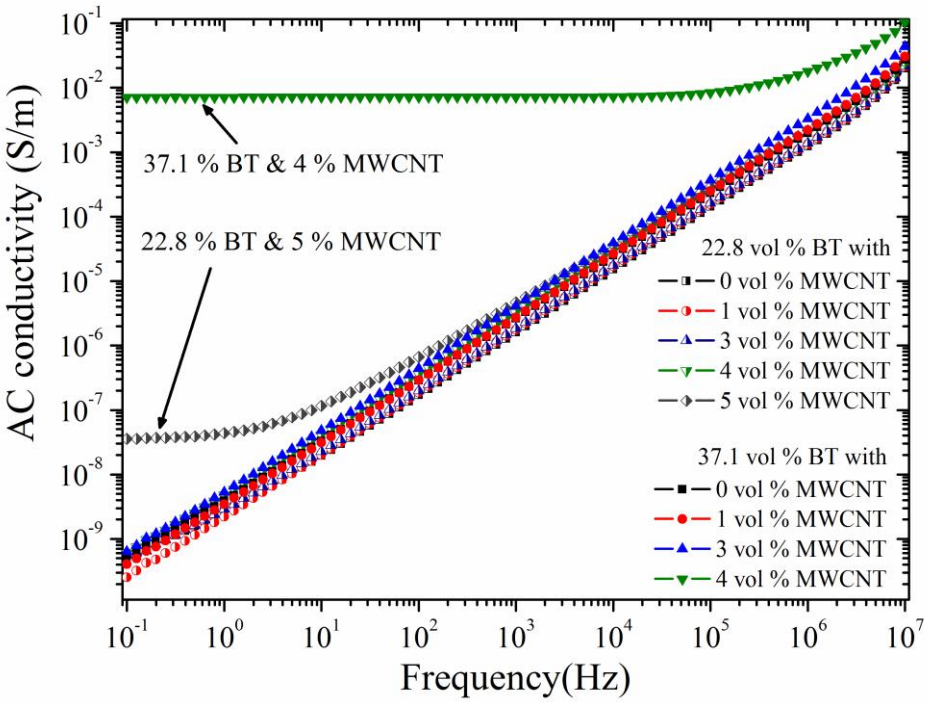

Figure 4.17. AC conductivity of nanocomposites containing 22.8 vol % BT and 0 to 5 vol % MWCNT as well as samples containing 37.1 vol % BT and 0 to 4 vol % MWCNT.[83]

Figure 4.18 shows steady state dielectric properties of multi-phase nanocomposites at 1 kHz as a function of MWCNT content. The real permittivity of the nanocomposites was substantially improved as the MWCNT content increased. At 22.8 vol % BT, the real permittivity increased from 26.9 for 0 % MWCNT to 78.4 for 5 vol% MWCNT. However, the composite sample containing 5 vol % MWCNT also showed relatively high dielectric loss up to 0.2, which is due to the onset of percolation network of MWCNT as has been shown in Fig. 4.17.

Polymer matrix dielectric nanocomposites containing conductive 0D/1D/2D fillers usually show narrow adjustable windows near the percolation threshold where dielectric properties can be improved.[102] The adjustable window in the BT/MWCNT/PVDF nanocomposites was in between 1-4 vol % of MWCNT with 37.1

vol % BT or less. The dielectric loss of multi-phase nanocomposites was very low (< 0.05) in the adjustable window, which illustrates the effective dispersion of the MWCNT before the onset of the conductive percolation network. At BT content 47.0 vol % or higher, the dielectric permittivity decreased with increasing MWCNT content in the adjustable window. The induced interfacial charge polarization near BT NPs was decreased due to high concentration of fillers. This can be explained by the pores formed at higher filler loading, local bundling of MWCNT and neutralization of the relaxation time difference between the phases due to physical contacts between the BT and MWCNT.

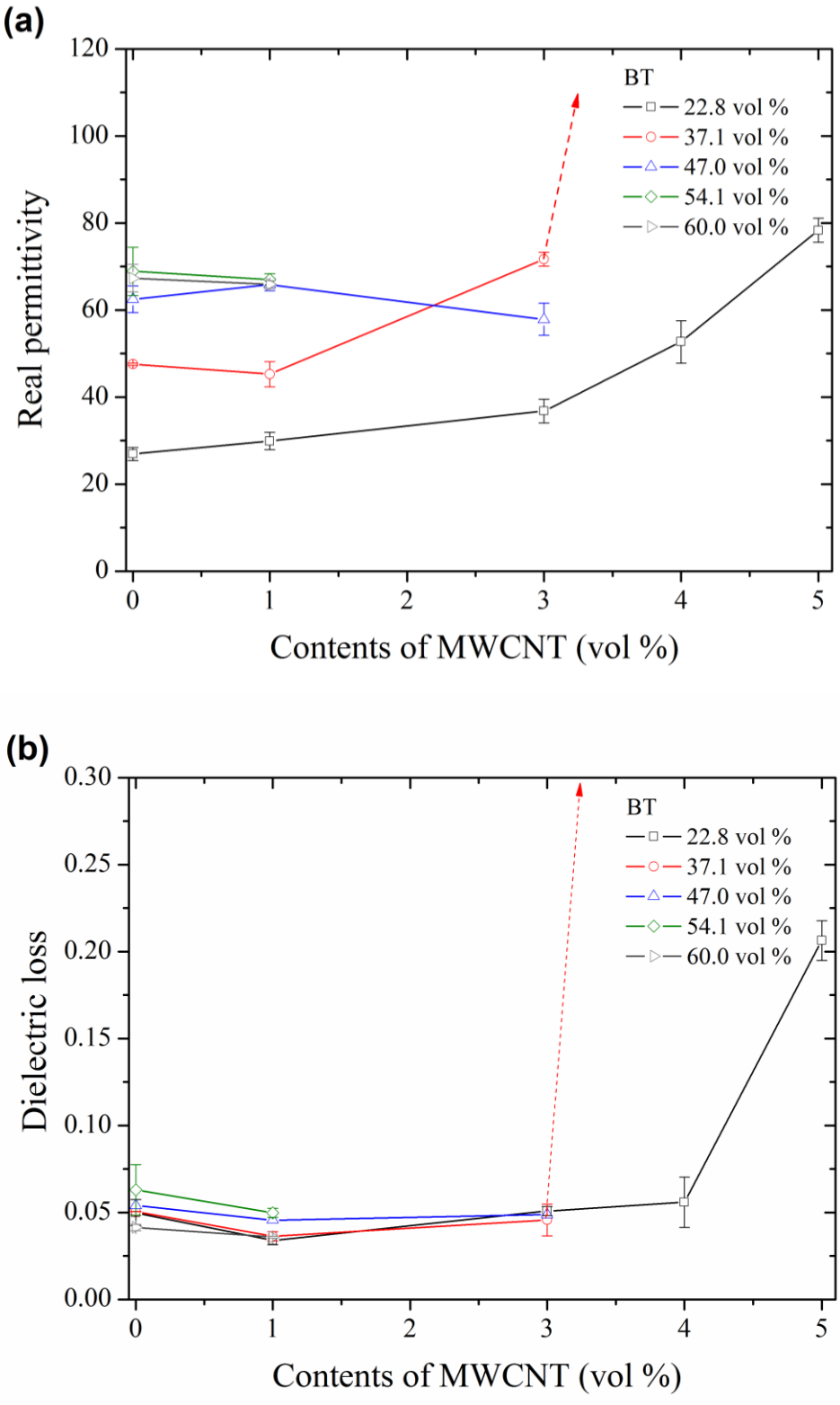

Figure 4.18. Steady state dielectric properties of nanocomposites at 1 kHz (a) real permittivity and (b) dielectric loss.[83]

4.2.2.3 Effects of Particle Size of High-*k* Fillers

Figure 4.19 (a) shows the real permittivity of polymer matrix nanocomposites containing 37.1 vol % of surface modified BT with different sizes. As a general trend, the real permittivity of the BT/PVDF nanocomposite gradually decreases with increasing frequency from 1 Hz to 1 MHz. Although, the real permittivity showed similar frequency dependence, there was a significant difference in the real permittivity values between the nanocomposite containing BT NPs with different sizes. According to the phenomenological theory,[93, 160] ferroelectricity decreases remarkably with decreasing grain size, and the ferroelectricity of BT nanoparticles would disappear when the grain size drops to about 44 nm. Similar trends have been reported by other researchers.[93, 95] In this study, the synthesis conditions to make BT nanoparticles of different size were maintained identical to show the filler size dependent dielectric properties under the same surface conditions of BT nanoparticles, because the dielectric properties of polymer matrix nanocomposites containing ferroelectric fillers can be highly affected by surface conditions of filler NPs as well as interfaces between the matrix and the fillers. Note that Fig. 4.19 and Fig. 4.20 contain the results from commercial BT (78 nm), which were included because they fit nicely with the trends obtained from the synthesized BT NPs. Figure 4.19 (b) shows the dielectric loss of polymer matrix nanocomposites containing 37.1 vol % of surface modified BT with different sizes. It was observed that the dielectric loss was very low for a wide range of frequencies. In general, dielectric loss of nanocomposites with synthesized BT showed lower values than that of nanocomposites with commercial BT at all frequencies. It is believed that the compatibility between the matrix and the fillers was better in the nanocomposites made with the synthesized BT NPs.

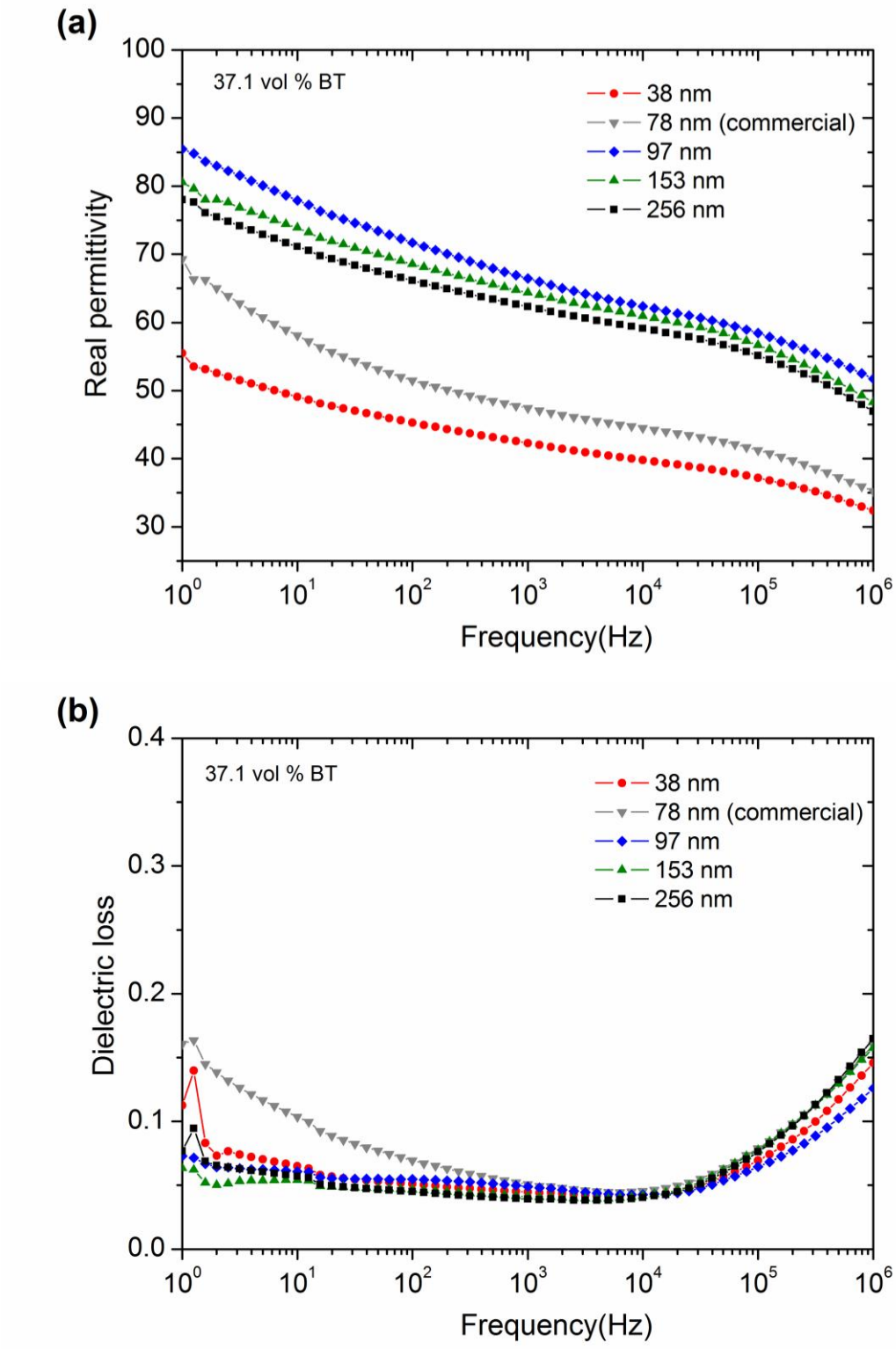

Figure 4.19. (a) Real permittivity and (b) dielectric loss of nanocomposites containing 37.1 vol % BT synthesized with different sizes (78 nm BT was commercially obtained).

Figure 4.20 shows steady state dielectric properties of nanocomposites containing 37.1 vol % of BT as a function of BT particle size. The real permittivity exhibited the highest value when the BT particle size was 97 nm and exhibited the lowest value when the BT size was 38 nm. At 1 kHz, the maximum value of real permittivity was 65.9 and the minimum value was 38.6. The synthesized BT with particle size above 97 nm showed similar results, but the real permittivity values gradually decreased with BT size as shown in Fig. 4.20. The lowest real permittivity of composites that was obtained with synthesized BT (38 nm) can be explained by the decreased ferroelectricity due to the smaller particle size.[93] In general, the real permittivity sharply increased with BT size until 100 nm, and gradually decreased as BT size further increased as shown in Fig. 4.20 (a). There was no noticeable size dependence of dielectric loss of nanocomposites containing synthesized BT (Fig. 4.20 (b)). Dielectric loss values kept below 0.05 at frequencies below 10 kHz. The increased dielectric loss above 10 kHz is mainly due to a small resonance of the matrix polymer as described above.

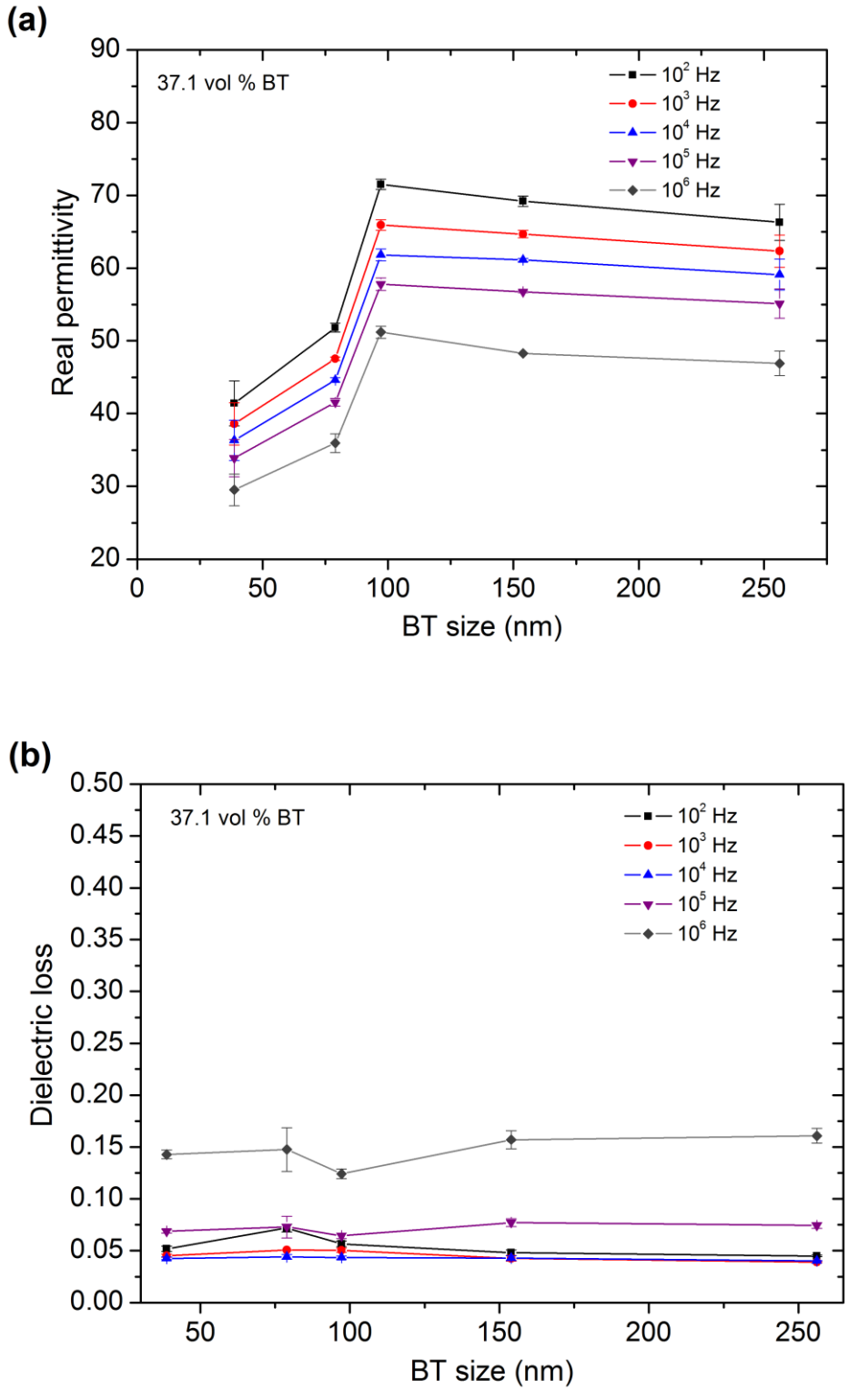

Figure 4.20. Steady state dielectric properties of nanocomposites at 100-1MHz as a function of particle size (a) real permittivity (b) dielectric loss.

4.2.2.4 Breakdown Strength and Energy Density of the Dielectric PMCs

Figure 4.21 (a) shows the breakdown strength of the pure PVDF, PVDF-HFP and the nanocomposites containing 37.1 vol % of BT and 1 to 3 vol % of MWCNT. The breakdown strength of the pure PVDF was increased from 260.3 V/μm to 308.5 V/μm after annealing and quenching, while that of PVDF-HFP was increased from 294.0 to 438.5 V/μm. The annealing followed by quenching was more effective for PVDF-HFP, as was expected from the FTIR and DSC results. The energy density can be enhanced more in the PVDF-HFP matrix nanocomposites than in the PVDF matrix nanocomposites, because the former showed higher breakdown strength, while the real permittivity and the dielectric loss showed approximately the same properties within the error bars. The breakdown strength of PVDF-HFP matrix hybrid nanocomposites increased from 232.72 to 272.43 V/μm and 199.0 to 251.1 V/μm for BT contents of 37.1 vol % with 1 vol % and 3 vol % MWCNT respectively. The breakdown strength gradually decreased as the BT filler content increased, due to increased defects, more interfacial polarization, which can adversely affect the breakdown strength; and more joule heating along the MWCNT at breakdown. Figure 4.21 (b) shows calculated energy density of some hybrid nanocomposites based on the measured real permittivity and the measured breakdown strength values. The energy density of the PVDF-HFP matrix nanocomposites containing 37.1 vol % of BT and 3 vol % of MWCNT was 19.82 J/cm^3 at 250 V/um.

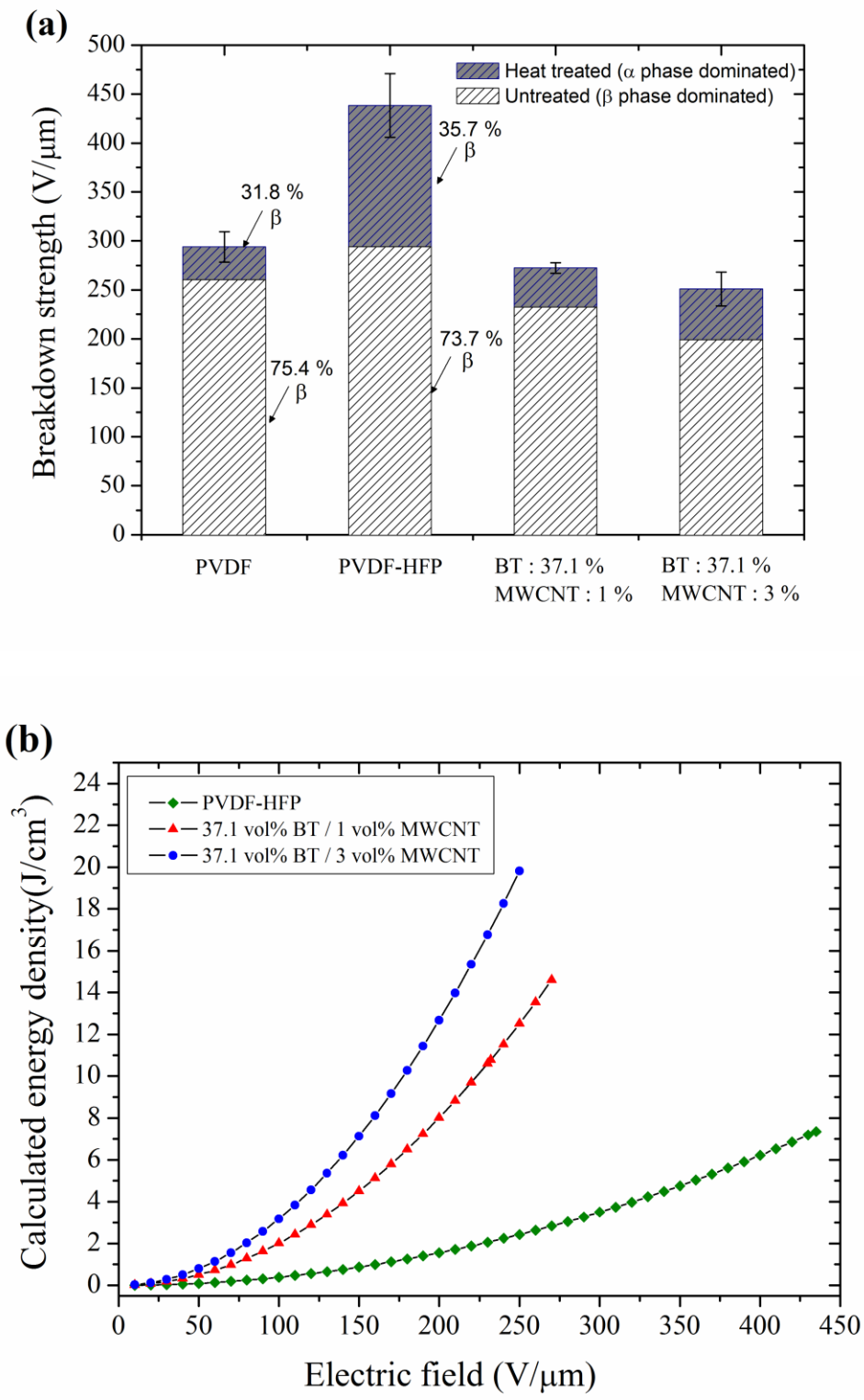

Figure 4.21. (a) Breakdown strength of heat treated (grey) and untreated (white) pure PVDF, PVDF-HFP and nanocomposites containing 37.1 vol % BT and 1 to 3 vol % MWCNT. (b) Calculated energy density.[83]

Table 4.1 shows a comparison of previously reported dielectric properties of polymer matrix composites. In general, dielectric properties are based on compromise. It is very difficult to make a composite material with high real permittivity, low dielectric loss and high breakdown strength at the same time. Polymer composites with high breakdown strength often have low values of real permittivity, thus higher electric field is required to store more electric energy. And polymer composites with high real permittivity normally have low breakdown strength, which limits their use in the higher operating electric fields. In this work, polymer matrix composites with hybrid fillers demonstrated that they can have a good combination of real permittivity, dielectric loss and breakdown strength.

Table 4.1: Dielectric properties of reported polymer matrix composites

Matrix	Filler (vol %)	Real permittivity at 1 kHz	Dielectric loss at 1 kHz	B.D. (V/μm)	Energy density / electric field (V/μm)	Ref.
PVDF-HFP	BT(37.1) / MWCNT(3)	71.6	0.04	251	19.8 [b] (251)	Present work
PVDF	BT NP (20)	20.2	0.04	> 250	3.54 (250)	[87]
PVDF	BT@SiO_2 NW (2.5)	-	-	> 330	6.28 (330)	[161]
PVDF	CCTO NP (55)	77.5	0.11	-	-	[68]
PMMA	BT@HBP [a]	39.3	0.03	-	0.03 (12)	[69]
PVDF-HFP	BT NW (10)	25	-	100±36	-	[70]
PVDF-HFP	BST NW (7.5)	14.9	0.03	118	0.05 (20)	[162]
PVDF-HFP	BT@TO (3)	19	0.05	797	31.2 (797)	[51]
PVDF-CTFE	BT NP (50)	37	0.07	210±50	6.1 [b] (210)	[82]
PVDF-TrFE-CFE	BT NW (17.5)	69.5	0.09	> 300	10.48 (300)	[99]

a) composite fabricated by in-situ polymerization (HBP : Hyperbranched Aromatic Polyamide)
b) calculated energy density from measured real permittivity and breakdown strength

4.2.2.5 Equivalent Circuit Fitting for Dielectric Responses of the Dielectric PMCs

It is customary to analyze the measured impedance using possible equivalent circuit components to evaluate the responses obtained. In this way, one can have a better idea as to how the conductive and the ferroelectric fillers affect the charge accumulation in a polymer matrix hybrid composite system. Impedance spectroscopy is widely used to investigate the charge transport and accumulation in a given microstructure. Although there have been studies on the equivalent circuit fitting of the BT/MWCNT/PVDF nanocomposites,[147] the quantitative understanding of the relationship between microstructure and electrical responses requires a comprehensive analysis in all four different dielectric functions (impedance, Z^*, admittance, Y^*, electric modulus, M^*, and permittivity, ε^*), because polarization or conduction processes may not be detectable when using only one formalism.[127, 129] Most dielectric materials can be represented by a parallel RC circuit. And interfacial polarization in between heterogeneous phases can be described by a modified Debye circuit. Thus, the equivalent circuit of BT/MWCNT/PVDF hybrid nanocomposite is represented as a modified Debye circuit in series with a parallel RC circuit. If the percolation network of MWCNT is formed, an inductive element has to be added due to the intrinsic electrical properties of MWCNT.[147, 163] The constant phase elements (CPE), which can describe slight deviations from a perfect capacitor response, was used in the equivalent circuit fitting. A CPE can be expressed by the following equation.

$$Z = 1/\left[Y_0(i\omega)^{\alpha}\right] \quad (4)$$

where the Y_0 is the constant in the units of Farads (F) and α is the CPE power index ($0 \leq \alpha \leq 1$); if α is 1, Y_0 works as a perfect capacitor.

The simulated values of the equivalent circuit elements are listed in table 4.2. Data shown in table 4.2 are averaged values of at least 3 samples at each filler content. The effective permittivity of the hybrid nanocomposites was highly related to the interfacial polarization, which is represented by the high frequency capacitance in the modified Debye circuit (CPE1). The Y_0 values of the high frequency capacitance (CPE1) increased as the filler content increased illustrating the combined effects of the charge storage effects of the ferroelectric BT NPs and the charge transport effects of the conductive MWCNT.

Table 4.2: Simulated values of the equivalent circuit elements. (obtained from the average)

BT/CNT (vol %)	Interfacial Resistance (R1 (Ω))	High *f* capacitance (CPE1)		Low *f* capacitance (CPE2)		Filler resistance (R2 (Ω))	Filler capacitance (CPE3)	
		Y_0 (F)	α	Y_0 (F)	α		Y_0 (F)	α
22.8 / 1	1.38×10^{9}	1.60×10^{-11}	0.99	5.57×10^{-12}	0.64	8.67×10^{11}	3.27×10^{-8}	0.59
37.1 / 1	8.50×10^{8}	2.26×10^{-11}	0.99	6.95×10^{-12}	0.64	1.16×10^{12}	9.78×10^{-8}	0.54
47.0 / 1	4.77×10^{8}	3.23×10^{-11}	0.98	2.10×10^{-11}	0.57	1.12×10^{12}	1.10×10^{-6}	0.46
22.8 / 3	7.74×10^{8}	1.91×10^{-11}	0.98	2.70×10^{-11}	0.47	8.23×10^{11}	2.39×10^{-7}	0.51
37.1 / 3	4.94×10^{8}	3.83×10^{-11}	0.98	1.28×10^{-11}	0.65	1.13×10^{12}	4.80×10^{-7}	0.51
47.0 / 3	2.97×10^{8}	3.22×10^{-11}	0.98	5.67×10^{-11}	0.51	1.27×10^{12}	5.00×10^{-7}	0.50

The values of α of the CPE1 are close to 1, representing Y_0 work as a perfect capacitor. The interfacial resistance (R1) decreased with the increased filler content since the local conductivity increased with the filler content. In this circuit model, R1 does not represent the overall resistance of the composites, which was several orders of magnitude larger than R1. The low frequency capacitance (CPE2) represents space charge polarization of the nanocomposites. It is believed that the CPE2 is related to the defects such as micro-voids and micro-cracks and the local agglomeration of the fillers in the polymer matrix. The real permittivity became more frequency dependent at the low frequency region as

the values of Y_0 in the CPE2 increased (Fig. 4.16). The much larger values of Y_0 in the CPE3 are related to the intrinsic capacitance of the fillers. However, the effective permittivity of the polymer matrix nanocomposites is more related to the average increase of the field in the matrix region rather than the intrinsic properties of the fillers.

Figure 4.22 shows equivalent circuit fitting of a composite containing 37.1 vol % BT and 3 vol % MWCNT in the impedance complex plot (a), permittivity complex plot (b), real permittivity (c) and dielectric loss (d). The measured data were fitted well with the equivalent circuit model in all four functions. Figure 4.23 shows the equivalent circuit fitting for the other dielectric functions. It is important to do this so that physical assignment to each circuit element can be made more easily and take all parameters into account.

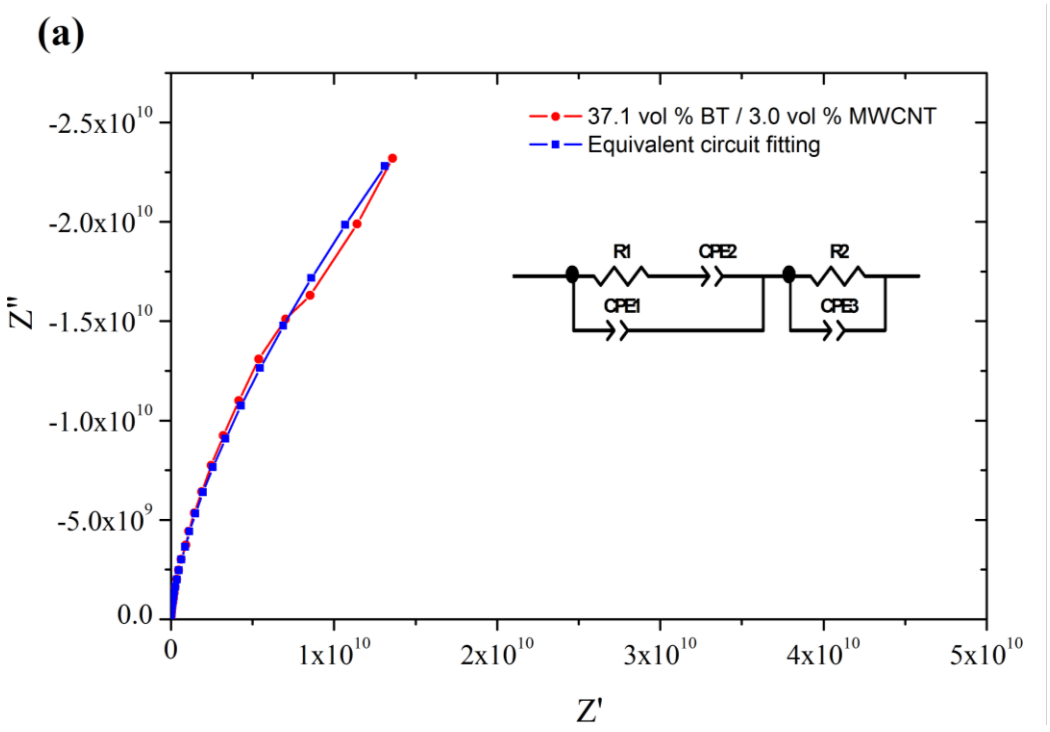
(a)
37.1 vol % BT / 3.0 vol % MWCNT
Equivalent circuit fitting
R1
CPE2
R2
CPE1
CPE3
-2.5x10^10
-2.0x10^10
-1.5x10^10
-1.0x10^10
-5.0x10^9
0.0
Z''
0
1x10^10
2x10^10
3x10^10
4x10^10
5x10^10
Z'

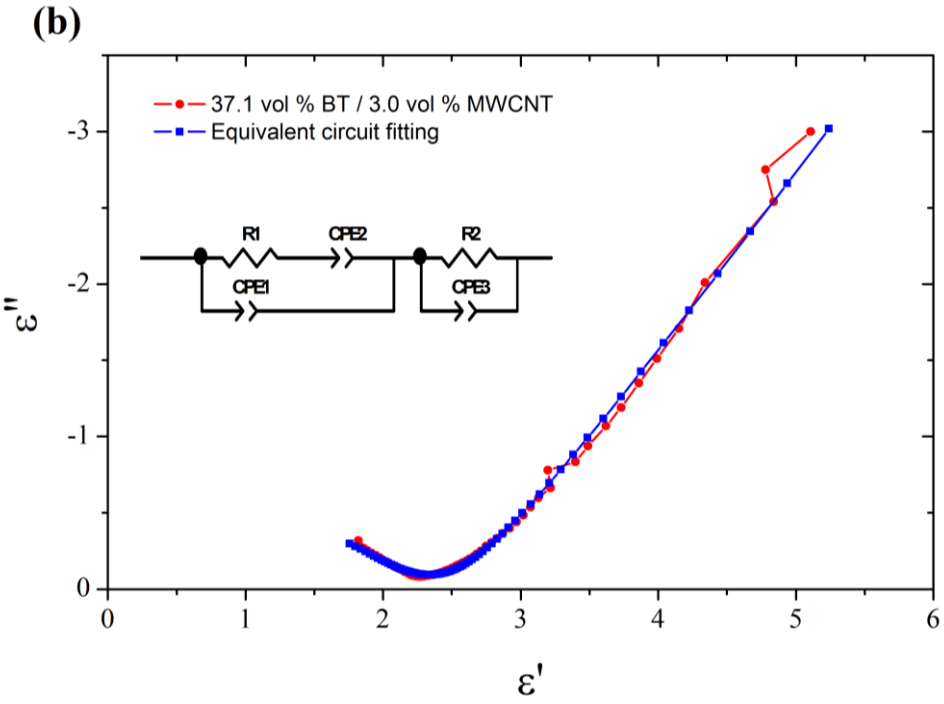
(b)
37.1 vol % BT / 3.0 vol % MWCNT
Equivalent circuit fitting
R1
CPE2
R2
CPE1
CPE3
-3
-2
-1
0
ε''
0
1
2
3
4
5
6
ε'

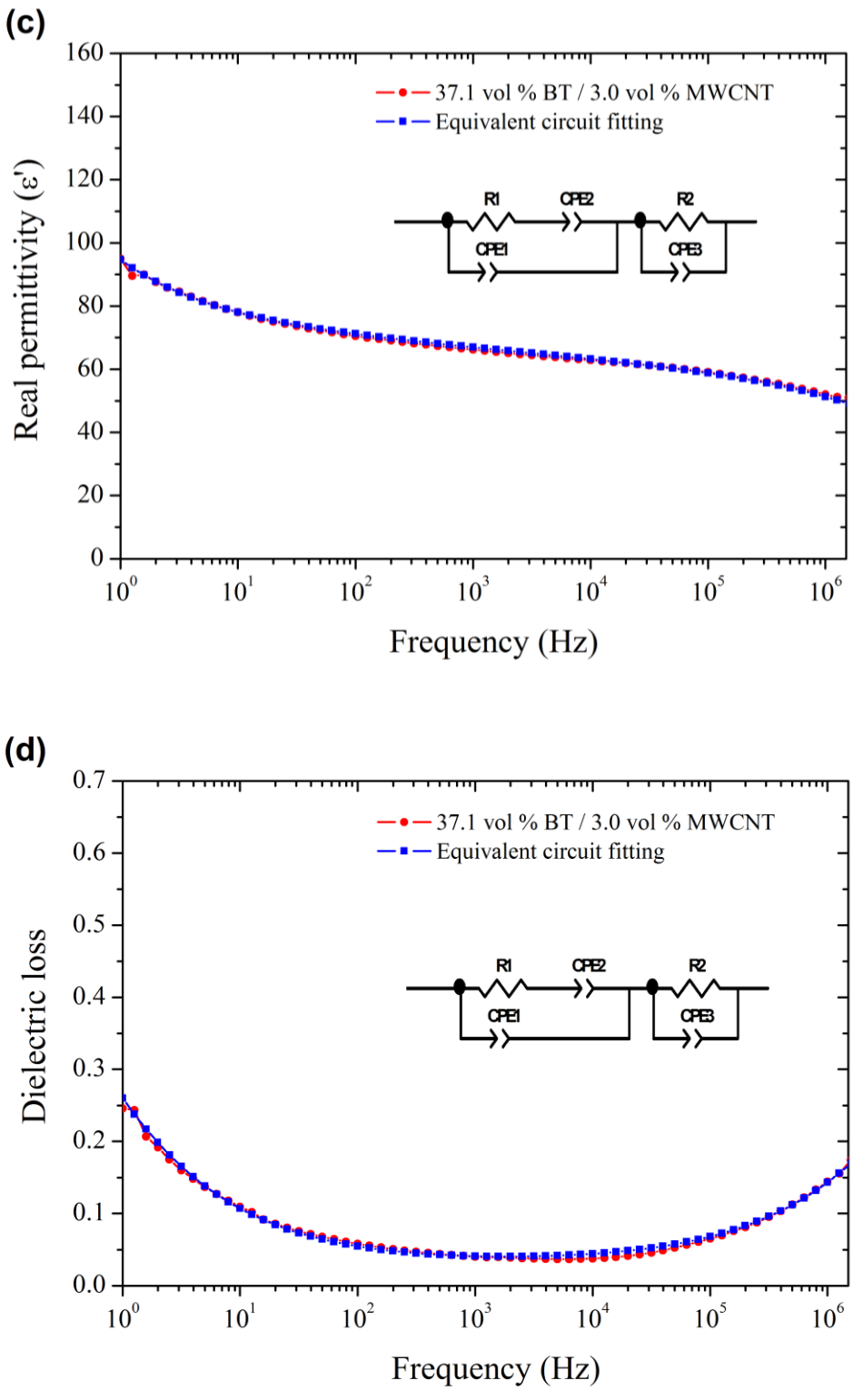

Figure 4.22. Equivalent circuit fitting of a composite containing 37.1 vol % BT and 3 vol % MWCNT (a) impedance complex plot, (b) permittivity complex plot, (c) real permittivity and (d) dielectric loss.

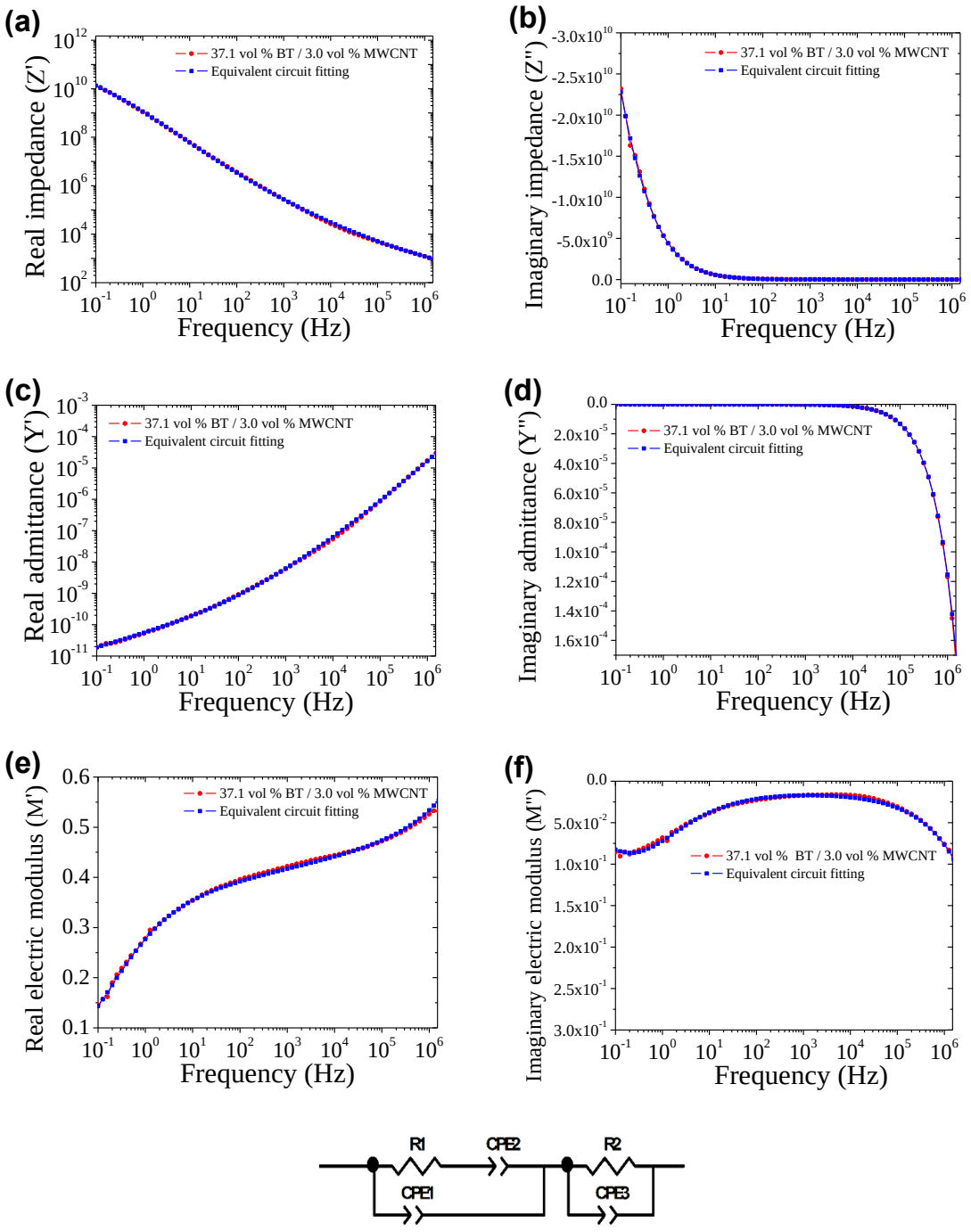

Figure 4.23. Additional equivalent circuit fitted curves for the same composite containing 37.1 vol % BT and 3 vol % MWCNT displayed in Fig. 4.22 (a) real impedance, (b) imaginary impedance (c) real admittance, (d) imaginary admittance, (e) real electric modulus and (f) imaginary electric modulus plots.[83]

4.2.3 Finite Element Modeling of Dielectric Behavior of the Dielectric PMCs

Dielectric polarization and relaxation mechanisms in polymer matrix nanocomposites, with respect to charge storage effects of the ferroelectric phase and the charge transport effects of the conductive phase, were studied by finite element analysis. In the case of impedance measurements, the potential/current is time varying and usually harmonic. Impedance measurement setups involve small length scales (orders of mm) and low frequencies (mHz-MHz range). Hence, the electric field wavelength is typically several orders of magnitude larger than the dimensions of the sample that is measured. In such a situation, the quasi-static approximation can be used.[141]

4.2.3.1 Modeling Overview

The numerical simulations were performed in the frequency domain using the AC/DC module of COMSOL Multiphysics® Version 5.2. The objective was to solve the quasi-static form of Maxwell's equations for the electric potential in the 3D geometry. Figure 4.24 shows schematics of simulation configuration and geometry of a composite containing 47.9 vol % BT NPs. A parallel plate capacitor geometry was used to calculate impedance responses between the port and the ground electrodes.

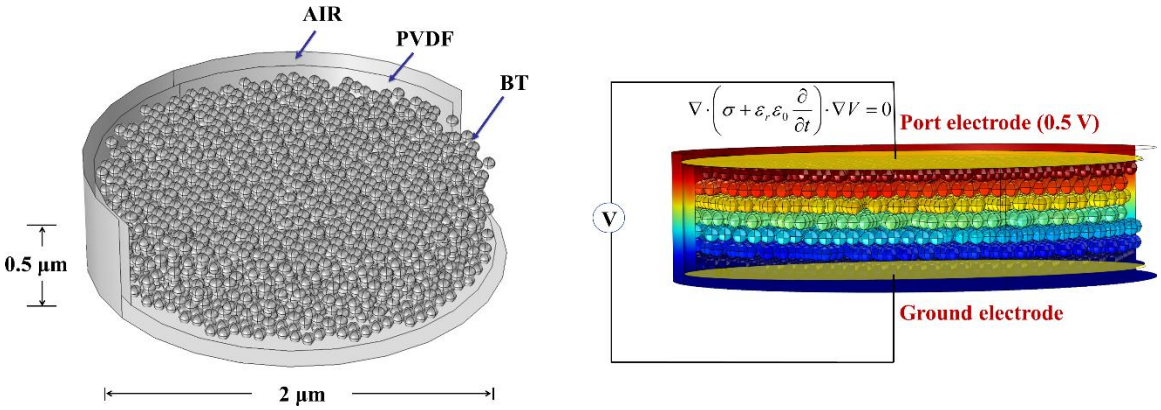

Figure 4.24. Schematic of the configuration for dielectric simulation of a composite containing 47.9 vol % BT.[83]

4.2.3.2 Dielectric Responses from Interactions of Fillers

The interaction between fillers is more important at higher concentration of fillers, because the inter-particle distance is decreased. Moreover, the induced electrical field from the distribution of dipole moments is no longer negligible when calculating overall field locally experienced in the matrix.[5] Figure 4.25 (a) shows the effects of inter-particle distance of nanoparticles on the electric displacement field. The electric displacement in between 2 adjacent nanoparticles increased by more than 200 % as the inter-particle distance decreased from 60 nm to 10 nm when the particle size was 78 nm. A schematic in Fig. 4.25 (b) shows that the interaction zone becomes stronger as the inter-particle distance decreases, in other words, filler concentration increases.[5]

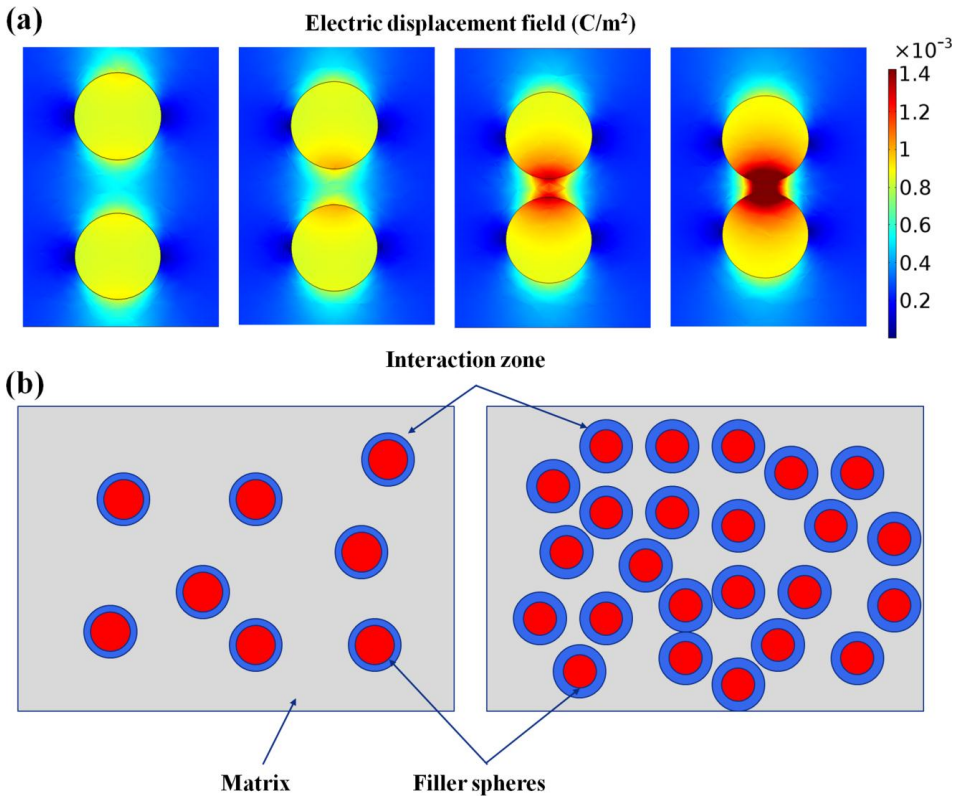

Figure 4.25. (a) Simulation of the effects of inter-particle distance in electric displacement field in between BT NPs (60, 40, 20, and 10 nm from the left) and (b) schematic of interaction zone with respect to inter-particle distance (image modified from reference.[5])

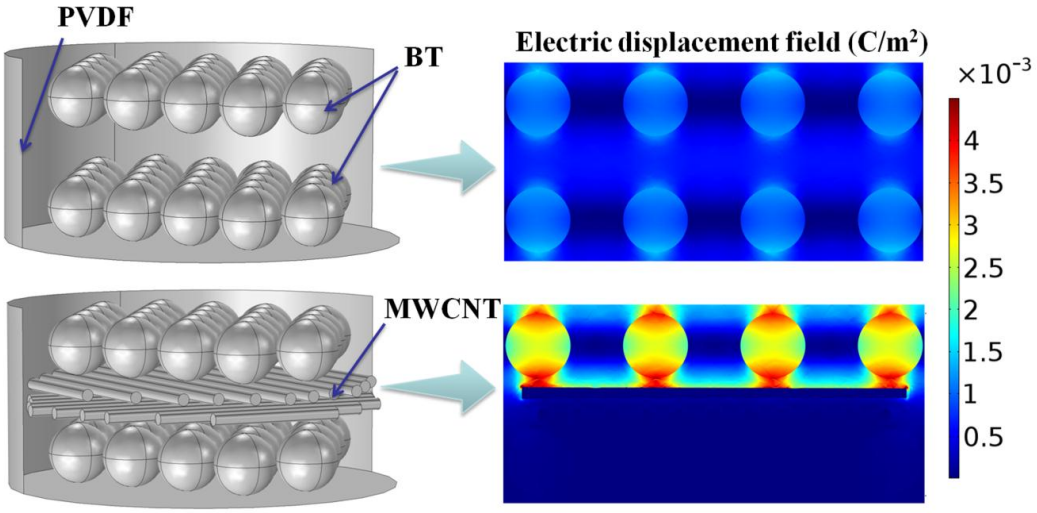

Figure 4.26. Cross-sectional electric displacements field maps of composites containing 22.8 vol % BT and 0 to 3 vol % MWCNT.

The interactions between the ferroelectric filler and the conductive filler were also simulated. Figure 4.26 shows simulated electric displacement field maps for the nanocomposites containing only BT NPs and BT NPs with MWCNT. Perfect alignment of MWCNT perpendicular to the electric field vector and a repeating geometry was assumed. The electric displacement field between adjacent BT NPs was increased by up to 5 times with the presence of effectively separated MWCNT.

Table 4.3 shows the comparison between the FE simulation and the experiments for some multi-phase nanocomposites. The simulated permittivity for the composite containing 22.8 vol % BT and 3 vol % MWCNT was slightly higher than the experimental value, since in the simulation, the MWCNTs were assumed to be perfectly aligned parallel to the electrodes.

Table 4.3: Comparison of real permittivity at 1kHz between finite element analysis and experiments

Composite composition	FEA	Experiments
22.8 % BT	26.4	26.9 ± 1.5
22.8 % BT + 3 % MWCNT	44.3	36.8 ± 2.7

4.2.3.3 Dielectric Responses as a Function of Concentration of Fillers

Figure 4.27 shows FEA modeling geometry for different BT concentrations with minimum inter-particle distance of 10 nm. BT NPs were randomly distributed in the matrix at a desired volume fraction. Figure 4.28 shows the experimental and FEA simulated real permittivity of composites as a function of BT content and calculated values using some existing numerical models. When the filler concentration was less than 20 vol %, the simulation results without interaction field can predict the overall dielectric property well; however, at filler concentration above 20 vol %, the simulation results were lower than the experimental values. The FEA model needed to be modified to better predict the effective permittivity of composites.

The Maxwell-Garnett model, which is based on mean field theory predicted the lowest effective permittivity.[58] Another mean field theory, known as the Bruggeman model can predict more sharply increased effective permittivity for the filler volume fraction above 20 % as was previously reported.[12] Among the existing numerical models, Jaysundere-Smith (J-S) model reasonably predicted the experimental real permittivity obtained from the PVDF/BT nanocomposites. In the J-S model, an additional electric field was introduced as follows :[61]

$$E_{Interaction} = \frac{3\varepsilon_1}{\varepsilon_2 + 2\varepsilon_1} \frac{\varepsilon_2 - \varepsilon_1}{\varepsilon_2 + 2\varepsilon_1} 2 f_2 E_0 \qquad (4.5)$$

where ε_1 and ε_2 are the permittivities of the matrix and the filler respectively, f_2 is the fraction of filler, E_0 is the initial electric field. However, it is only applicable to isolated spherical dielectric fillers. A realistic geometry-based simulation was needed to account for the complexities in the morphology and arrangements of fillers and composition of such components. The FEA model was modified with an additional interaction field for better predictability.

Figure 4.28 shows that there was good agreement between the experimental and the simulation results (note that there was no more physical space in the matrix beyond 47 % of the BT filler to include more fillers when the distance between the fillers is 10 nm). The simulation results with an additional interacting electric filed component for isolated filler NPs, which was proposed by Jaysundere and Smith,[61] showed better prediction of experimental data as expected. The geometry based FEA simulations combined with equivalent circuit analysis can be used to predict and to analyze dielectric properties of polymer matrix dielectric nanocomposites.

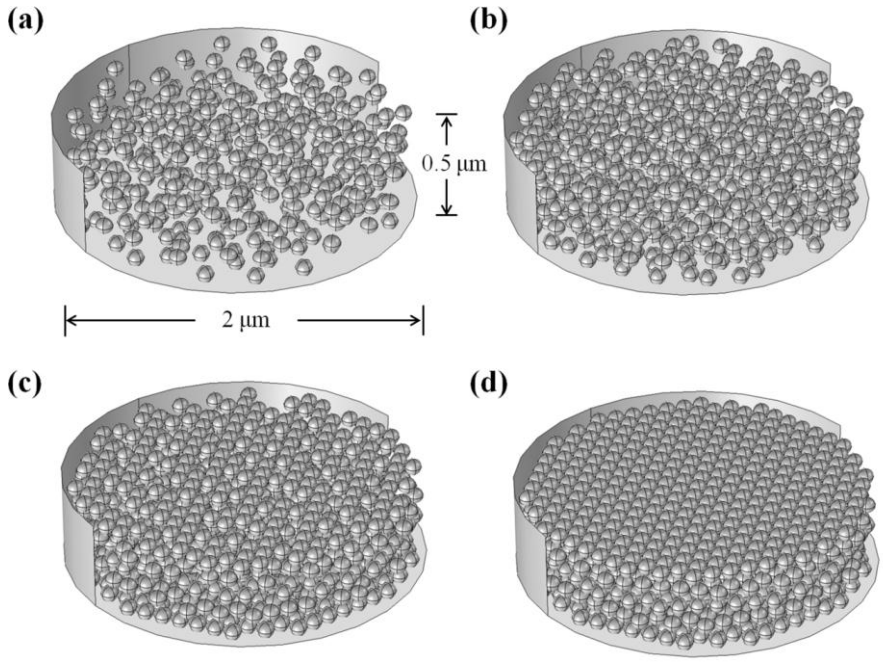

Figure 4.27. FEA modeling geometry for different BT concentrations with minimum inter-particle distance of 10 nm; (a) 10 vol % BT, (b) 20 vol % BT, (c) 30 vol % BT, and (d) 40 vol % BT. [83]

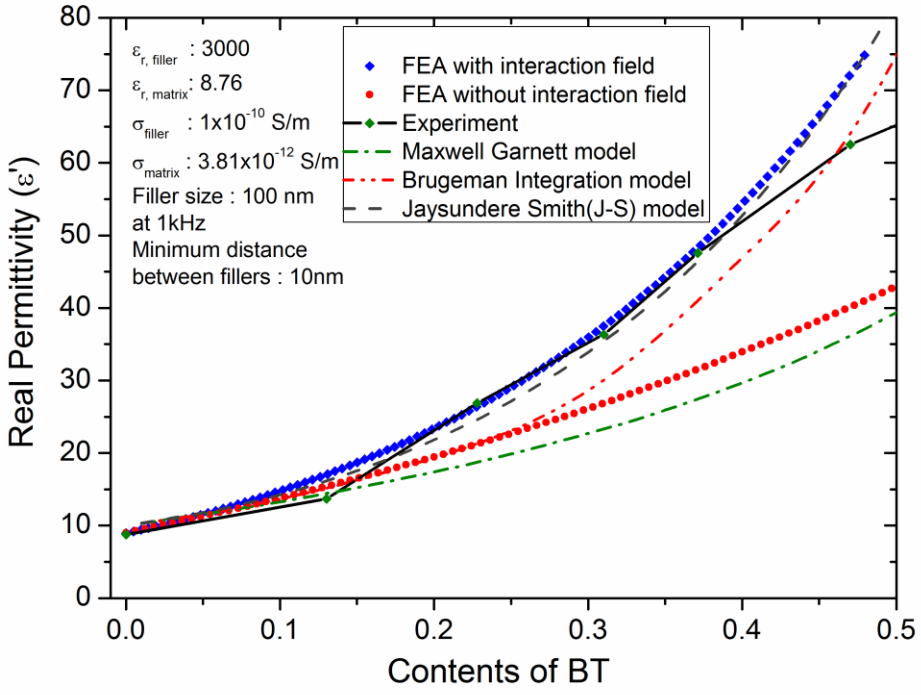

Figure 4.28. Experimental and FEA simulated real permittivity of composites as a function of BT content and calculated values by some numerical models.[83]

4.3 Conclusions

Polymer matrix hybrid nanocomposites with ferroelectric BT NPs and conductive MWCNT were fabricated by using a simple phase separation method. AC electrical measurements and microstructural characterization were performed for the dielectric nanocomposites. SEM images revealed the effective dispersion of BT NPs and MWCNT in the polymer matrix. The dielectric properties of the nanocomposites were improved by combining BT and MWCNT to increase the interfacial polarization between the matrix and the fillers. For instance, a real permittivity of 71.7 with a dielectric loss of 0.045 at 1 kHz was achieved in the nanocomposite with 37.1 vol % BT and 3 vol % MWCNT. BT NPs with different sizes were synthesized by a one-step hydrothermal reaction. It was found that the nanocomposites with BT NPs of 40 nm or smaller showed lower real permittivity, which is believed to be due to decreased ferroelectricity of BT NPs in that size range.

PVDF showed phase transformation from α to β during coagulation phase separation and reverted from β to α after post-annealing and quenching heat treatment. An improved breakdown strength of dielectric nanocomposite was observed after the heat treatments.

An equivalent circuit model of a modified Debye circuit and a parallel RC circuit in series was proposed to quantitatively describe the dielectric responses of the multi-phase nanocomposites. The finite element approach was selected for simulating the dielectric responses of polymer matrix nanocomposites with one or more types of fillers. Good agreement was obtained between the experimental results and the 3D modeling results. The 3D simulation model can be applicable to different composite systems with fillers of different shapes and properties. The easy processability, excellent dielectric performance and high flexibility make BT/MWCNT/PVDF nanocomposites attractive for applications in flexible electronics, embedded devices and electrostatic charge storage devices.

CHAPTER 5

CONCLUSIONS AND SUGGESTED FUTURE WORK

5.1 Conclusions

5.1.1 Conclusions in Conductive PMCs

- The formation of the phase segregated networks of the conductive filler in the polymer matrix composites resulted in high performance conductive material at very low concentration of the conductive filler

- The low percolation threshold of the mechanically blended PMCs provides some advantages such as processability, flexibility, low cost, and optical properties compared to conventional polymer matrix composites with random percolation networks.

- The phase segregated PMMA and ATO nanocomposites made from monosize and polydisperse PMMA showed the effects of the size and the size distribution of the matrix polymer microspheres on the electrical percolation behaviors.

- The percolation threshold (ρ_c) was 0.18 vol % for the monosize PMMA and 0.27 vol % for the polydisperse PMMA.

- The effects of the processing conditions on the electrical conductivity and the microstructure were investigated using impedance spectroscopy and SEM. It was evident that the microstructure was very sensitive to the processing conditions.

- The fractured surfaces showed trans-granular crack propagation due to low viscosity of the matrix and high filler penetration at the higher temperatures and pressures. The final electrical conductivity can deviate by more than 2 orders of magnitude by changing the compression molding temperature and/or pressure for the composites containing the same amount of the filler.

- The finite element approach was used for simulating the impedance responses of insulator-conductor nanocomposites, which have the phase segregated microstructures. Good agreement was obtained between the experimental results and the modeling results by using a filler packing density model and realistic filler conductivity values.

- The finite element simulation models are believed to be applicable to many different kinds of nanocomposite systems with phase segregated structures and not just those that were presented here.

5.1.2 Conclusions in Dielectric PMCs

- Core-shell structured polymer matrix nanocomposites with barium titanate nanoparticles (BT NPs) and multiwall carbon nanotubes (MWCNTs) hybrid fillers were fabricated by a simple phase separation method.

- BT NPs and MWCNTs were dispersed homogeneously in the polymer matrix.

- The dielectric properties of the nanocomposites were improved by combining BT and MWCNTs as the fillers in the PMCs. The uniformly dispersed BT and MWCNTs fillers have shown synergetic effects on the interfacial polarization between the matrix and the fillers. A high real permittivity (71.7) and a low dielectric loss (0.045) were achieved with 37.1 vol % BT NPs and 3 vol % MWCNT. The breakdown strength was improved by annealing heat treatments.

- For quantitative analysis of the charge transport and charge accumulation mechanisms in the dielectric PMCs, an equivalent circuit model of a modified Debye circuit and a parallel RC circuit in series was introduced to describe the dielectric responses of the multi-phase nanocomposites.

- Finite element simulations were conducted for quantitative analysis and improved predictability of the dielectric responses of the polymer matrix nanocomposites with one or more types of fillers. It was found to be necessary to use an interaction

term to more accurately predict the dielectric properties. The geometry-based 3D finite element simulation model is believed to be applicable to different composite systems with fillers of different shapes and properties.

5.2 Suggested Future Work

This research has demonstrated the phase segregated conductive PMCs though mechanical blending followed by a compression molding. The percolation networks are easily formed via this processing technique and are dependent on the physical arrangement of the fillers. Although a considerable effort has been dedicated to the formation of the percolation networks and to the optimization of multifunctional properties in the conductive PMCs, the segregated structure itself limits the maximum amount of the filler that can be used. Further enhancement of the maximum conductivity is required to meet the electrical conductivity requirements for practical applications. Since the formation of the phase segregated percolation networks using mechanical blending is more dependent on the processing than the materials themselves, possible solutions may include: (1) using more highly conductive nanomaterials as fillers, (2) improving the connectivity of the conductive percolation channels by using surface treatment for the fillers or by using high aspect ratio fillers, (3) by further optimizing the fabrication processes. In terms of the production cost, the hybrid filler approach combining cost effective conventional fillers (i.e. graphite and CB) with more properties effective fillers (i.e. CNTs, carbon fibers, and carbon nanosheets) may show synergistic effects and may be a promising alternative to lower the fabrication cost of the conductive PMCs. Conducting additional finite element simulations may help to select and design the new composite systems for obtaining better properties.

This research also included progress in improving the performance of the dielectric polymer matrix composites. The greatest challenge in the dielectric PMCs

remain in the nature of the properties of the dielectric PMCs which are based on compromise. To improve dielectric permittivity, dielectric loss and breakdown strength together, much more effort needs to be done by designing the composite materials, rather than simple mixing of the precursor materials. Most importantly, improving the interfaces between the matrix and the filler must be achieved to meet the requirements needed for certain applications, such as high energy density electric energy storage. Controlling the heat during charging and discharging operations is another very important task that requires improving the breakdown strength of the dielectric PMCs. More simulation work needs to be done for optimizing the structures and the design of the dielectric PMCs.

APPENDIX A

HYDROTHERMAL SYNTHESIS OF BT NANOCRYSTALS

A.1 Two Step Hydrothermal Reaction for BT Crystals with Different Shapes

The synthesis of barium titanate is highly dependent on the nature of the precursor materials used. The common titanium precursors include inorganic salts, such as $TiCl_3$ and $TiOSO_4$ or organometallic compounds such as titanium acetylacetonate and titanium isopropoxide, which are usually expensive, corrosive, and sensitive to moisture.[145] Other precursor materials such as layered alkali-metals or layered protonic titanates have shown a significant influence on both the formation and the growth of titanate crystals.[164, 165] The protonic $H_2Ti_3O_7$ nanotubes and nanowires, which can be prepared from $Na_2Ti_3O_7$ by H^+/Na^+ ion-exchange reaction in a HCl solution has been used for the synthesis of titanate crystals with different shapes and sizes.[99, 165] In this study, $Na_2Ti_3O_7$ was directly used as a precursor for the synthesis of barium titanate with different sizes and shapes because it was found that $Na_2Ti_3O_7$ nanotubes and nanowires can be split into small fragments to become more complex BT crystals or can dehydrate and crystallize to form BT nanowires directly, depending on the reaction conditions.[145]

3.0 g of TiO_2 (anatase) (US Research Nanomaterials, 99.9%) was dispersed in 140 mL of a 10 M NaOH aqueous solution in a 200 ml Teflon-lined stainless steel autoclave by stirring for 1h. After sealing, the autoclave reactor was heated at 240 ℃ for 72 h. After cooling to room temperature, the precipitated $Na_2Ti_3O_7$ was collected, washed several times with distilled water and ethanol, and then dried on a hot plate at 70 ℃ for 12 h.

A certain amount of $Na_2Ti_3O_7$ was dispersed in 140 mL of a $Ba(OH)_2 \cdot 8H_2O$ solution of different concentrations by stirring for 1h. The molar ratio of titanium and barium was maintained as 1:1.5 throughout the whole process. After sealing, the autoclave was heated at different temperatures (80, 120 and 140 ℃) for 24 h for the BT

crystals with different shapes and heated at 210 ℃ for 85 min for BT NWs, then cooled to room temperature. The precipitate was collected after washing with 0.1 M aqueous solution of CH_3COOH, distilled water and ethanol, and then dried on a hot plate at 70 ℃ for 12 h. Figure A.1 shows TEM images of the hydrothermally synthesized BT crystals with different shapes. The star shaped BT was obtained at the lowest reaction temperature of 80 ℃ in 0.2 M $Ba(OH)_2 \cdot 8H_2O$ solution for 24 h. The intermediate sword shaped BT was obtained at 120 ℃ in 0.1 M $Ba(OH)_2 \cdot 8H_2O$ solution for 24 h. The cube shaped BT nanocrystal was obtained at 140 ℃ in 0.2 M $Ba(OH)_2 \cdot 8H_2O$ solution for 24 h. BT nanowires were obtained at 210 ℃ in 0.1 M $Ba(OH)_2 \cdot 8H_2O$ solution for 85 min. Figure A.2 shows the influences of the hydrothermal reaction conditions on the shapes of BT crystals. The $Na_2Ti_3O_7$ nanowires were split into small pieces during the early stage of reaction, then the small fragments were directly crystalized into cube shaped BT nanocrystals at relatively high temperature (140 ℃) or they reassemble to form relatively large intermediate crystals at relatively low reaction temperatures (80 and 120 ℃).[145] However, the $Na_2Ti_3O_7$ nanowires directly crystallized into BT NWs, when high enough temperature (210 ℃) was used to complete the reaction within a short period of time (85 min).

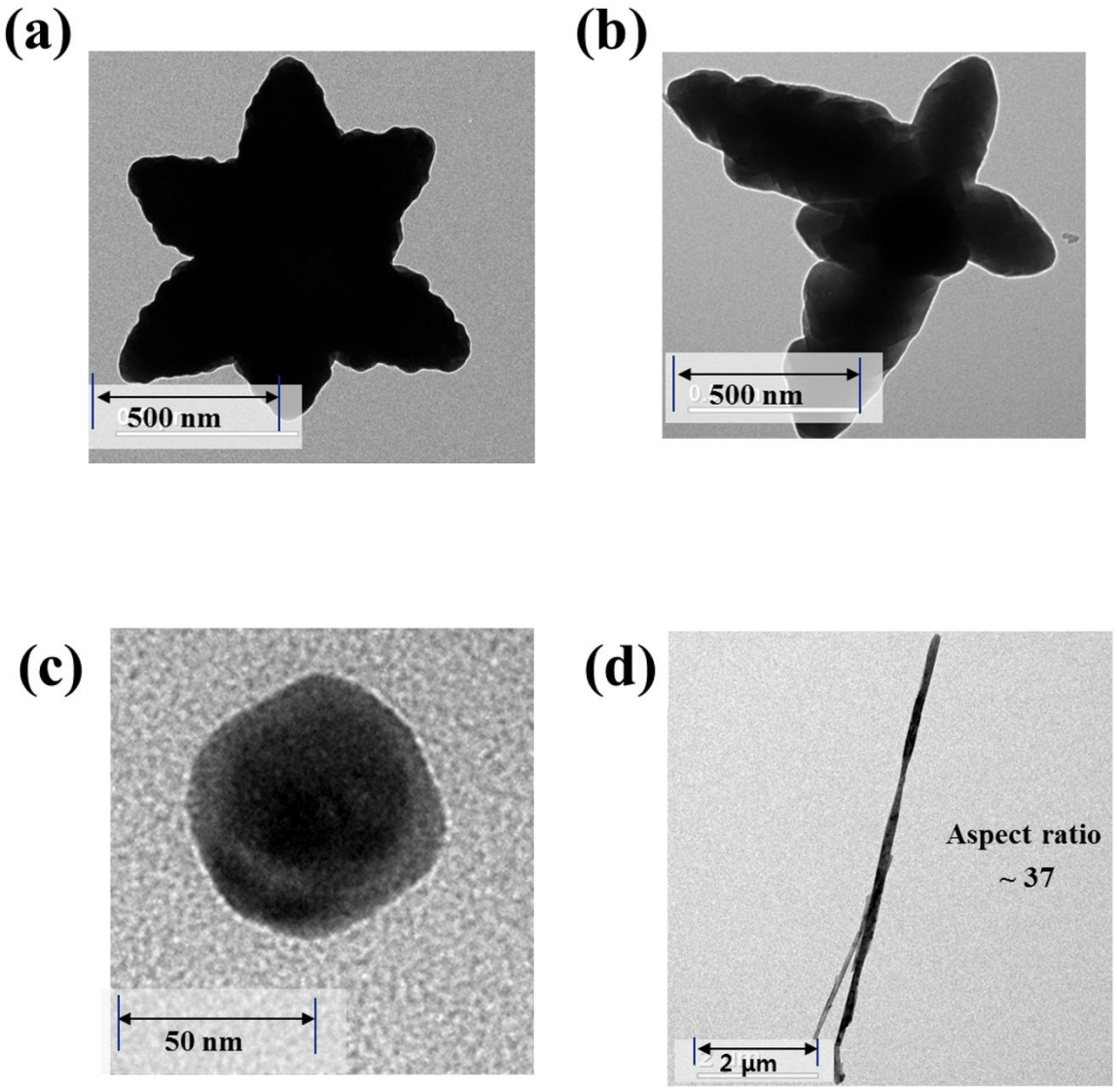

Figure A.1. TEM images of hydrothermally synthesized BT crystals with different shapes: (a) star (80 ℃ / 0.2 M $Ba(OH)_2 \cdot 8H_2O$**)**, (b) sword (120 ℃ / 0.1 M $Ba(OH)_2 \cdot 8H_2O$), (c) cube (140 ℃ / 0.2 M $Ba(OH)_2 \cdot 8H_2O$), (d) Nanowire (210 ℃ / 0.1 M $Ba(OH)_2 \cdot 8H_2O$).

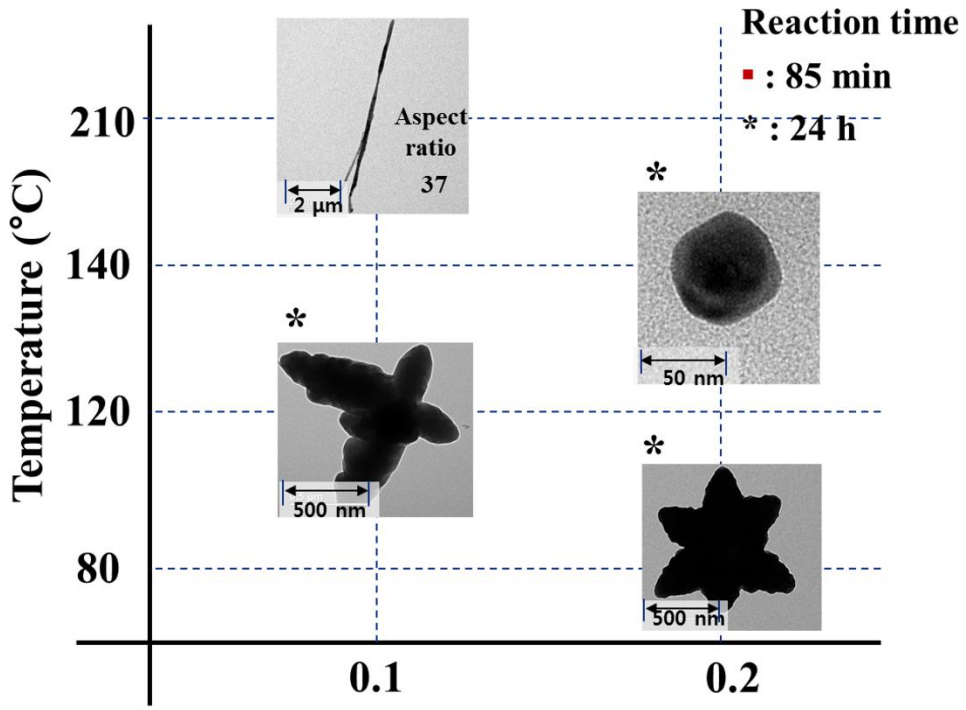

Figure A.2. Influence of the hydrothermal reaction conditions on the shapes of the synthesized BT crystals.

A.2 One Step Hydrothermal Reaction for BT Nanoparticles with Different Sizes

Barium titanate with different shapes can be easily obtained from two step hydrothermal reactions with different temperatures and different concentrations of $Ba(OH)_2 \cdot 8H_2O$ solution as shown above. However, the size of BT nanoparticles was not easily changed using the two-step hydrothermal reaction. Although it has been reported that BT nanoparticles were synthesized in different sizes using solvothermal reactions in different solvents and precursors,[95] it is also important to have BT NPs in different sizes using the same reaction conditions with the same solvent and precursors to be able to compare the effects of the filler particle size on the dielectric properties of polymer matrix composites. The synthesis of BT nanoparticles of different size was done by one-step hydrothermal reaction using TiO_2 (anatase) as a precursor.

1.13 g of TiO_2 anatase (US Research Nanomaterials, 99.9%)) was dispersed in 0.2 M $Ba(OH)_2 \cdot 8H_2O$ solution by stirring for 1 h in a 200 ml Teflon-lined stainless steel

autoclave. The molar ratio of titanium and barium was maintained as 1:1.5 to fully transfer the TiO_2 to BT. After sealing, the autoclave was heated at 180° for different reaction times (3, 6, 12, 24, 48 and 72 h). As the reaction time increased, the size of BT nanoparticles gradually increased as shown in Fig. 4.5. However, x-ray diffraction patterns in Fig. 4.3 showed that pure and crystalline BT NPs without any indication of un-reacted TiO_2 or barium carbonate ($BaCO_3$) can be obtained only when the reaction was held more than 6 h.

REFERENCES

[1] R.-M. Wang, S.-R. Zheng, and Y.-P. Zheng, *Introduction to polymer matrix composites*. Padstow: Woodhead Publishing, 2011.

[2] F. Hussain, M. Hojjati, M. Okamoto, and R. E. Gorga, "Review article: Polymer-Matrix Nanocomposites, Processing, Manufacturing, and Application: An Overview," *Journal of Composite Materials*, vol. 40, pp. 1511-1575, 2006.

[3] D. Stauffer and A. Aharony, *Introduction to Percolation Theory*: Oxford University Press, New York, 1971.

[4] H. Pang, L. Xu, D.-X. Yan, and Z.-M. Li, "Conductive Polymer Composites with Segregated Structures," *Progress in Polymer Science*, vol. 39, pp. 1908-1933, 2014.

[5] Z.-M. Dang, J.-K. Yuan, J.-W. Zha, T. Zhou, S.-T. Li, and G.-H. Hu, "Fundamentals, Processes and Applications of High-Permittivity Polymer–Matrix Composites," *Progress in Materials Science*, vol. 57, pp. 660-723, 2012.

[6] Y. Jin and R. A. Gerhardt, "Prediction of the Percolation Threshold and Electrical Conductivity of Self-Assembled Antimony-Doped Tin Oxide Nanoparticles into Ordered Structures in PMMA/ATO Nanocomposites," *ACS Applied Materials & Interfaces*, vol. 6, pp. 22264-22271, 2014.

[7] J. Waddell, R. Ou, C. J. Capozzi, S. Gupta, C. A. Parker, R. A. Gerhardt, K. Seal, S. V. Kalinin, and A. P. Baddorf, "Detection of Percolating Paths in Polyhedral Segregated Network Composites Using Electrostatic Force Microscopy and Conductive Atomic Force Microscopy," *Applied Physics Letters*, vol. 95, p. 233122 2009.

[8] H. Da and N. N. Ekere, "Effect of Particle Size Ratio on the Conducting Percolation Threshold of Granular Conductive–Insulating Composites," *Journal of Physics D: Applied Physics*, vol. 37, p. 1848, 2004.

[9] C.-W. Nan, Y. Shen, and J. Ma, "Physical Properties of Composites Near Percolation," *Annual Review of Materials Research*, vol. 40, pp. 131-151, 2010.

[10] C. J. Capozzi and R. A. Gerhardt, "Correlation of the ac Electrical Conductivity and the Microstructure of PMMA/ITO Nanocomposites That Possess Phase-Segregated Microstructures," *The Journal of Physical Chemistry C*, vol. 112, pp. 19372-19382, 2008.

[11] Y. Jin, N. Xia, and R. A. Gerhardt, "Dielectric Nanocomposite with High Dielectric Permittivity and Low Dielectric Loss," in *Electrical Insulation Conference (EIC), 2015 IEEE*, 2015, pp. 442-445.

[12] P. Barber, S. Balasubramanian, Y. Anguchamy, S. Gong, A. Wibowo, H. Gao, H. Ploehn, and H.-C. Zur Loye, "Polymer Composite and Nanocomposite Dielectric Materials for Pulse Power Energy Storage," *Materials*, vol. 2, pp. 1697-1733, 2009.

[13] M. Sahimi, *Applications of Percolation Theory*. Routledge, UK: CRC Press, 1994.

[14] J. W. Essam, "Percolation Theory," *Reports on Progress in Physics*, vol. 43, p. 833, 1980.

[15] F. Lux, "Models Proposed to Explain the Electrical Conductivity of Mixtures made of Conductive and Insulating Materials," *Journal of Materials Science,* vol. 28, pp. 285-301, 1993.
[16] J. Runyan, R. A. Gerhardt, and R. Ruh, "Electrical Properties of Boron Nitride Matrix Composites: I, Analysis of McLachlan Equation and Modeling of the Conductivity of Boron Nitride–Boron Carbide and Boron Nitride–Silicon Carbide Composites," *Journal of the American Ceramic Society,* vol. 84, pp. 1490-1496, 2001.
[17] S. Kirkpatrick, "Percolation and Conduction," *Reviews of Modern Physics,* vol. 45, pp. 574-588, 1973.
[18] C. J. Capozzi, "Controlled Self-Assembly of ITO Nanoparticles into Aggregate Wire Structures in PMMA-ITO Nanocomposites," PhD Thesis, Materials Science and Engineering, Georgia Institute of Technology, Atlanta, 2009.
[19] S. Gupta, R. Ou, and R. A. Gerhardt, "Effect of the Fabrication Method on the Electrical Properties of Poly(acrylonitrile-co-butadiene-co-styrene)/Carbon Black Composites," *Journal of Electronic Materials,* vol. 35, pp. 224-229, 2006.
[20] H. Pang, C. Chen, Y. Bao, J. Chen, X. Ji, J. Lei, and Z.-M. Li, "Electrically Conductive Carbon Nanotube/Ultrahigh Molecular Weight Polyethylene Composites with Segregated and Double Percolated Structure," *Materials Letters,* vol. 79, pp. 96-99, 2012.
[21] J. Chen, Y. Shi, J. Yang, N. Zhang, T. Huang, C. Chen, Y. Wang, and Z.-w. Zhou, "A Simple Strategy to Achieve Very Low Percolation Threshold Via the Selective Distribution of Carbon Nanotubes at the Interface of Polymer Blends," *Journal of Materials Chemistry,* vol. 22, pp. 22398-22404, 2012.
[22] J. Yang, T. Xu, A. Lu, Q. Zhang, and Q. Fu, "Electrical Properties of Poly(phenylene sulfide)/Multiwalled Carbon Nanotube Composites Prepared by Simple Mixing and Compression," *Journal of Applied Polymer Science,* vol. 109, pp. 720-726, 2008.
[23] L. Xie, X. Huang, C. Wu, and P. Jiang, "Core-Shell Structured Poly(methyl methacrylate)/$BaTiO_3$ Nanocomposites Prepared by in situ Atom Transfer Radical Polymerization: a Route to High Dielectric Constant Materials with the Inherent Low Loss of the Base Polymer," *Journal of Materials Chemistry,* vol. 21, pp. 5897-5906, 2011.
[24] I. Jurewicz, P. Worajittiphon, A. A. K. King, P. J. Sellin, J. L. Keddie, and A. B. Dalton, "Locking Carbon Nanotubes in Confined Lattice Geometries − A Route to Low Percolation in Conducting Composites," *The Journal of Physical Chemistry B,* vol. 115, pp. 6395-6400, 2011.
[25] C. J. Capozzi and R. A. Gerhardt, "Novel Percolation Mechanism in PMMA Matrix Composites Containing Segregated ITO Nanowire Networks," *Advanced Functional Materials,* vol. 17, pp. 2515-2521, 2007.
[26] T. L. Pruyn and R. A. Gerhardt, "Percolation in Borosilicate Glass Matrix Composites Containing Antimony-Doped Tin Oxide Segregated Networks. Part I: Fabrication of Segregated Networks," *Journal of the American Ceramic Society,* vol. 96, pp. 3544-3551, 2013.
[27] H. Scher and R. Zallen, "Critical Density in Percolation Processes," *The Journal of Chemical Physics,* vol. 53, pp. 3759-3761, 1970.

[28] J. Chen, Y.-y. Shi, J.-h. Yang, N. Zhang, T. Huang, C. Chen, Y. Wang, and Z.-w. Zhou, "A simple strategy to achieve very low percolation threshold via the selective distribution of carbon nanotubes at the interface of polymer blends," *Journal of Materials Chemistry*, vol. 22, pp. 22398-22404, 2012.

[29] G. A. Gelves, M. H. Al-Saleh, and U. Sundararaj, "Highly Electrically Conductive and High Performance EMI Shielding Nanowire/polymer Nanocomposites by Miscible Mixing and Precipitation," *Journal of Materials Chemistry*, vol. 21, pp. 829-836, 2011.

[30] R. Ou, S. Gupta, C. A. Parker, and R. A. Gerhardt, "Fabrication and Electrical Conductivity of Poly(methyl methacrylate) (PMMA)/Carbon black (CB) Composites: Comparison Between an Ordered Carbon Black Nanowire-Like Segregated Structure and a Randomly Dispersed Carbon Black Nanostructure," *Journal of Physical Chemistry B*, vol. 110, pp. 22365-73, 2006.

[31] Y. P. Mamunya, H. Zois, L. Apekis, and E. V. Lebedev, "Influence of Pressure on the Electrical Conductivity of Metal Powders Used as Fillers in Polymer Composites," *Powder Technology*, vol. 140, pp. 49-55, 2004.

[32] A. Mierczynska, M. Mayne-L'Hermite, G. Boiteux, and J. K. Jeszka, "Electrical and Mechanical Properties of Carbon Nanotube/Ultrahigh-Molecular-Weight Polyethylene Composites Prepared by a Filler Prelocalization Method," *Journal of Applied Polymer Science*, vol. 105, pp. 158-168, 2007.

[33] J. Bouchet, C. Carrot, J. Guillet, G. Boiteux, G. Seytre, and M. Pineri, "Conductive Composites of UHMWPE and Ceramics Based on the Segregated Network Concept," *Polymer Engineering & Science*, vol. 40, pp. 36-45, 2000.

[34] L. A. Prystaj, E. A. Lucas, K. Alston, and R. A. Gerhardt., "Effect of Graphitic Filler Characteristics on the Percolation Behavior and Electrical Conductivity of Segregated Network Polymer Composites," *Nanotech Conference Proceedings*, vol. 1, 2016.

[35] T. L. Pruyn, "Investigation of Percolation in Borosilicate Glass Matrix Composites Containing Conducting Segregated Networks," PhD Thesis, Georgia Institute of Technology, Atlanta, GA, 2014.

[36] J. Du, L. Zhao, Y. Zeng, L. Zhang, F. Li, P. Liu, and C. Liu, "Comparison of Electrical Properties Between Multi-walled Carbon Nanotube and Graphene Nanosheet/High Density Polyethylene Composites with a Segregated Network Structure," *Carbon*, vol. 49, pp. 1094-1100, 2011.

[37] D.-X. Yan, H. Pang, B. Li, R. Vajtai, L. Xu, P.-G. Ren, J.-H. Wang, and Z.-M. Li, "Structured Reduced Graphene Oxide/Polymer Composites for Ultra-Efficient Electromagnetic Interference Shielding," *Advanced Functional Materials*, vol. 25, pp. 559-566, 2015.

[38] D. G. Stroppa, L. A. Montoro, A. Beltrán, T. G. Conti, R. O. da Silva, J. Andrés, E. Longo, E. R. Leite, and A. J. Ramirez, "Unveiling the Chemical and Morphological Features of $Sb{-}SnO_2$ Nanocrystals by the Combined Use of High-Resolution Transmission Electron Microscopy and ab Initio Surface Energy Calculations," *Journal of the American Chemical Society*, vol. 131, pp. 14544-14548, 2009.

[39] G. Lu, X. Li, H. Jiang, and X. Mao, "Electrical Conductivity of Carbon Fibers/ABS Resin Composites Mixed with Carbon Blacks," *Journal of Applied Polymer Science,* vol. 62, pp. 2193-2199, 1996.
[40] Z. M. Jarzebski and J. P. Morton, "Physical Properties of SnO_2 Materials: III . Optical Properties," *Journal of The Electrochemical Society,* vol. 123, pp. 333C-346C, 1976.
[41] T. G. Conti, A. J. Chiquito, R. O. Da Silva, E. Longo, and E. R. Leite, "Electrical Properties of Highly Conducting SnO_2:Sb Nanocrystals Synthesized using a Nonaqueous Sol–Gel Method," *Journal of the American Ceramic Society,* vol. 93, pp. 3862-3866, 2010.
[42] K. H. Kim, S. W. Lee, D. W. Shin, and C. G. Park, "Effect of Antimony Addition on Electrical and Optical Properties of Tin Oxide Film," *Journal of the American Ceramic Society,* vol. 77, pp. 915-921, 1994.
[43] J. Zhang, L. Gao, and M. Chen, "Spark Plasma Sintering of High-Density Antimony-Doped Tin Oxide Ceramics from Nanoparticles," *Journal of the American Ceramic Society,* vol. 89, pp. 3874-3876, 2006.
[44] J. Zhang and L. Gao, "Synthesis and Characterization of Antimony-Doped Tin Oxide (ATO) Nanoparticles by a New Hydrothermal Method," *Materials Chemistry and Physics,* vol. 87, pp. 10-13, 2004.
[45] F. J. Berry and C. Greaves, "A Neutron Diffraction Investigation of the Defect Rutile Structure of Tin-Antimony Oxide," *Journal of the Chemical Society, Dalton Transactions,* pp. 2447-2451, 1981.
[46] G. B. González, "Investigating the Defect Structures in Transparent Conducting Oxides Using X-ray and Neutron Scattering Techniques," *Materials,* vol. 5, p. 818, 2012.
[47] C. J. Capozzi, S. Shackelford, R. Ou, and R. A. Gerhardt, "Study of Percolation in PMMA / Indium Tin Oxide Composites," *MRS Online Proceedings Library,* vol. 819, 2004.
[48] R. J. Andrews and E. A. Grulke, *Polymer handbook*, 4th ed. New York: Wiley, 1999.
[49] H. Kobayashi, H. Takahashi, and Y. Hiki, "Viscosity Measurement of Organic Glasses Below and Above Glass Transition Temperature," *Journal of Non-Crystalline Solids,* vol. 290, pp. 32-40, 2001.
[50] K. C. Kao, *Dielectric Phenomena in Solids: with Emphasis on Physical Concepts of Electronic Processes*. San Diego: Elsevier, 2004.
[51] X. Zhang, Y. Shen, B. Xu, Q. Zhang, L. Gu, J. Jiang, J. Ma, Y. Lin, and C.-W. Nan, "Giant Energy Density and Improved Discharge Efficiency of Solution-Processed Polymer Nanocomposites for Dielectric Energy Storage," *Advanced Materials,* vol. 28, pp. 2055-2061, 2016.
[52] X. Huang and P. Jiang, "Core–Shell Structured High-k Polymer Nanocomposites for Energy Storage and Dielectric Applications," *Advanced Materials,* vol. 27, pp. 546-554, 2015.
[53] Y. Kim, "Ferroelectric Nanocomposite and Polar Hybrid Sol-Gel Materials for Efficient, High Energy Density Capacitors," PhD Thesis, Georgia Institute of Techonology, Atlanta, GA, 2014.

[54] V. A. Zakrevskii, N. T. Sudar, A. Zaopo, and Y. A. Dubitsky, "Mechanism of electrical degradation and breakdown of insulating polymers," *Journal of Applied Physics,* vol. 93, pp. 2135-2139, 2003.
[55] J. J. O'Dwyer, *The Theory of Electrical Conduction and Breakdown in Solid*. Oxford: Clarendon Press, 1973.
[56] Q. Li, G. Zhang, F. Liu, K. Han, M. R. Gadinski, C. Xiong, and Q. Wang, "Solution-Processed Ferroelectric Terpolymer Nanocomposites with High Breakdown Strength and Energy Density Utilizing Boron Nitride Nanosheets," *Energy & Environmental Science,* vol. 8, pp. 922-931, 2015.
[57] H. J. Ploehn, "Materials science: Composite for Energy Storage Takes the Heat," *Nature,* vol. 523, pp. 536-537, 2015.
[58] O. Levy and D. Stroud, "Maxwell Garnett Theory for Mixtures of Anisotropic Inclusions: Application to Conducting Polymers," *Physical Review B,* vol. 56, pp. 8035-8046, 1997.
[59] W. S. Weiglhofer, A. Lakhtakia, and B. Michel, "Maxwell Garnett and Bruggeman Formalisms for a Particulate Composite with Bianisotropic Host Medium," *Microwave and Optical Technology Letters,* vol. 15, pp. 263-266, 1997.
[60] M. G. Todd and F. G. Shi, "Complex Permittivity of Composite Systems: a Comprehensive Interphase Approach," *IEEE Transactions on Dielectrics and Electrical Insulation,* vol. 12, pp. 601-611, 2005.
[61] N. Jayasundere and B. V. Smith, "Dielectric Constant for Binary Piezoelectric 0-3 Composites," *Journal of Applied Physics,* vol. 73, pp. 2462-2466, 1993.
[62] C. Chiteme and D. S. McLachlan, "Measurements of Universal and Non-Universal Percolation Exponents in Macroscopically Similar Systems," *Physica B: Condensed Matter,* vol. 279, pp. 69-71, 2000.
[63] T. J. Lewis, "Interfaces: Nanometric Dielectrics," *Journal of Physics D: Applied Physics,* vol. 38, p. 202, 2005.
[64] X.-J. Zhang, G.-S. Wang, Y.-Z. Wei, L. Guo, and M.-S. Cao, "Polymer-Composite with High Dielectric Constant and Enhanced Absorption Properties Based on Graphene-CuS Nanocomposites and Polyvinylidene Fluoride," *Journal of Materials Chemistry A,* vol. 1, pp. 12115-12122, 2013.
[65] P. Kim, S. C. Jones, P. J. Hotchkiss, J. N. Haddock, B. Kippelen, S. R. Marder, and J. W. Perry, "Phosphonic Acid-Modified Barium Titanate Polymer Nanocomposites with High Permittivity and Dielectric Strength," *Advanced Materials,* vol. 19, pp. 1001-1005, 2007.
[66] J. Li, S. I. Seok, B. Chu, F. Dogan, Q. Zhang, and Q. Wang, "Nanocomposites of Ferroelectric Polymers with TiO_2 Nanoparticles Exhibiting Significantly Enhanced Electrical Energy Density," *Advanced Materials,* vol. 21, pp. 217-221, 2009.
[67] H. Tang and H. A. Sodano, "Ultra High Energy Density Nanocomposite Capacitors with Fast Discharge Using $Ba_{0.2}Sr_{0.8}TiO_3$ Nanowires," *Nano Letters,* vol. 13, pp. 1373-1379, 2013.
[68] P. Thomas, K. T. Varughese, K. Dwarakanath, and K. B. R. Varma, "Dielectric properties of Poly(vinylidene fluoride)/$CaCu_3Ti_4O_{12}$ Composites," *Composites Science and Technology,* vol. 70, pp. 539-545, 2010.

[69] L. Xie, X. Huang, Y. Huang, K. Yang, and P. Jiang, "Core@Double-Shell Structured $BaTiO_3$–Polymer Nanocomposites with High Dielectric Constant and Low Dielectric Loss for Energy Storage Application," *The Journal of Physical Chemistry C,* vol. 117, pp. 22525-22537, 2013.

[70] Y. Feng, W. L. Li, Y. F. Hou, Y. Yu, W. P. Cao, T. D. Zhang, and W. D. Fei, "Enhanced Dielectric Properties of PVDF-HFP/$BaTiO_3$-Nanowire Composites Induced by Interfacial Polarization and Wire-Shape," *Journal of Materials Chemistry C,* vol. 3, pp. 1250-1260, 2015.

[71] Z. Wang, J. K. Nelson, J. Miao, R. J. Linhardt, L. S. Schadler, H. Hillborg, and S. Zhao, "Effect of High Aspect Ratio Filler on Dielectric Properties of Polymer Composites: A Study on Barium Titanate Fibers and Graphene Platelets," *IEEE Transactions on Dielectrics and Electrical Insulation,* vol. 19, pp. 960-967, 2012.

[72] H. Tang, Z. Zhou, C. C. Bowland, and H. A. Sodano, "Synthesis of Calcium Copper Titanate ($CaCu_3Ti_4O_{12}$) Nanowires with Insulating SiO_2 Barrier for Low Loss High Dielectric Constant Nanocomposites," *Nano Energy,* vol. 17, pp. 302-307, 2015.

[73] J.-Y. Kim, J. Lee, W. H. Lee, I. N. Kholmanov, J. W. Suk, T. Kim, Y. Hao, H. Chou, D. Akinwande, and R. S. Ruoff, "Flexible and Transparent Dielectric Film with a High Dielectric Constant Using Chemical Vapor Deposition-Grown Graphene Interlayer," *ACS Nano,* vol. 8, pp. 269-274, 2014.

[74] H. Liu, Y. Shen, Y. Song, C.-W. Nan, Y. Lin, and X. Yang, "Carbon Nanotube Array/Polymer Core/Shell Structured Composites with High Dielectric Permittivity, Low Dielectric Loss, and Large Energy Density," *Advanced Materials,* vol. 23, pp. 5104-5108, 2011.

[75] D. Tasis, N. Tagmatarchis, A. Bianco, and M. Prato, "Chemistry of Carbon Nanotubes," *Chemical Reviews,* vol. 106, pp. 1105-1136, 2006.

[76] P. C. Ma, J.-K. Kim, and B. Z. Tang, "Functionalization of Carbon Nanotubes Using a Silane Coupling Agent," *Carbon,* vol. 44, pp. 3232-3238, 2006.

[77] S. A. Paniagua, Y. Kim, K. Henry, R. Kumar, J. W. Perry, and S. R. Marder, "Surface-Initiated Polymerization from Barium Titanate Nanoparticles for Hybrid Dielectric Capacitors," *ACS Applied Materials & Interfaces,* vol. 6, pp. 3477-3482, 2014.

[78] M. N. Tchoul, S. P. Fillery, H. Koerner, L. F. Drummy, F. T. Oyerokun, P. A. Mirau, M. F. Durstock, and R. A. Vaia, "Assemblies of Titanium Dioxide-Polystyrene Hybrid Nanoparticles for Dielectric Applications," *Chemistry of Materials,* vol. 22, pp. 1749-1759, 2010.

[79] Z. Li, L. A. Fredin, P. Tewari, S. A. Dibenedetto, M. T. Lanagan, M. A. Ratner, and T. J. Marks, "In Situ Catalytic Encapsulation of Core-Shell Nanoparticles Having Variable Shell Thickness: Dielectric and Energy Storage Properties of High-Permittivity Metal Oxide Nanocomposites," *Chemistry of Materials,* vol. 22, pp. 5154-5164, 2010.

[80] H. M. Jung, J.-H. Kang, S. Y. Yang, J. C. Won, and Y. S. Kim, "Barium Titanate Nanoparticles with Diblock Copolymer Shielding Layers for High-Energy Density Nanocomposites," *Chemistry of Materials,* vol. 22, pp. 450-456, 2010.

[81] X. Pang, Y. He, B. Jiang, J. Iocozzia, L. Zhao, H. Guo, J. Liu, M. Akinc, N. Bowler, X. Tan, and Z. Lin, "Block Copolymer/Ferroelectric Nanoparticle Nanocomposites," *Nanoscale,* vol. 5, pp. 8695-8702, 2013.

[82] P. Kim, N. M. Doss, J. P. Tillotson, P. J. Hotchkiss, M.-J. Pan, S. R. Marder, J. Li, J. P. Calame, and J. W. Perry, "High Energy Density Nanocomposites Based on Surface-Modified $BaTiO_3$ and a Ferroelectric Polymer," *ACS Nano,* vol. 3, pp. 2581-2592, 2009.

[83] Y. Jin, N. Xia, and R. A. Gerhardt, "Enhanced Dielectric Properties of Polymer Matrix Composites with $BaTiO_3$ and MWCNT Hybrid Fillers using Simple Phase Separation," *Nano Energy,* vol. submitted, 2016.

[84] Y. Jin and R. A. Gerhardt, "Dielectric Properties and Charge Storage Optimization in Poly(vinylidene fluoride) Polymer Matrix Hybrid Nanocomposites with $BaTiO_3$ and Multi-Walled Carbon Nanotubes," *Nanotech Conference Proceedings,* vol. 1, 2016.

[85] K. Yang, X. Huang, Y. Huang, L. Xie, and P. Jiang, "Fluoro-Polymer@$BaTiO_3$ Hybrid Nanoparticles Prepared via RAFT Polymerization: Toward Ferroelectric Polymer Nanocomposites with High Dielectric Constant and Low Dielectric Loss for Energy Storage Application," *Chemistry of Materials,* vol. 25, pp. 2327-2338, 2013.

[86] Y. Shen, Y. H. Lin, and C. W. Nan, "Interfacial Effect on Dielectric Properties of Polymer Nanocomposites Filled with Core/Shell-Structured Particles," *Advanced Functional Materials,* vol. 17, pp. 2405-2410, 2007.

[87] K. Yu, Y. Niu, Y. Bai, Y. Zhou, and H. Wang, "Poly(vinylidene fluoride) Polymer Based Nanocomposites with Significantly Reduced Energy Loss by Filling with Core-Shell Structured $BaTiO_3/SiO_2$ Nanoparticles," *Applied Physics Letters,* vol. 102, p. 102903, 2013.

[88] T. J. Lewis, "Interfaces are the Dominant Feature of Dielectrics at the Nanometric Level," *IEEE Transactions on Dielectrics and Electrical Insulation,* vol. 11, pp. 739-753, 2004.

[89] D.-H. Kuo, C.-C. Chang, T.-Y. Su, W.-K. Wang, and B.-Y. Lin, "Dielectric Behaviours of Multi-Doped $BaTiO_3$/Epoxy Composites," *Journal of the European Ceramic Society,* vol. 21, pp. 1171-1177, 2001.

[90] Z.-M. Dang, T. Zhou, S.-H. Yao, J.-K. Yuan, J.-W. Zha, H.-T. Song, J.-Y. Li, Q. Chen, W.-T. Yang, and J. Bai, "Advanced Calcium Copper Titanate/Polyimide Functional Hybrid Films with High Dielectric Permittivity," *Advanced Materials,* vol. 21, pp. 2077-2082, 2009.

[91] W. Hu, Y. Liu, R. L. Withers, T. J. Frankcombe, L. Norén, A. Snashall, M. Kitchin, P. Smith, B. Gong, H. Chen, J. Schiemer, F. Brink, and J. Wong-Leung, "Electron-Pinned Defect-Dipoles for High-Performance Colossal Permittivity Materials," *Nat Mater,* vol. 12, pp. 821-826, 2013.

[92] V. Hornebecq, C. Huber, M. Maglione, M. Antonietti, and C. Elissalde, "Dielectric Properties of Pure $(BaSr)TiO_3$ and Composites with Different Grain Sizes Ranging from the Nanometer to the Micrometer," *Advanced Functional Materials,* vol. 14, pp. 899-904, 2004.

[93] S. Wada, A. Yazawa, T. Hoshina, Y. Kameshima, H. Kakemoto, T. Tsurumi, and Y. Kuroiwa, "Preparation of Barium Titanate Nanoparticle Sphere Arrays and

Their Dielectric Properties," *IEEE Transactions on Ultrasonics, Ferroelectrics, and Frequency Control,* vol. 55, pp. 1895-1899, 2008.
[94] M. Schoijet, "On the Anomalous Crystallographic Properties of Small Barium Titanate Particles," *British Journal of Applied Physics,* vol. 15, p. 719, 1964.
[95] Y. P. Mao, S. Y. Mao, Z.-G. Ye, Z. X. Xie, and L. S. Zheng, "Size-Dependences of the Dielectric and Ferroelectric Properties of $BaTiO_3$/Polyvinylidene Fluoride Nanocomposites," *Journal of Applied Physics,* vol. 108, p. 014102, 2010.
[96] B.-H. Fan, J.-W. Zha, D. Wang, J. Zhao, and Z.-M. Dang, "Size-Dependent Low-Frequency Dielectric Properties in the $BaTiO_3$/Poly(vinylidene fluoride) Nanocomposite Films," *Applied Physics Letters,* vol. 100, p. 012903, 2012.
[97] N. Guo, S. A. DiBenedetto, P. Tewari, M. T. Lanagan, M. A. Ratner, and T. J. Marks, "Nanoparticle, Size, Shape, and Interfacial Effects on Leakage Current Density, Permittivity, and Breakdown Strength of Metal Oxide−Polyolefin Nanocomposites: Experiment and Theory," *Chemistry of Materials,* vol. 22, pp. 1567-1578, 2010.
[98] F. Ning, M. Shao, C. Zhang, S. Xu, M. Wei, and X. Duan, "Co_3O_4@Layered Double Hydroxide Core/Shell Hierarchical Nanowire Arrays for Enhanced Supercapacitance Performance," *Nano Energy,* vol. 7, pp. 134-142, 2014.
[99] H. Tang, Y. Lin, and H. A. Sodano, "Synthesis of High Aspect Ratio $BaTiO_3$ Nanowires for High Energy Density Nanocomposite Capacitors," *Advanced Energy Materials,* vol. 3, pp. 451-456, 2013.
[100] S. Ricardo, S. Jaime, V. Richard, S. Vítor, C. Pedro, G. João, and L.-M. Senentxu, "Low Percolation Transitions in Carbon Nanotube Networks Dispersed in a Polymer Matrix: Dielectric Properties, Simulations and Experiments," *Nanotechnology,* vol. 20, p. 035703, 2009.
[101] F. Dalmas, R. Dendievel, L. Chazeau, J.-Y. Cavaillé, and C. Gauthier, "Carbon Nanotube-Filled Polymer Composites. Numerical Simulation of Electrical Conductivity in Three-Dimensional Entangled Fibrous Networks," *Acta Materialia,* vol. 54, pp. 2923-2931, 2006.
[102] Z.-M. Dang, M.-S. Zheng, and J.-W. Zha, "1D/2D Carbon Nanomaterial-Polymer Dielectric Composites with High Permittivity for Power Energy Storage Applications," *Small,* pp. 1688-1701, 2016.
[103] A. Karatrantos, R. J. Composto, K. I. Winey, and N. Clarke, "Structure and Conformations of Polymer/SWCNT Nanocomposites," *Macromolecules,* vol. 44, pp. 9830-9838, 2011.
[104] H. Tang, G. J. Ehlert, Y. Lin, and H. A. Sodano, "Highly Efficient Synthesis of Graphene Nanocomposites," *Nano Letters,* vol. 12, pp. 84-90, 2012.
[105] J.-Y. Kim, T. Kim, J. W. Suk, H. Chou, J.-H. Jang, J. H. Lee, I. N. Kholmanov, D. Akinwande, and R. S. Ruoff, "Enhanced Dielectric Performance in Polymer Composite Films with Carbon Nanotube-Reduced Graphene Oxide Hybrid Filler," *Small,* vol. 10, pp. 3405-3411, 2014.
[106] S. Biswas, G. P. Kar, D. Arora, and S. Bose, "A Unique Strategy Towards High Dielectric Constant and Low Loss with Multiwall Carbon Nanotubes Anchored onto Graphene Oxide Sheets," *RSC Advances,* vol. 5, pp. 24132-24138, 2015.
[107] R. R. Kohlmeyer, A. Javadi, B. Pradhan, S. Pilla, K. Setyowati, J. Chen, and S. Gong, "Electrical and Dielectric Properties of Hydroxylated Carbon

Nanotube−Elastomer Composites," *The Journal of Physical Chemistry C,* vol. 113, pp. 17626-17629, 2009.
[108] Y. Rao and C. P. Wong, "Material Characterization of a High-Dielectric-Constant Polymer–Ceramic Composite for Embedded Capacitor for RF Applications," *Journal of Applied Polymer Science,* vol. 92, pp. 2228-2231, 2004.
[109] F. Carpi, G. Gallone, F. Galantini, and D. DeRossi, "Silicone–Poly(hexylthiophene) Blends as Elastomers with Enhanced Electromechanical Transduction Properties," *Advanced Functional Materials,* vol. 18, pp. 235-241, 2008.
[110] L. Zhiying, G. Xindong, Z. Zhiwei, Q. Zhijun, W. Dongping, Z. Zhi-Bin, and Z. Shi-Li, "Solution-Processed Logic Gates Based On Nanotube/Polymer Composite," *Electron Devices, IEEE Transactions on,* vol. 60, pp. 2542-2547, 2013.
[111] Y. Liu, H. Lv, X. Lan, J. Leng, and S. Du, "Review of Electro-Active Shape-Memory Polymer Composite," *Composites Science and Technology,* vol. 69, pp. 2064-2068, 2009.
[112] M. Rabuffi and G. Picci, "Status Quo and Future Prospects for Metallized Polypropylene Energy Storage Capacitors," *IEEE Transactions on Plasma Science,* vol. 30, pp. 1939-1942, 2002.
[113] T. Mitsui and W. B. Westphal, "Dielectric and X-Ray Studies of $Ca_xBa_{1-x}TiO_3$ and $Ca_xSr_{1-x}TiO_3$," *Physical Review,* vol. 124, pp. 1354-1359, 1961.
[114] W. Jackson and W. Reddish, "High Permittivity Crystalline Aggregates," *Nature,* vol. 156, pp. 717-717, 1945.
[115] J. Ihlefeld, B. Laughlin, A. Hunt-Lowery, W. Borland, A. Kingon, and J.-P. Maria, "Copper Compatible Barium Titanate Thin Films for Embedded Passives," *Journal of Electroceramics,* vol. 14, pp. 95-102, 2005.
[116] A. J. Lovinger, "Ferroelectric Polymers," *Science,* vol. 220, pp. 1115-1121, 1983.
[117] M. Bohlen and K. Bolton, "Conformational Studies of Poly(vinylidene fluoride), Poly(trifluoroethylene) and Poly(vinylidene fluoride-co-trifluoroethylene) Using Density Functional Theory," *Physical Chemistry Chemical Physics,* vol. 16, pp. 12929-12939, 2014.
[118] V. Sencadas, R. Gregorio, and S. Lanceros-Méndez, "α to β Phase Transformation and Microstructural Changes of PVDF Films Induced by Uniaxial Stretch," *Journal of Macromolecular Science, Part B,* vol. 48, pp. 514-525, 2009.
[119] L. Li, M. Zhang, M. Rong, and W. Ruan, "Studies on the Transformation Process of PVDF from Alpha to Beta Phase by Stretching," *RSC Advances,* vol. 4, pp. 3938-3943, 2014.
[120] S. Tuukkanen, T. Julin, V. Rantanen, M. Zakrzewski, P. Moilanen, K. E. Lilja, and S. Rajala, "Solution-Processible Electrode Materials for a Heat-Sensitive Piezoelectric Thin-Film Sensor," *Synthetic Metals,* vol. 162, pp. 1987-1995, 2012.
[121] O. C. Zienkiewicz, R. L. Taylor, and J. Z. Zhu, *The Finite Element Method: Its Basis and Fundamentals,* 6 ed. Oxford: Butterworth-Heinemann, 2013.
[122] S. Kumar and R. A. Gerhardt, "Role of Geometric Parameters in Electrical Measurements of Insulating Thin Films Deposited on a Conductive Substrate," *Measurement Science and Technology,* vol. 23, p. 035602, 2012.

[123] Y. Jin, S. Kumar, and R. A. Gerhardt, "Simulation of the Impedance Response of Thin Films as a Function of Film Conductivity and Thickness," *Proceedings of COMSOL Conference,* pp. 1-5, 2015.
[124] G. Branković, Z. Branković, V. Jović, and J. Varela, "Fractal Approach to ac Impedance Spectroscopy Studies of Ceramic Materials," *Journal of Electroceramics,* vol. 7, pp. 89-94, 2001.
[125] C. Chen, D. Chen, W. C. Chueh, and F. Ciucci, "Modeling the Impedance Response of Mixed-Conducting Thin Film Electrodes," *Physical Chemistry Chemical Physics,* vol. 16, pp. 11573-11583, 2014.
[126] X. Ren and P. G. Pickup, "Simulation and Analysis of the Impedance Behaviour of Electroactive Layers with Non-uniform Conductivity and Capacitance Profiles," *Electrochimica Acta,* vol. 46, pp. 4177-4183, 2001.
[127] R. A. Gerhardt, "Impedance Spectroscopy and Mobility Spectra," in *Encyclopedia of Condensed Matter Physics*, F. Bassani, G. L. Liedl, and P. Wyder, Eds., ed Oxford: Elsevier, 2005, pp. 350-363.
[128] E. Barsoukov and J. R. Macdonald, *Impedance Spectroscopy: Theory, Experiment, and Applications*, 2 ed. New York: Wiley-Interscience, 2005.
[129] R. A. Gerhardt, "Impedance and Dielectric Spectroscopy Revisited: Distinguishing Localized Relaxation from Long-Range Conductivity," *Journal of Physics and Chemistry of Solids,* vol. 55, pp. 1491-1506, 1994.
[130] C. J. Capozzi, Z. Li, R. J. Samuels, and R. A. Gerhardt, "Impedance Spectroscopy and Optical Characterization of Poly(methyl methacrylate)/Indium Tin Oxide Nanocomposites with Three-Dimensional Voronoi Microstructures," *Journal of Applied Physics,* vol. 104, p. 114902, 2008.
[131] R. A. Gerhardt, J. Runyan, C. Sana, D. S. McLachlan, and R. Ruh, "Electrical Properties of Boron Nitride Matrix Composites: III, Observations near the Percolation Threshold in BN–B4C Composites," *Journal of the American Ceramic Society,* vol. 84, pp. 2335-2342, 2001.
[132] T. L. Pruyn and R. A. Gerhardt, "Detection of Different Interfaces in Percolated Networks of Antimony Tin Oxide: Borosilicate Glass Composites by Impedance Spectroscopy," *Journal of the American Ceramic Society,* pp. 154-162, 2014.
[133] M. Narkis, "Size Distribution of Suspension-Polymerized Unsaturated Polyester Beads," *Journal of Applied Polymer Science,* vol. 23, pp. 2043-2048, 1979.
[134] G. C. Kuczynski, B. Neuville, and H. P. Toner, "Study of Sintering of Poly(methyl methacrylate)," *Journal of Applied Polymer Science,* vol. 14, pp. 2069-2077, 1970.
[135] R. German, *Powder Metallurgy Science*: Metal Powder Industries Federation, 1994.
[136] R. A. Gerhardt, R. Qu, Z. Li, R. J. Samuels, and C. J. Capozzi, "Composite Materials Having Low Filler Percolation Thresholds and Methods of Controlling Filler Interconnectivity," US Patent, 2010.
[137] A. J. Kinloch and R. J. Young, "Glassy Polymers I—Thermoplastics," in *Fracture Behaviour of Polymers*, ed: Springer Netherlands, 1995, pp. 229-285.
[138] J.-M. Thomassin, C. Jérôme, T. Pardoen, C. Bailly, I. Huynen, and C. Detrembleur, "Polymer/carbon Based Composites as Electromagnetic Interference

(EMI) Shielding Materials," *Materials Science and Engineering: R: Reports,* vol. 74, pp. 211-232, 2013.
[139] J. Ling, W. Zhai, W. Feng, B. Shen, J. Zhang, and W. g. Zheng, "Facile Preparation of Lightweight Microcellular Polyetherimide/Graphene Composite Foams for Electromagnetic Interference Shielding," *ACS Applied Materials & Interfaces,* vol. 5, pp. 2677-2684, 2013.
[140] Z. J. Li, B. C. Yang, S. R. Zhang, and C. M. Zhao, "Graphene Oxide with Improved Electrical Conductivity for Supercapacitor Electrodes," *Applied Surface Science,* vol. 258, pp. 3726-3731, 2012.
[141] A. J. Lichtenberg, "The Quasi-Static Approximation for Moving and Finite Temperature Plasmas," *Electron Devices, IEEE Transactions on,* vol. 11, pp. 62-65, 1964.
[142] M. Frary and C. A. Schuh, "Connectivity and Percolation Behaviour of Grain Boundary Networks in Three Dimensions," *Philosophical Magazine,* vol. 85, pp. 1123-1143, 2005.
[143] C. Goebbert, R. Nonninger, M. A. Aegerter, and H. Schmidt, "Wet Chemical Deposition of ATO and ITO Coatings using Crystalline Nanoparticles Redispersable in Solutions," *Thin Solid Films,* vol. 351, pp. 79-84, 1999.
[144] J. Sánchez-González, A. Macías-García, M. F. Alexandre-Franco, and V. Gómez-Serrano, "Electrical Conductivity of Carbon Blacks Under Compression," *Carbon,* vol. 43, pp. 741-747, 2005.
[145] N. Bao, L. Shen, G. Srinivasan, K. Yanagisawa, and A. Gupta, "Shape-Controlled Monocrystalline Ferroelectric Barium Titanate Nanostructures: From Nanotubes and Nanowires to Ordered Nanostructures," *The Journal of Physical Chemistry C,* vol. 112, pp. 8634-8642, 2008.
[146] S. Moon, H.-W. Lee, C.-H. Choi, and D. K. Kim, "Influence of Ammonia on Properties of Nanocrystalline Barium Titanate Particles Prepared by a Hydrothermal Method," *Journal of the American Ceramic Society,* vol. 95, pp. 2248-2253, 2012.
[147] Z.-M. Dang, S.-H. Yao, J.-K. Yuan, and J. Bai, "Tailored Dielectric Properties based on Microstructure Change in $BaTiO_3$-Carbon Nanotube/Polyvinylidene Fluoride Three-Phase Nanocomposites," *The Journal of Physical Chemistry C,* vol. 114, pp. 13204-13209, 2010.
[148] M. Selvi, M. Rangaraj Vengatesan, P. Prabunathan, J. Kun Song, and M. Alagar, "High Dielectric Multiwalled Carbon Nanotube-Polybenzoxazine Nanocomposites for Printed Circuit Board Applications," *Applied Physics Letters,* vol. 103, p. 152902, 2013.
[149] L. Jin, H. Wu, and M. Morbidelli, "Synthesis of Water-Based Dispersions of Polymer/TiO_2 Hybrid Nanospheres," *Nanomaterials,* vol. 5, p. 1454, 2015.
[150] S. R. Culler, H. Ishida, and J. L. Koenig, "FT-IR Characterization of the Reaction at the Silane/Matrix Resin Interphase of Composite Materials," *Journal of Colloid and Interface Science,* vol. 109, pp. 1-10, 1986.
[151] M. Arun, S. Kantheti, R. R. Gaddam, R. Narayan, and K. V. S. N. Raju, "Surface Modification of TiO_2 Nanoparticles with 1,3,5-Triazine based Silane Coupling Agent and its Cumulative Effect on the Properties of Polyurethane Composite Coating," *Journal of Polymer Research,* vol. 21, pp. 1-11, 2014.

[152] J. Zhao, M. Milanova, M. M. C. G. Warmoeskerken, and V. Dutschk, "Surface Modification of TiO_2 Nanoparticles with Silane Coupling Agents," *Colloids and Surfaces A: Physicochemical and Engineering Aspects,* vol. 413, pp. 273-279, 2012.
[153] M. Sabzi, S. M. Mirabedini, J. Zohuriaan-Mehr, and M. Atai, "Surface Modification of TiO_2 Nano-Particles with Silane Coupling Agent and Investigation of its Effect on the Properties of Polyurethane Composite Coating," *Progress in Organic Coatings,* vol. 65, pp. 222-228, 2009.
[154] J. Gomes, J. S. Nunes, V. Sencadas, and S. Lanceros-Mendez, "Influence of the β-Phase Content and Degree of Crystallinity on the Piezo- and Ferroelectric Properties of Poly(vinylidene fluoride)," *Smart Materials and Structures,* vol. 19, p. 065010, 2010.
[155] L. N. Sim, S. R. Majid, and A. K. Arof, "FTIR Studies of PEMA/PVDF-HFP Blend Polymer Electrolyte System Incorporated with $LiCF_3SO_3$ salt," *Vibrational Spectroscopy,* vol. 58, pp. 57-66, 2012.
[156] C. Pecharromán and J. S. Moya, "Experimental Evidence of a Giant Capacitance in Insulator–Conductor Composites at the Percolation Threshold," *Advanced Materials,* vol. 12, pp. 294-297, 2000.
[157] I. A. Malyshkina, G. V. Markin, and V. V. Kochervinskiĭ, "Investigation into the Dielectric Relaxation of Vinylidene Fluoride Copolymers with Hexafluoropropylene," *Physics of the Solid State,* vol. 48, pp. 1197-1199.
[158] D. Kim, Y. Kim, K. Choi, J. C. Grunlan, and C. Yu, "Improved Thermoelectric Behavior of Nanotube-Filled Polymer Composites with Poly(3,4-ethylenedioxythiophene) Poly(styrenesulfonate)," *ACS Nano,* vol. 4, pp. 513-523, 2009.
[159] K. H. Lee, J. Kao, S. S. Parizi, G. Caruntu, and T. Xu, "Dielectric properties of barium titanate supramolecular nanocomposites," *Nanoscale,* vol. 6, pp. 3526-3531, 2014.
[160] W. L. Zhong, Y. G. Wang, P. L. Zhang, and B. D. Qu, "Phenomenological Study of the Size Effect on Phase Transitions in Ferroelectric Particles," *Physical Review B,* vol. 50, pp. 698-703, 1994.
[161] S. Liu, S. Xue, B. Shen, and J. Zhai, "Reduced Energy Loss in Poly(vinylidene fluoride) Nanocomposites by Filling with a Small Loading of Core-Shell Structured $BaTiO_3/SiO_2$ Nanofibers," *Applied Physics Letters,* vol. 107, p. 032907, 2015.
[162] D. Yu, N.-x. Xu, L. Hu, Q.-l. Zhang, and H. Yang, "Nanocomposites with $BaTiO_3$-$SrTiO_3$ Hybrid Fillers Exhibiting Enhanced Dielectric Behaviours and Energy-Storage Densities," *Journal of Materials Chemistry C,* vol. 3, pp. 4016-4022, 2015.
[163] R. L. Muhlbauer, T. L. Pruyn, W. T. Puckett, and R. A. Gerhardt, "Effect of Graphitic Filler Size and Shape on the Microstructure, Electrical Percolation Behavior and Thermal Properties of Nanostructured Multilayered Carbon Films Deposited onto Paper Substrates," *Journal of Materials Research,* vol. 29, pp. 472-484, 2014.

[164] S. Zhang, L. M. Peng, Q. Chen, G. H. Du, G. Dawson, and W. Z. Zhou, "Formation Mechanism of $H_2Ti_3O_7$ Nanotubes," *Physical Review Letters,* vol. 91, p. 256103, 2003.
[165] Y. Mao and S. S. Wong, "Size and Shape Dependent Transformation of Nanosized Titanate into Analogous Anatase Titania Nanostructures," *Journal of the American Chemical Society,* vol. 128, pp. 8217-8226, 2006.